Physics and Applications of Four-Wave Mixing in Semiconductor Optical Amplifiers

Thesis by

Roberto Paiella

In Partial Fulfillment of the Requirements

for the Degree of

Doctor of Philosophy

California Institute of Technology

Pasadena, California

1999

(Defended June 18, 1998)

To My Parents

Acknowledgments

First and foremost, I wish to express my deepest gratitude to my advisor, Professor Kerry Vahala. I have always been amazed by his scientific knowledge, insight, and enthusiasm, and by his patience and love for teaching. I feel honored to have been a part of his research group for the past four years, and I am sure that his example will continue to inspire me in the future. Also, I really enjoyed his friendship.

Most of the work presented in this thesis was done in direct collaboration with Guido Hunziker, to whom I owe special thanks. I have thoroughly enjoyed working with him and have strongly benefited from his research skills and his great overall attitude. Furthermore, our collaboration has always been a lot of fun.

During my first three years at Caltech, I have also had a continuous interaction with Dr. David Geraghty and Dr. Robert Lee, then graduate students in the group, and I am grateful to them for sharing the lab facilities as well as their expertise in the system-level experiments. I would also like to acknowledge Dr. Jianhui Zhou for his help and guidance during my first year at Caltech, and Dr. Alessandro D'Ottavi of FUB, Italy, for a great collaboration the past summer. Other members of the Vahala group, past and present, that helped make my Ph.D. experience rewarding include: Dr. Renato Camata, Dr. Charles Tsai, Prof. Minyu Yao, Masashi Fukazawa, Dr. Per Olof Hedekvist, Elizabeth Boer, Dr. David Dougherty, Ashish Bhardwaj, Ming Cai, and Michael Shumway. My thanks also go to Rosalie Rowe for her help with administrative matters.

Furthermore, I am grateful to several researchers worldwide for the loan of the

semiconductor optical amplifiers used in this work: in particular, Dr. Uzi Koren of Lucent Technologies for the polarization insensitive devices used in the spectroscopy experiments; Dr. Mehrdad Ziari and Dr. Atul Mathur of SDL Inc. for the fiber-pigtailed laser; Dr. Roberto Dall'Ara of Optospeed, Switzerland, for the bulk amplifier used in the system-experiment collaboration with FUB; and, finally, Dr. James Whiteaway of Nortel, England, and Dr. Franck Delorme of France Telecom. Special thanks are also due to Dr. Thomas Schrans and Dr. Norman Kwong of Ortel Corp. for the loan of DFB lasers, rf-amplifiers and detectors. I would also like to acknowledge Prof. Richard Osgood of Columbia University for helping me move my first steps in the world of research, and for encouraging me to come to Caltech, and Dr. Carlo Sirtori of Bell Labs, now at Thomson-CSF, France, for stimulating discussions.

Finally, my deepest gratitude goes to my parents and to my sister for their unconditional patience, support and encouragement through the many years of my education, as well as for their more concrete help when the need arised.

Abstract

This thesis investigates the physical mechanisms responsible for four-wave mixing (FWM) in semiconductor optical amplifiers (SOAs), and their application to quantum-well spectroscopy and all-optical signal processing. A microscopic theory of polarization-resolved FWM is developed, and the corresponding polarization selection rules are derived. It is then shown how these results can be used to study basic carrier dynamics in semiconductor active layers. Finally, a wavelength conversion device and a new class of all-optical logic gates, based on FWM in SOAs, are presented and characterized.

The first part of the thesis is devoted to several experimental and theoretical investigations of carrier transport dynamics in multiquantum-well SOAs, and of their relation to the FWM nonlinearity of these devices. A polarization-resolved FWM configuration is used to study interwell carrier transport in a SOA consisting of alternating pairs of tensile and compressively strained quantum wells. A similar structure with interwell coupling provided by resonant tunneling is then investigated theoretically; it is shown how FWM can be used to excite coherent electric-dipole oscillations in this device, leading to efficient generation of TeraHertz radiation. Finally, a novel wavelength-resolved FWM technique is demonstrated to directly study the capture of carriers in quantum wells.

The second part of the thesis focuses on the application of FWM to all-optical signal processing for WDM communication systems. A wavelength conversion device based on FWM in a long (1.5 mm) SOA is developed, and used to demonstrate error-

free conversion of 10 Gbit/sec data over a record 30 nm wavelength span. Other configurations for wavelength conversion by FWM are then proposed and demonstrated, including: a dual-pump configuration for polarization insensitive operation; a self-pumped FWM converter, based on a fiber-Bragg-grating coupled diode laser; and a device based on injection-locked FWM in this same laser, characterized by a large resonance peak in its conversion efficiency. Finally, the last chapter is devoted to a novel class of all-optical logic gates, based on FWM, designed to operate on bytes of information encoded in wavelength ("byte-wide WDM").

Contents

List of Figures

Chapter 1

Introduction

Semiconductor optical amplifiers (SOAs) based on the InGaAsP material system, operating at 1.5 μm, are attractive components for all-optical signal processing applications in fiber-optic communication systems. Their use in these applications relies on the large gain and index nonlinearities typical of semiconductor materials. Consequently, a large research effort is currently focused on a variety of nonlinear optical processes in semiconductor active layers. A particularly interesting example is provided by four-wave mixing (FWM) between nondegenerate waves copropagating in the SOA waveguide. Since this process involves the interaction between distinct wavelength channels, it is particularly well suited to application in multiwavelength networks based on wavelength-division multiplexing (WDM), which is becoming the dominant technology for long-distance communications.

This thesis investigates the physics and applications of FWM in InGaAsP SOAs. In the first part, we present a series of experimental and theoretical studies of the physical mechanisms associated with the FWM nonlinearity of these devices. In par-

ticular, we focus on the relation between this nonlinearity and the transport dynamics of electrical carriers, in real and phase space, in multiquantum-well SOAs. In fact, we show that FWM provides quite a powerful spectroscopic tool to study these transport processes. In the second part of the thesis, we explore and demonstrate system level applications of FWM, in particular to wavelength conversion and all-optical processing of "byte-wide WDM" signals.

Chapter 2 contains a general introduction to the nonlinear optical properties of semiconductor gain media. The physical processes responsible for the gain and index nonlinearities of these media are qualitatively discussed. We then describe in general terms the FWM interaction in SOAs, and briefly review early FWM experiments.

Chapter 3 is devoted to the theoretical description of FWM in semiconductor active layers, based on the density-matrix formalism. This analysis gives a full microscopic solution for the FWM susceptibility (for simplicity, some of the relevant expressions are given in Appendix A). The vector nature of the interacting waves is explicitly included in our treatment, which leads to a set of polarization selection rules for all FWM mechanisms. Based on these results (which are also given a simple interpretation in terms of photon transition diagrams), we discuss the polarization properties of FWM, which will be used in the following, both for spectroscopy (chapter 4) and for wavelength conversion applications (chapter 7).

Chapter 4 describes an experiment based on polarization-resolved FWM aimed at studying the interwell carrier transport dynamics in a specially designed multiquantum-well SOA (consisting of alternating pairs of tensile and compressively strained quan-

tum wells). The theoretical framework of the previous chapter is extended to account for interwell coupling, and the resulting expressions are used to fit the experimental data and extrapolate the relevant time constants; in particular, a value of 16 psec is inferred for the overall interwell equilibration lifetime. At the end of the chapter, we present another experiment based on a similar polarization-resolved FWM configuration, providing an extremely simple technique to measure the interband stimulated recombination lifetime.

Chapter 5 considers theoretically FWM in a similar SOA structure, in the case where interwell coupling occurs through resonant tunneling. Using the density-matrix formalism, we propose a scheme for exciting in this device coherent electric-dipole oscillations, leading to a large resonance peak in the FWM conversion efficiency at TeraHertz detuning frequencies. Furthermore, we argue that this excitation scheme could be used for efficient generation of cw far-infrared radiation.

Chapter 6 presents a novel spectroscopic technique, based on wavelength-resolved FWM, to study the capture of electrical carriers in semiconductor quantum wells. Using a simple rate-equation model, we show how this technique can be used to directly measure the intrinsic capture lifetime, with no need for any involved numerical fit. We then demonstrate it using the same multiquantum-well SOA of chapter 4, and obtain an estimate of 1.8 psec for the capture lifetime in this device. Finally, we present a microscopic theory of phonon-assisted capture, in which the possible impact of hot-phonon effects is investigated.

Chapter 7 is devoted to a wavelength conversion device based on FWM in SOAs.

We discuss the design prescriptions developed in our labs to maximize its bit-error-rate performance, and apply them to demonstrate error-free FWM wavelength conversion at 10 Gbit/sec over a record 30 nm wavelength span. The standard theoretical description of the conversion efficiency and the noise properties of this device, based on the FWM coupled-mode wave equations, is summarized in Appendix B. Furthermore, we use the results of chapter 3 to propose and demonstrate (at 2.5 Gbit/sec) a polarization insensitive FWM wavelength converter, based on a dual-pump configuration.

Chapter 8 describes two different wavelength conversion devices based on FWM in a fiber-Bragg-grating coupled semiconductor laser. In one case, the lasing mode is used as the FWM pump wave, which eliminates the need for a high-power external pump source. Error-free wavelength conversion at 2.5 Gbit/sec is demonstrated with this device. Furthermore, we show that, as a result of its optical gain being clamped at threshold, its performance strongly improves with increasing pump power (much more than in the case of FWM in a single-pass SOA). In the second configuration, an external pump wave is used, and the converted signal wavelength is tuned to the Bragg wavelength; through a mechanism similar to injection-locking, this results in a large resonance enhancement of the FWM signal power. Finally, we discuss means to increase the spectral width of this resonance to make this approach suitable to high bit-rate operation.

Chapter 9 considers the use of WDM for byte-wide transmission and signal processing, i.e., the parallel transmission and processing of entire bytes of information on a same fiber, with each bit assigned to a different wavelength channel. In particular,

we propose a new class of all-optical logic gates, based on FWM, that operate on such multiwavelength data buses, with polarization used to define the logical state of each bit. We then conclude with a preliminary demonstration of an EXOR gate.

The work presented in this thesis has appeared in the journal articles [1]–[12] and conference presentations [13]–[22] listed below.

Bibliography

[1] A. D'Ottavi, P. Spano, G. Hunziker, R. Paiella, R. Dall'Ara, G. Guekos, and K. J. Vahala, "Wavelength Conversion at 10 Gb/s by Four-Wave Mixing Over a 30-nm Interval," *IEEE Photon. Technol. Lett.*, vol. 10, pp. 952–954, 1998.

[2] R. Paiella, G. Hunziker, M. Ziari, A. Mathur, and K. J. Vahala, "Wavelength Conversion by Cavity-Enhanced Injection-Locked Four-Wave Mixing in a Fiber-Bragg-Grating Coupled Diode Laser," *IEEE Photon. Technol. Lett.*, vol. 10, pp. 802–804, 1998.

[3] R. Paiella, G. Hunziker, K. J. Vahala, and U. Koren, "Four-Wave Mixing Mediated by the Capture of Electrons and Holes in Semiconductor Quantum-Well Laser Amplifiers," *Appl. Phys. Lett.*, vol. 71, pp. 3601–3603, 1997.

[4] G. Hunziker, R. Paiella, M. Ziari, A. Mathur, and K. J. Vahala, "Folded-Path, Self-Pumped Wavelength Converter Based on Four-Wave Mixing in a Semiconductor Optical Amplifier," *IEEE Photon. Technol. Lett.*, vol. 9, pp. 1352–1354, 1997.

[5] K. J. Vahala, R. Paiella, and G. Hunziker, "Ultrafast WDM Logic," *IEEE J. Select. Topics in Quantum Electron.*, vol. 3, pp. 698–701, 1997.

[6] R. Paiella, G. Hunziker, U. Koren, and K. J. Vahala, "Polarization-Dependent Optical Nonlinearities of Multiquantum-Well Laser Amplifiers Studied by Four-Wave Mixing," *IEEE J. Select. Topics in Quantum Electron.*, vol. 3, pp. 529–540, 1997.

[7] G. Hunziker, R. Paiella, K. J. Vahala, and U. Koren, "Measurement of the Stimulated Carrier Lifetime in Semiconductor Optical Amplifiers by Four-Wave

Mixing of Polarized ASE Noise," *IEEE Photon. Technol. Lett.*, vol. 9, pp. 907–909, 1997.

[8] R. Paiella, G. Hunziker, K. J. Vahala, and U. Koren, "Measurement of the Interwell Carrier Transport Lifetime in Multiquantum-Well Optical Amplifiers by Polarization-Resolved Four-Wave Mixing," *Appl. Phys. Lett.*, vol. 69, pp. 4142–4144, 1996.

[9] G. Hunziker, R. Paiella, D. F. Geraghty, K. J. Vahala, and U. Koren, "Polarization-Independent Wavelength Conversion at 2.5 Gb/s by Dual-Pump Four-Wave Mixing in a Strained Semiconductor Optical Amplifier," *IEEE Photon. Technol. Lett.*, vol. 8, pp. 1633–1635, 1996.

[10] R. Paiella, G. Hunziker, J. Zhou, K. J. Vahala, U. Koren, and B. I. Miller, "Polarization Properties of Four-Wave Mixing in Strained Semiconductor Optical Amplifiers," *IEEE Photon. Technol. Lett.*, vol. 8, pp. 773–775, 1996.

[11] R. Paiella and K. J. Vahala, "Four-Wave Mixing and Generation of TeraHertz Radiation in an Alternating-Strain Coupled Quantum-Well Structure," *IEEE J. Quantum Electron.*, vol. 32, pp. 721–728, 1996.

[12] R. Paiella and K. J. Vahala, "Highly Nondegenerate Four-Wave Mixing Efficiency of an Asymmetric Coupled Quantum-Well Structure," *Appl. Phys. Lett.*, vol. 66, pp. 2619–2621, 1995.

[13] G. Hunziker, R. Paiella, U. Koren, and K. J. Vahala, "Four-Wave Mixing Mediated by the Capture of Carriers in Semiconductor Quantum-Well Amplifiers," *Conference on Laser and Electro-Optics*, San Francisco, California, May 3–8, 1998, paper CThR3.

[14] R. Paiella, G. Hunziker, M. Ziari, A. Mathur, and K. J. Vahala, "Resonance Enhancement of the Four-Wave Mixing Efficiency by Injection Locking in a Fiber-Bragg-Grating Coupled Semiconductor Laser," *Conference on Laser and Electro-Optics*, San Francisco, California, May 3–8, 1998, paper CWC5.

[15] K. J. Vahala, R. Paiella, G. Hunziker, and U. Koren, "Direct Measurement of Capture and Escape Rates in Quantum Well Active Layers," *OSA Victoria Topical Meeting on Integrated Photonics Research*, Victoria, British Columbia, Canada, March 29–April 1, 1998, paper ITuG4 (**Invited Paper**).

[16] G. Hunziker, R. Paiella, A. D'Ottavi, P. Spano, R. Dall'Ara, G. Guekos, and K. J. Vahala, "30 nm Wavelength Conversion at 10 Gb/s by Four-Wave Mixing in a Semiconductor Optical Amplifier," *Optical Fiber Communication Conference*, San Jose, California, February 22–27, 1998, paper WB7.

[17] R. Paiella, G. Hunziker, M. Ziari, A. Mathur, and K. J. Vahala, "Wavelength Conversion by Four-Wave Mixing in a Folded-Path, Self-Pumped Semiconductor Optical Amplifier," *Optical Fiber Communication Conference*, San Jose, California, February 22–27, 1998, paper WB8.

[18] K. J. Vahala, R. B. Lee, D. F. Geraghty, G. Hunziker, R. Paiella, M. Ziari, and A. Mathur, "Tera-Hertz Carrier Dynamics and Application to All-Optical Wavelength Conversion," *IEEE Lasers and Electro-Optics Society Annual Meeting*, San Francisco, California, November 10–13, 1997, paper MN5 (**Invited Paper**).

[19] K. J. Vahala, R. Paiella, G. Hunziker, R. B. Lee, and D. F. Geraghty, "Ultrafast Semiconductor Carrier Dynamics Probed by Four-Wave Mixing and Application to All-Optical Signal Processing in WDM Systems," *OSA Spring Topical Meeting on Ultrafast Electronics and Optoelectronics*, Incline Village, Nevada, March 17–19, 1997, paper UMC1 (**Invited Paper**).

[20] G. Hunziker, R. Paiella, K. J. Vahala, and U. Koren, "Interwell Carrier Transport Rate Measured by Four-Wave Mixing," *IEEE International Semiconductor Laser Conference*, Haifa, Israel, October 13–18, 1996, paper PDP4 (**Postdeadline Paper**).

[21] K. J. Vahala, R. B. Lee, D. F. Geraghty, G. Hunziker, and R. Paiella, "Wavelength Conversion by Four-Wave Mixing in Semiconductor Amplifiers," *Optical Society of America Annual Meeting*, Rochester, New York, October 20–24, 1996, paper MDD2 (**Invited Paper**).

[22] R. Paiella, G. Hunziker, J. Zhou, K. J. Vahala, U. Koren, and B. I. Miller, "Using Tensor Properties of Four-Wave Mixing in Semiconductor Optical Amplifiers for Polarization-Independent Wavelength Conversion or Pump Suppression," *Conference on Laser and Electro-Optics*, Anaheim, California, June 2–7, 1996, paper CFF1.

Chapter 2

Nonlinear Optics of Semiconductor Gain Media

2.1 Introduction

Semiconductor lasers [1]–[3] based on the InGaAsP material system, emitting at 1.55 μm (the wavelength of minimum loss in silica fibers), are ideal signal sources for high-speed fiber-optic communication systems. In the previous decade, in parallel with the development of these diode lasers, semiconductor optical amplifiers (SOAs) based on the same material system have also been developed and investigated [4]–[8]. In their simplest form, these devices consist of semiconductor lasers with anti-reflection coated [4] and/or angled [5] facets (typically resulting in facet reflectivities of $< 10^{-4}$) for single-pass traveling-wave amplification. Despite their small size, SOAs can provide large small-signal gain, up to about 30 dB. In fact, they were originally considered for all-optical regeneration in long-haul fiber transmission lines [6]–[8]. However, Erbium-

doped fiber amplifiers (EDFAs) [9], developed later, turned out to be much better suited to this application, and by now they have completely replaced SOAs as in-line amplifiers. On the other hand, in the past few years there has been a revival of interest in SOAs, focused on their strong nonlinear optical response.

It is well known that semiconductor gain media are characterized by large optical nonlinearities [10]–[15], that strongly affect their dynamic and spectral properties. For instance, the large nonlinear gain compression typical of diode lasers is directly related to the maximum direct modulation bandwidth of these devices [16]. In SOAs, the same saturation processes are responsible for cross-talk among different wavelength channels and for the distortion and chirping of short optical pulses [17]. These features obviously pose serious limitations to the use of these amplifiers as in-line repeaters in optical communication networks, for which gain linearity is highly desirable; in fact, this is one of the main reasons why EDFAs (which are characterized by extremely large saturation powers) are preferable for this application. On the other hand, the nonlinear interaction among different channels in SOAs makes them promising candidates for applications involving wavelength conversion [18] and, more in general, all-optical signal processing.

The work reported in this thesis belongs to an extensive research program focused on the optical nonlinearities of semiconductor gain media. On the one hand, we want to measure their relative strength and speed, determine whether they are primarily resistive, reactive or both (i.e., gain versus index nonlinearities), and characterize their dependence on the device structure, operating conditions, etc. On the other

hand, we want to explore their applications. In both cases we will use four-wave mixing, either as a spectroscopic tool, or as a means to make different wavelength channels interact with one another.

2.2 Semiconductor Gain and Index Nonlinearities

In general, three main mechanisms contribute to the strong dependence of both the gain and the refractive index of a semiconductor on the optical field intensity; namely: carrier density depletion, carrier heating and spectral hole burning. The basic idea in each case is that as optical power builds up within the device, the distribution of carriers in the conduction and valence bands is correspondingly modified. This is illustrated schematically in Figs. 2.1a-c, where we plot the occupation probability ρ of the available states in either band as a function of energy E into the band. The dashed line in each plot corresponds to the limit of negligible optical power, in which case $\rho(E)$ is a quasi-Fermi distribution determined by the steady-state electrical current used to bias the device. The continuous lines show how this occupancy function is modified in the presence of a large optical field, through the mechanisms listed above. This in turn leads to changes in both the gain and the carrier-induced refractive index, which are very sensitive to the carrier distribution.

The strongest nonlinear mechanism is carrier density depletion, which refers to the reduction of the overall number of carriers with increasing optical power brought about by stimulated electron-hole recombination. The corresponding change in the states occupancy is illustrated in Fig. 2.1a, and it is accompanied by a decrease

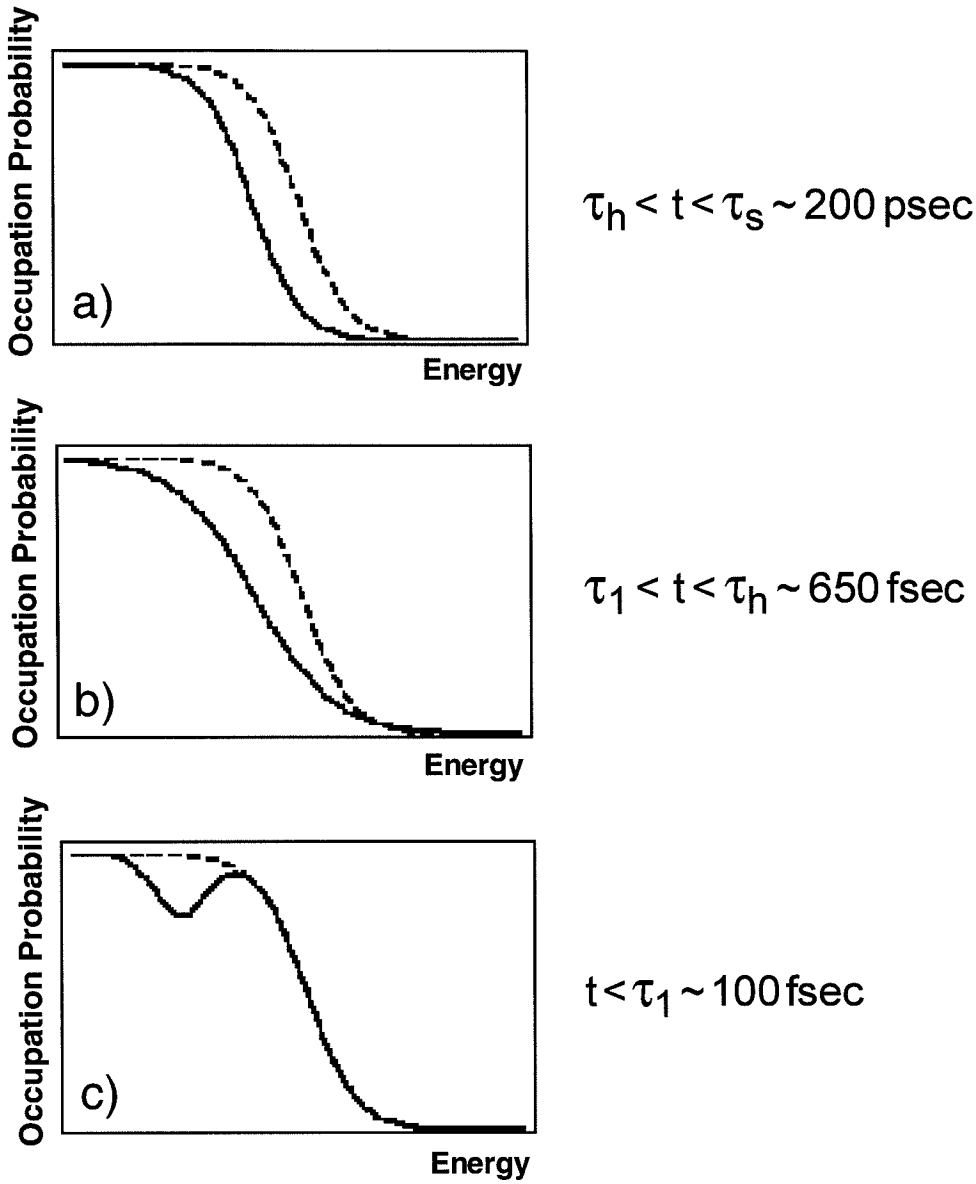

Figure 2.1: Dynamic evolution of the occupation probability of the available energy states in each band in the presence of a strong optical field. The dashed line corresponds to the limit of negligible optical power; the continuous lines show how this is modified through carrier density depletion (a), carrier heating (b), and spectral hole burning (c). The corresponding time scales are also indicated.

in optical gain and (because of the finite, positive linewidth enhancement factor) an increase in refractive index. The quasi-equilibrium carrier number tends to be recovered through the interplay of electrical injection and stimulated recombination, with a characteristic time scale τ_s on the order of a few hundreds of picoseconds under typical SOA operating conditions. This lifetime then determines the speed of the carrier density depletion nonlinearity.

Stimulated recombination, as well as free-carrier absorption, removes carriers from states near the bottom of each band, having relatively low kinetic energy. As shown schematically in Fig. 2.1b, the net result (after a quasi-Fermi distribution is re-established in each band by carrier-carrier scattering) is an increase in the carrier temperature, which leads to a further compression of the gain and increase in the index [12], [13]. The lifetime of this mechanism τ_h is set by carrier-LO phonon scattering (which tends to restore the lattice temperature in each band), and it has been measured in InGaAsP SOAs to be approximately 600 fsec [14], [19].

Finally, spectral hole burning (illustrated in Fig. 2.1c) refers to the reduction of the occupation probabilities of the electronic states resonantly interacting with the optical field [10], [11]. This reduction persists on a time scale τ_1 set by carrier-carrier scattering (on the order of 100 fsec or less at the large carrier densities typical of laser and SOA operation). Notice that the "spectral hole" in the optical gain spectrum is quite symmetrical about the photon energy; as a result, the corresponding index nonlinearity is negligible for this mechanism, as can be argued on the basis of the Kramers-Kronig relations.

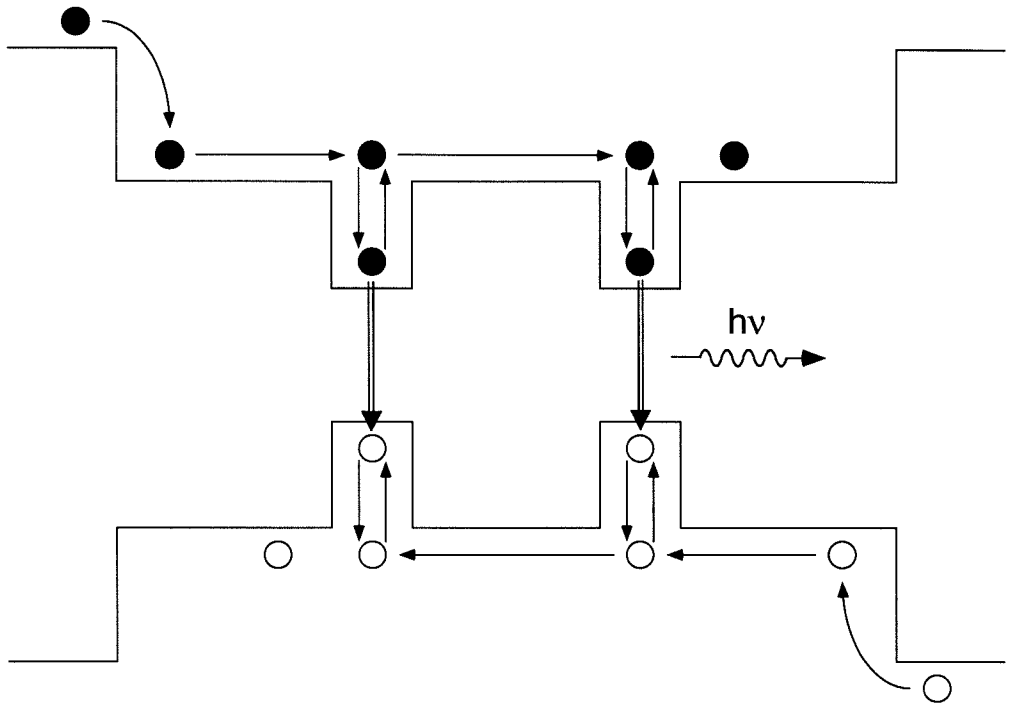

Figure 2.2: Interwell transport dynamics of electrical carriers in multiquantum-well optical amplifiers.

In addition to the above interband and intraband nonlinearities, (multi)quantum-well (QW) active layers are characterized by an additional, structure-dependent source of optical nonlinearity, related to carrier transport processes in real and phase space [20]–[23]. These processes (shown schematically in Fig. 2.2) include classical diffusion and drift across the barrier region, and "quantum capture" (escape) of carriers into (out of) the bound states of the QWs, mediated by the emission (absorption) of LO phonon (and by carrier-carrier scattering in the presence of large carrier densities). The finite lifetimes associated with such carrier dynamics set the time scale with which the quasi-equilibrium carrier density is re-established in each QW. As

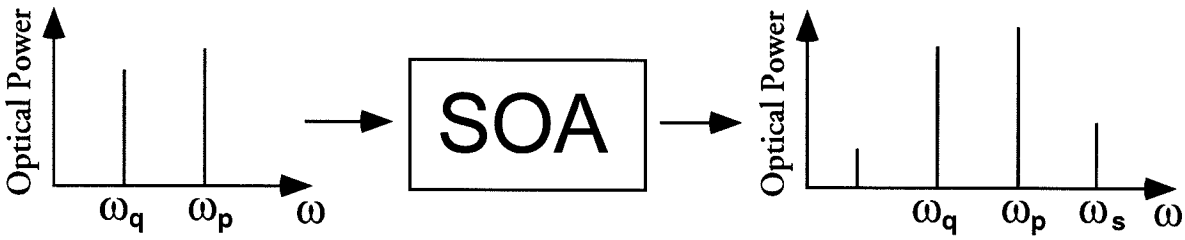

Figure 2.3: Schematic illustration of four-wave mixing in semiconductor optical amplifiers.

a result, the transport processes mentioned above effectively provide an additional contribution to the carrier density depletion nonlinearity of QW active layers. This contribution is particularly important to the dynamic properties of QW lasers, since it is believed to have an important role in limiting the maximum direct modulation bandwidth of these lasers [20]–[23].

2.3 Four-Wave Mixing in Semiconductor Optical Amplifiers

In recent years, nondegenerate four-wave mixing (FWM) in SOAs [19], [24]–[27] has emerged as a powerful frequency-domain technique to study the optical nonlinearities of semiconductor gain media. The basic configuration of a FWM experiment is illustrated in Fig. 2.3: two copropagating cw waves at different frequencies, a strong pump wave of frequency ω_p and a probe wave (or input signal) of frequency ω_q, are coupled into the SOA waveguide, so that the overall optical intensity in the active layer will include a harmonic component at their detuning frequency $\Omega \equiv \omega_p - \omega_q$. The gain and refractive index are then modulated at this frequency by way of all

of the nonlinear mechanisms just discussed. The resulting dynamic gain and index gratings partially scatter the input waves into new sideband signals, whose relative intensities are measured as a function of the detuning frequency.

The FWM signal generated by scattering of the pump wave, at frequency $\omega_s = \omega_p + \Omega = 2\omega_p - \omega_q$, has field amplitude approximately given, as a function of Ω, by the following expression [19]

$$E_s^{out} = \left(E_p^{in}\right)^2 \left(E_q^{in}\right)^* \sum_{m=1}^{3} \frac{C_m}{1 - i\Omega\tau_m} \tag{2.1}$$

where the index m runs over the three nonlinear mechanisms described above, τ_m is the corresponding characteristic lifetime, and C_m is a complex-valued constant (a rigorous expression for $\vec{E}_s$ will be derived in the next chapter). Notice that FWM can be viewed as the frequency-domain counterpart of pump-probe spectroscopy, which has also been used to study the optical nonlinearities of InGaAsP SOAs [14], [15]. Specifically, while pump-probe experiments measure the impulse response fuction of a given physical system, FWM measures the corresponding frequency response function, as given for instance in Eq. (2.1).

The results of a typical FWM experiment are shown in Fig. 2.4 (from Ref. [19]), where the circles and squares correspond, respectively, to positive and negative detuning frequencies (i.e., frequency up- and down-conversion). The dashed line shows the 20 dB/dec roll-off associated with stimulated interband recombination (i.e., the carrier density modulation contribution to the FWM signal). The continuous lines are theoretical fits based on Eq. (2.1), from which one can infer the relative strength (and phase) of the different contributing nonlinear mechanisms, and estimate the as-

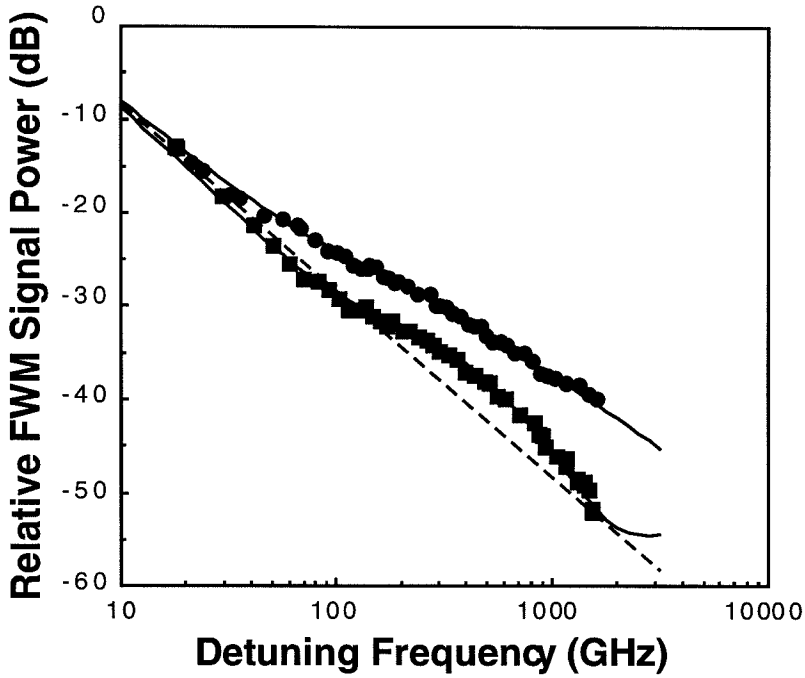

Figure 2.4: Four-wave mixing conversion efficiency versus positive (circles) and negative (squares) detuning frequency in a multiquantum-well optical amplifier (from Ref. [19]).

sociated lifetimes. In particular, these data give a stimulated recombination lifetime $\tau_s > 20$ psec, a carrier cooling lifetime $\tau_h \approx 650$ fsec, and a carrier-carrier scattering lifetime $\tau_1 < 100$ fsec.

To further resolve τ_s, the measured frequency range should be extended to subGigaHertz values: this measurement, however, is complicated by the large variation in the FWM signal power with Ω at small detuning frequencies, so that extremely accurate readings of both power and frequency would be required for meaningful results. Similarly, in order to infer τ_1 from the data, the measured detuning frequency should be extended to several TeraHertz, where the FWM signal power becomes vanishingly small. Finally, we notice in Fig. 2.4 a large asymmetry in the FWM conversion ef-

ficiency for positive and negative detuning frequencies, which is due to interference among the various contributing mechanisms.

As it follows from Eq. (2.1), the field amplitude of the FWM signal is proportional to the complex conjugate of the probe wave: as a result, if information is encoded on this field component, whether on its magnitude or phase, the same information is translated at the new frequency ω_s. Indeed, in view of the large magnitude and ultrafast nature of the nonlinearities involved, FWM in SOAs is a promising candidate for the implementation of broadband wavelength conversion in wavelength division multiplexed (WDM) communication networks [28]–[31]. Additional applications of FWM include dispersion compensation by optical phase conjugation [32], time-division demultiplexing [33], [34] and all-optical signal processing [35], [36].

Bibliography

[1] G. P. Agrawal and N. K. Dutta, *Long-Wavelength Semiconductor Lasers*, van Nostrand Reinhold, 1986.

[2] W. W. Chow, S. W. Koch, and M. Sargent III, *Semiconductor-Laser Physics*, Springer-Verlag, 1994.

[3] P. S. Zory, Jr., Ed., *Quantum Well Lasers*, Academic Press, 1993.

[4] T. Saitoh, T. Mukai and O. Mikami, "Theoretical-analysis and fabrication of antireflection coatings on laser-diode facets," *IEEE J. Lightwave Technol.*, vol. 3, pp. 288–293, 1985.

[5] C. E. Zah, J. S. Osinski, C. Caneau, S. G. Menocal, L. A. Reith, J. Salzman, F. K. Shokoohi, and T. P. Lee, "Fabrication and performance of 1.5 μm GaInAsP traveling-wave laser amplifiers with angled facets," *Electron. Lett.*, vol. 23, pp. 990–992, 1987.

[6] J. C. Simon, "GaInAsP semiconductor laser amplifiers for single mode fiber communications," *IEEE J. Lightwave Technol.*, vol. 5, pp. 1286–1295, 1987.

[7] N. A. Olsson, "Lightwave systems with optical amplifiers," *IEEE J. Lightwave Technol.*, vol. 7, pp. 1071–1082, 1989.

[8] M. G. Oberg, N. A. Olsson, L. A. Koszi and G. J. Przybylek, "313-km transmission experiment at 1 Gbit/s using optical amplifiers and a low chirp laser," *Electron. Lett.*, vol. 24, pp. 38–39, 1988.

[9] E. Desurvire, *Erbium-Doped Fiber Amplifiers: Principles and Applications*, John Wiley & Sons, Inc., 1994.

[10] M. Asada and Y. Suematsu, "Density-matrix theory of semiconductor lasers with relaxation broadening model-Gain and gain suppression in semiconductor lasers," *IEEE J. Quantum Electron.*, vol. 21, pp. 434–442, 1985.

[11] G. P. Agrawal, "Gain nonlinearity in semiconductor lasers: Theory and applications to distributed feedback lasers," *IEEE J. Quantum Electron.*, vol. 23, pp. 860–868, 1987.

[12] M. P. Kesler and E. P. Ippen, "Subpicosecond gain dynamics in GaAlAs laser diodes," *Appl. Phys. Lett.*, vol. 51, pp. 1765–1767, 1987.

[13] B. N. Gomatam and A. P. DeFonzo, "Theory of hot carrier effects on nonlinear gain in GaAs-GaAlAs lasers and amplifiers," *IEEE J. Quantum Electron.*, vol. 26, pp. 1689–1704, 1990.

[14] K. L. Hall, J. Mark, E. P. Ippen, and G. Eisenstein, "Femtosecond gain dynamics in InGaAsP optical amplifiers," *Appl. Phys. Lett.*, vol. 56, pp. 1740–1742, 1990.

[15] K. L. Hall, A. M. Drawish, E. P. Ippen, U. Koren, and G. Raybon, "Femtosecond index nonlinearities in InGaAsP optical amplifiers," *Appl. Phys. Lett.*, vol. 62, pp. 1320–1322, 1993.

[16] J. E. Bowers, "High speed semiconductor laser design and performance," *Solid State Electron.*, vol. 30, no. 1, pp. 1–11, 1987.

[17] N. A. Olsson and G. P. Agrawal, "Spectral shift and distortion due to self-phase modulation of picosecond pulses in 1.5 μm optical amplifiers," *Appl. Phys. Lett.*, vol. 55, pp. 13–15, 1989.

[18] S. J. B. Yoo, "Wavelength conversion technologies for WDM network applications," *J. Lightwave Technology*, vol. 14, pp. 955–965, 1996.

[19] J. Zhou, N. Park, J. W. Dawson, K. J. Vahala, M. A. Newkirk, and B. I. Miller, "Terahertz four-wave mixing spectroscopy for study of ultrafast dynamics in a semiconductor optical amplifier," *Appl. Phys. Lett.*, vol.63, pp. 1179 – 1181, 1993.

[20] W. Rideout, W. F. Sharfin, E. S. Koteles, M. O. Vassell, and B. Elman, "Well-barrier hole burning in quantum well lasers," *IEEE Photon. Technol. Lett.*, vol. 3, pp. 784–786, 1991.

[21] R. Nagarajan, T. Fukushima, S. W. Corzine, and J. E. Bowers, "Effects of carrier transport on high-speed quantum well lasers," *Appl. Phys. Lett.*, vol. 59, pp. 1835–1837, 1991.

[22] S. C. Kan, D. Vassilovski, T. C. Wu, and K. Y. Lau, "On the effects of carrier diffusion and quantum capture in high speed modulation of quantum well lasers," *Appl. Phys. Lett.*, vol. 61, pp. 752–754, 1992.

[23] N. Tessler and G. Eisenstein, "On carrier injection and gain dynamics in quantum well lasers," *IEEE J. Quantum Electron.*, vol. 29, pp. 1586–1595, 1993.

[24] G. P. Agrawal, "Population pulsations and nondegenerate four-wave mixing in semiconductor lasers and amplifiers," *J. Opt. Soc. Am. B*, vol. 5, pp. 147–158, 1988.

[25] K. Kikuchi, M. Kakui, C. E. Zah, and T. P. Lee, "Observation of highly nondegenerate four-wave mixing in 1.5 μm traveling-wave semiconductor optical amplifiers and estimation of nonlinear gain coefficient," *IEEE J. Quantum Electron.*, vol. 28, pp. 151–156, 1992.

[26] A. Uskov, J. Mϕrk, and J. Mark, "Wave mixing in semiconductor laser amplifiers due to carrier heating and spectral hole burning," *IEEE J. Quantum Electron.*, vol. 30, pp. 1769–1781, 1994.

[27] A. Mecozzi, S. Scotti, A. D'Ottavi, E. Iannone, and P. Spano, "Four-wave mixing in traveling-wave semiconductor amplifiers," *IEEE J. Quantum Electron.*, vol. 31, pp. 689–699, 1995.

[28] M. C. Tatham, G. Sherlock, and L. D. Westbrook, "20 nm wavelength conversion using nondegenerate four-wave mixing," *IEEE Photon. Technol. Lett.*, vol. 5, pp. 1303 – 1306, 1993.

[29] J. Zhou, N. Park, J. W. Dawson, K. J. Vahala, M. A. Newkirk, and B. I. Miller, "Efficiency of broadband four-wave mixing wavelength conversion using semiconductor traveling-wave amplifiers," *IEEE Photon. Technol. Lett.*, vol. 6, pp. 50–52, 1994.

[30] D. F. Geraghty, R. B. Lee, M. Verdiell, M. Ziari, A. Mathur, and K. J. Vahala, "Wavelength conversion for WDM communication systems using four-wave mix-

ing in semiconductor optical amplifiers," to appear on the October 1997 issue of the *IEEE J. Select. Topics Quantum Electron.*

[31] A. D'Ottavi, F. Girardin, L. Graziani, F. Martelli, P. Spano, A. Mecozzi, S. Scotti, R. Dall'Ara, J. Eckner, and G. Guekos, "Four-wave mixing in semiconductor optical amplifiers: a practical tool for wavelength conversion," *IEEE J. Select. Topics Quantum Electron.*, vol. 3, pp. 522–528, 1997.

[32] D. D. Marcenac, D. Nesset, A. E. Kelly, M. Brierly, A. D. Ellis, D. G. Moodie, and C. W. Ford, "40 Gbit/s transmission over 406 km of NDSF using mid-span spectral inversion in a 2 mm long semiconductor optical amplifier," *Electron. Lett.*, vol. 33, pp. 879–881, 1997.

[33] T. Morioka, H. Takara, S. Kawanishi, K. Uchiyama, and M. Saruwatari, "Polarization-independent all-optical demultiplexing up to 200 Gbit/s using four-wave mixing in a semiconductor laser amplifier," *Electron. Lett.*, vol. 32, pp. 840–841, 1996.

[34] S. Diez, C. Schmidt, R. Ludwig, H. G. Weber, K. Obermann, S. Kindt, I. Koltchanov, and K. Petermann, "Four-wave mixing in semiconductor optical amplifiers for frequency conversion and fast optical switching," *IEEE J. Select. Topics Quantum Electron.*, vol. 3, pp. 1131–1145, 1997.

[35] D. Nesset, M. Tatham, and D. Cotter, "All-optical AND gate operating on 10 Gbit/s signals at the same wavelength using four-wave mixing in a single semiconductor laser amplifier," *Electron. Lett.*, vol. 31, pp. 896–898, 1995.

[36] K. J. Vahala, R. Paiella, and G. Hunziker, "Ultrafast WDM logic," *IEEE J. Select. Topics Quantum Electron.*, vol. 3, pp. 698–701, 1997.

Chapter 3

Polarization-Resolved Four-Wave Mixing (FWM) in Semiconductor Optical Amplifiers

3.1 Introduction

In order to fully make use of the FWM interaction in SOAs, either as a spectroscopic tool or for all-optical signal processing applications, a detailed theory of such interaction must be formulated, to account for the dependence of the FWM conversion efficiency on the SOA structure and excitation conditions. A complete microscopic theory of FWM processes in semiconductor active layers requires use of the density-matrix formalism. In its simplest form, this description treats the semiconductor gain medium as a collection of inhomogeneously broadened, independent two-state systems (each corresponding to a different point in reciprocal space). This approach has been

successfully used to account for the dependence of the FWM conversion efficiency on the pump-probe detuning frequency [1], [2], yielding results in good agreement with experiments. On the other hand, this treatment is inadequate to describe polarization effects, and it is therefore limited to the case of copolarized input waves with fixed polarization state.

However, the efficiency of any nonlinear optical process such as FWM strongly depends on the polarization states of the optical waves involved. This issue is particularly important in QW gain media due to the typically large anisotropy of their optical response, which immediately follows from the presence of a preferred direction in the active region, the growth axis. In this chapter, we present a detailed study of the polarization properties of FWM in SOAs [3], [4] (with emphasis on QW structures). The importance of this study is twofold. On the one hand, in applications such as wavelength conversion, it is of paramount importance to minimize the dependence of the conversion efficiency on the polarization of the input signal. This issue will be considered in detail in chapter 7. Secondly, as will be shown in the next chapter, the same polarization properties can be exploited to extend the scope of FWM as a spectroscopic tool. Furthermore, while deriving these properties, a full analytic solution for the FWM susceptibility tensor, as a function of all relevant parameters, is obtained (for the sake of simplicity, some of the resulting expressions are given in Appendix A).

In order to include polarization effects, we consider in the next section a multi-state density-matrix model, including the spin-degenerate states in the lowest conduction

and valence subbands at a same $\vec{k}$. The results of this analysis are given a simple interpretation in terms of photon transition diagrams, and the FWM polarization selection rules are then derived and discussed. Furthermore, we apply these results to determine how the power and the polarization state of the FWM signal depend on the polarization states of the input waves, and experimentally verify these predictions. Finally, in the last section of the chapter, we discuss the possibility of obtaining FWM with a TE-polarized pump wave and TM-polarized probe wave (or vice versa), in which case the dynamic gratings arise from modulation of the optically-induced phase coherence between spin-degenerate states. However, in an attempt to measure this contribution in a multiquantum-well (MQW) device, we find it to be exceedingly small due to a large birefringence-induced phase mismatch.

3.2 The FWM Susceptibility Tensor

In the following analysis, we consider the usual case of a pump wave $\vec{E}^{(p)}$ of frequency ω_p and a probe wave $\vec{E}^{(q)}$ of frequency ω_q traveling along the SOA waveguide. The pump is assumed to be significantly stronger than the probe, and we only consider the FWM signal at frequency $\omega_s = 2\omega_p - \omega_q$. The FWM susceptibility tensor χ_{ijkl} is defined so that the harmonic component of the induced polarization density at ω_s is $P_i^{(s)} = \chi_{ijkl} E_j^{(p)} E_k^{(p)} (E_l^{(q)})^*$, where the indexes j and k refer to the pump components involved in the scattering process and the gratings-formation process respectively. We

calculate this tensor from the microscopic expression for $\vec{P}$,

$$\vec{P}(t) = \frac{1}{V} \sum_{\vec{k},v,c} \rho_{cv}(t) \vec{\mu}^*_{cv}, \tag{3.1}$$

where the index c (v) runs over the two spin-degenerate states in the conduction (valence) (sub)band. Strict conservation of the crystal wavevector $\vec{k}$ in optical transition is assumed. Furthermore, $\vec{\mu}$ is the electric dipole moment operator, and ρ is the density matrix of the electronic system. Note that here and in the following, the explicit dependence on $\vec{k}$ is omitted for notational simplicity.

The time evolution of the polarization function ρ_{cv} is coupled by the optical field to that of the occupation probabilities $\rho_x \equiv \rho_{xx}$ $(x = c, v)$ and of the coherence functions $\rho_{xx'}$ (with $x \neq x'$) according to the two-band Bloch equations [5]

$$\dot{\rho}_{cv} + \left(i\omega_{cv} + \frac{1}{\tau_{cv}} \right) \rho_{cv} = \frac{i}{\hbar} \left(\sum_{v'} \vec{\mu}_{cv'} \rho_{v'v} - \sum_{c'} \rho_{cc'} \vec{\mu}_{c'v} \right) \cdot \vec{E}(t) \tag{3.2}$$

$$\dot{\rho}_{v'v} + \frac{1}{\tau_{v'v}} \left(\rho_{v'v} - f_v \delta_{v',v} \right) = \frac{i}{\hbar} \sum_{c'} \left(\vec{\mu}^*_{c'v'} \rho_{c'v} - \rho^*_{c'v'} \vec{\mu}_{c'v} \right) \cdot \vec{E}(t) \tag{3.3}$$

$$\dot{\rho}_{cc'} + \frac{1}{\tau_{cc'}} \left(\rho_{cc'} - f_c \delta_{c,c'} \right) = -\frac{i}{\hbar} \sum_{v'} \left(\rho_{cv'} \vec{\mu}^*_{c'v'} - \vec{\mu}_{cv'} \rho^*_{c'v'} \right) \cdot \vec{E}(t), \tag{3.4}$$

where $\hbar\omega_{cv} = \epsilon_c - \epsilon_v$ is the transition energy, and several phenomenological time constants have been introduced to account for damping processes. In particular, τ_{cv} is the usual dipole dephasing lifetime, and $1/\tau_{xx'}$ is the rate at which $\rho_{xx'}$ relaxes to its quasi-equilibrium value (i.e., the quasi-Fermi distribution f_x for $x = x'$, zero otherwise), due to carrier-carrier scattering. In the following, we will take for simplicity $\tau_{xx} = \tau_1$ for all x and $\tau_{xx'} = \tau_2$ for all $x \neq x'$. Notice that forward and exchange scattering processes (i.e., carrier-carrier interactions leaving the overall distribution

unchanged) contribute to τ_2 but not to τ_1, so the latter is expected to be somewhat longer.

Since f_x is a function of the carrier density N and of the (sub)band temperature T_x, we obtain a closed set of equations by including the rate equations [2]

$$\dot{N} + \frac{N}{\tau_s} = -\frac{i}{\hbar}\frac{1}{V}\sum_{\vec{k},v,c}(\rho_{cv}\vec{\mu}^*_{cv} - \vec{\mu}_{cv}\rho^*_{cv})\cdot\vec{E}(t) \tag{3.5}$$

$$\dot{T}_x + \frac{T_x - T_L}{\tau_h^x} = -\frac{i}{\hbar}\frac{1}{V}\sum_{\vec{k},v,c}\frac{\epsilon_x - \mu_x}{h_x}(\rho_{cv}\vec{\mu}^*_{cv} - \vec{\mu}_{cv}\rho^*_{cv})\cdot\vec{E}(t), \tag{3.6}$$

where, as before, τ_s and τ_h^x are the interband recombination and carrier-phonon relaxation lifetimes respectively, T_L is the lattice temperature, and μ_x and h_x are the chemical potential and heat capacity of (sub)band $x = c, v$. Notice that these equations are appropriate to either a bulk active region or one consisting of perfectly uncoupled QWs. The inclusion of interwell transport in MQW devices leads to additional contributions to χ_{ijkl} and is considered in the next two chapters. Finally, we point out that carrier heating via plasma absorption and two-photon absorption, which may also give a nonnegligible contribution to the FWM susceptibility, is not considered here.

As discussed in the previous chapter, in the presence of two excitation frequencies ω_p and ω_q, dynamic gratings in the gain and refractive index are formed through carrier density modulation (CDM), dynamic carrier heating (CH), and dynamic spectral hole burning (SHB). These mechanisms arise respectively from the dependence of the carrier density N, the carrier temperatures T_x, and the occupancy distribution and coherence functions $\rho_{xx'}$ on the optical field intensity, which involves a beat note at the pump-probe detuning frequency $\Omega = \omega_p - \omega_q = \omega_s - \omega_p$. Subsequent scattering of

the pump wave by these gratings produces a harmonic component of the polarization function ρ_{cv} at the converted signal frequency ω_s. Based on these arguments, we assume solutions of the form

$$N = N^{(0)} + \left(N^{(\Omega)} e^{-i\Omega t} + c.c.\right),$$

$$T_x = T_x^{(0)} + \left(T_x^{(\Omega)} e^{-i\Omega t} + c.c.\right),$$

$$\rho_{xx'} = \rho_{xx'}^{(0)} + \rho_{xx'}^{(\Omega)} e^{-i\Omega t} + \rho_{xx'}^{(-\Omega)} e^{i\Omega t},$$

$$\rho_{cv} = \rho_{cv}^{(\omega_p)} e^{-i\omega_p t} + \rho_{cv}^{(\omega_q)} e^{-i\omega_q t} + \rho_{cv}^{(\omega_s)} e^{-i\omega_s t}. \tag{3.7}$$

In order to calculate $\rho_{cv}^{(\omega_s)}$, and hence (through Eq. (3.1) and the definition of χ_{ijkl}) the FWM susceptibility tensor, we substitute (3.7) in the equations of motion (3.2)-(3.6), approximate the dependence of f_x on N and T_x with a Taylor series about quasi-equilibrium, and retain only terms up to third-order in the input field amplitudes. After some lengthy but straightforward algebra, we find the expression for χ_{ijkl} given in Appendix A, Eqs. (A.1)-(A.4), having general validity within the above framework and for isotropic in-plane dispersion relations.

A more compact expression is obtained by neglecting any dependence of $\vec{\mu}_{vc}$ on $|\vec{k}|$, which is a valid approximation in the absence of strong valence-band mixing [6] (i.e., near $\vec{k} = 0$, and/or in highly strained QW structures); the FWM susceptibility tensor can then be written as

$$\chi_{ijkl} = \left\langle \sum_{v',c'} (\vec{\mu}_{c'v'})_j (\vec{\mu}_{v'c'})_i \right\rangle \left\langle \sum_{v,c} (\vec{\mu}_{cv})_k (\vec{\mu}_{vc})_l \right\rangle (\chi_{CDM} + \chi_{CH}) +$$

$$+ \left\langle \sum_{v,c,v'} (\vec{\mu}_{cv})_j (\vec{\mu}_{vc})_i (\vec{\mu}_{cv'})_k (\vec{\mu}_{v'c})_l + \sum_{v,c,c'} (\vec{\mu}_{vc})_i (\vec{\mu}_{cv})_j (\vec{\mu}_{vc'})_l (\vec{\mu}_{c'v})_k \right\rangle \chi_{SHB(1)} +$$

$$+\left\langle \sum_{v,c,v'} (\vec{\mu}_{\bar{c}v})_j (\vec{\mu}_{vc})_i (\vec{\mu}_{cv'})_k (\vec{\mu}_{v'\bar{c}})_l + \sum_{v,c,c'} (\vec{\mu}_{vc})_i (\vec{\mu}_{c\bar{v}})_j (\vec{\mu}_{\bar{v}c'})_l (\vec{\mu}_{c'v})_k \right\rangle \chi_{SHB(2)}. \quad (3.8)$$

Here, $(\vec{\mu}_{vc})_i$ is the i^{th} component of $\vec{\mu}_{vc}$ (i = 1, 2 for TE and TM components), $< ... >$ denotes averaging over all directions of $\vec{k}$, and χ_{CDM}, χ_{CH}, $\chi_{SHB(1)}$, and $\chi_{SHB(2)}$ are scalar susceptibilities whose explicit expressions are given in Appendix A (these quantities account for the detuning frequency dependence of χ_{ijkl}, in a manner consistent with the approximation of Eq. (2.1)). Furthermore, in the last term on the right-hand side (the term proportional to $\chi_{SHB(2)}$), the index $\bar{c}$ is defined so that, given c, $\bar{c} \neq c$ (for instance, if c denotes spin-up, $\bar{c}$ denotes spin-down), and similarly for $\bar{v}$.

3.3 FWM Polarization Selection Rules

The polarization dependence of the FWM susceptibility is entirely contained in the summations over the indices c, v in Eqs. (A.1)-(A.4) [or Eq. (3.8)], where the dipole moment matrix elements in each product have been written in a time-ordered fashion. Notice the different structure of these summations for the cases of carrier density modulation and carrier heating on the one hand, and spectral hole burning on the other. As discussed below, this difference is easily explained in terms of the different nature of these mechanisms.

In the case of CDM and CH, the formation of the dynamic gratings (through beating of $E_k^{(p)}$ and $E_l^{(q)}$) and the generation of the converted signal $E_i^{(s)}$ (through scattering of $E_j^{(p)}$ by these gratings) are two entirely distinct processes, hence the two separate summations. In particular, as illustrated schematically in Fig. 3.1

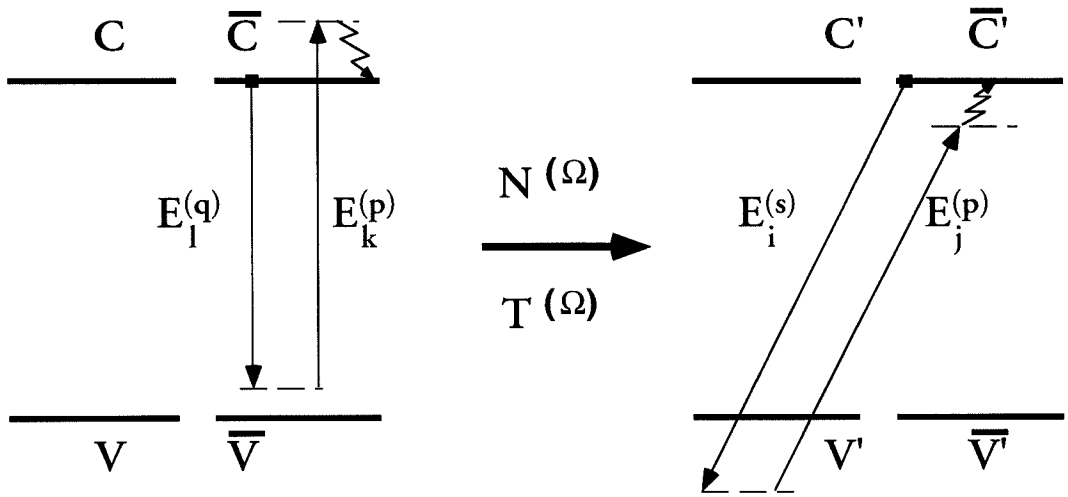

Figure 3.1: Photon transition diagrams illustrating the generation of the FWM signal by CDM (CH). Both the modulation of the carrier density (temperatures) and the scattering of the pump into the FWM signal occur through individual two-photon processes, as shown on the left and right diagrams respectively.

(left diagram), grating formation involves individual two-photon processes in which a photon is absorbed from the pump and simultaneously emitted into the probe wave. Provided that the final state of the electronic system in each such process is the same as the initial one ($\bar{c}$ in the figure), its occupation probability is correspondingly modulated at the detuning frequency, and then so are the overall carrier density and temperature (since they depend on the states occupancy integrated over the whole subband). Similarly, the pump wave is scattered by the resulting gratings into the FWM signal through individual two-photon processes (such as the one shown in the right diagram of Fig. 3.1), each of which also involves a single electronic transition (between $\bar{c}'$ and v' in the figure). It is important to emphasize that the

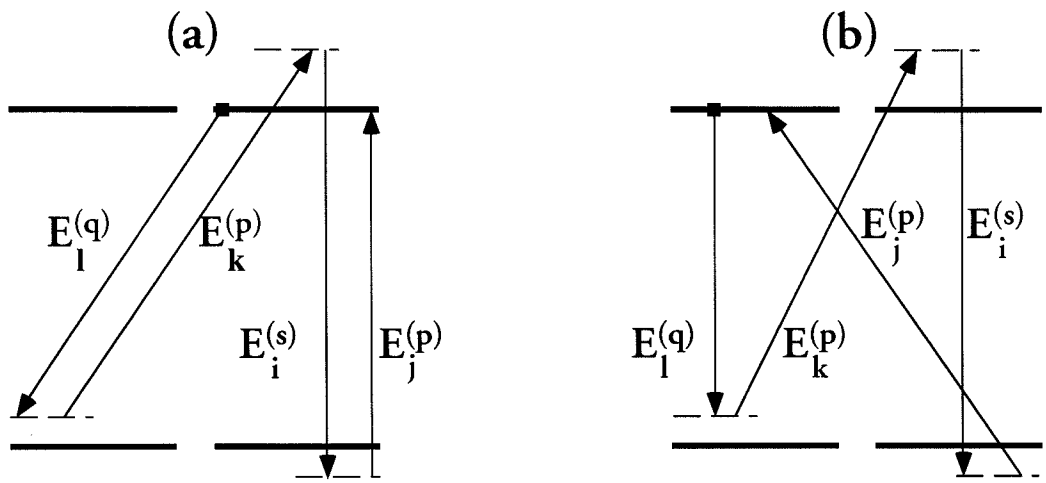

Figure 3.2: Photon transition diagrams illustrating the generation of the FWM signal by SHB. In the process shown in (a), the "dynamic gratings" result from modulation of the occupation probability of the initial state of the electronic system. In the process shown in (b), they result from modulation of the optically-induced phase coherence between the initial and the second intermediate state.

pump-scattering transitions need not be the same as those involved in the grating formation. Indeed, the states $(c, \bar{c}, v, \bar{v})$ on the one hand and $(c', \bar{c'}, v', \bar{v'})$ on the other, as given in Fig. 3.1, may even be localized in different spatial regions of the active medium. For this reason, FWM by CDM and CH is particularly suited to study the effect of transport processes on the nonlinear optical properties of a given device.

In the case of "spectral hole burning," however, gain/index modulation and pump scattering occur simultaneously through individual four-photon transitions (hence the single summation). Two qualitatively distinct types of processes are possible,

depending on the intermediate states, as illustrated in the diagrams of Fig. 3.2. In the case shown in Fig. 3.2a, the second intermediate state is the same as the initial one, and the gain and index modulation occurs directly through modulation of its occupancy (i.e., dynamic spectral hole burning, described by the term proportional to $\chi_{SHB(1)}$ in Eq. (3.8)). As shown in Fig. 3.2b, however, photons at the FWM frequency ω_s can also be generated in four-photon processes in which the second intermediate state is different from the initial one. Such processes (which contribute to the term proportional to $\chi_{SHB(2)}$ in Eq. (3.8)) can still be described in terms of gratings formation and pump scattering, but the gratings in this case result from modulation of the optically-induced relative phase coherence between the initial state and the second intermediate state. The corner frequency of the corresponding contribution to the FWM efficiency is set by the lifetime of this coherence, which, as discussed in connection with Eqs. (3.3)-(3.4), is the dephasing lifetime τ_2 (and not the relaxation lifetime τ_1 which limits the "ordinary" SHB contribution).

The FWM polarization selection rules can be immediately derived from Eq. (3.8), given knowledge of the dipole moment matrix elements $\vec{\mu}_{vc}$. For QW SOAs these are computed from the standard expressions for the spin-degenerate conduction and valence band states in a QW (see for instance Ref. [6]), given in Eq. (A.7) of Appendix A. Once substituted in the summations of Eq. (3.8), they result in the expressions listed in Appendix A [Eqs. (A.8)-(A.10)]. As can be seen from there, two qualitatively different sets of selection rules are found to apply for processes relying on modulation of the occupation probabilities and for processes relying on modulation of the phase

coherence between distinct states.

The former include CDM, CH and SHB processes of the type illustrated in Fig. 3.2a. All such processes are found to give a nonzero contribution only to tensor components of the form χ_{iikk}. In words, this means that: (I) formation of the dynamic gratings by modulation of the occupation probabilities can only occur through beating of the same components of the pump and probe waves (l and k either both TE or both TM); (II) the TE (TM) component of the pump can be scattered from these gratings into a FWM signal only with equal polarization (i = j).

On the other hand, FWM processes relying on modulation of relative coherences (i.e., "spectral hole burning" processes of the type shown in Fig. 3.2b) exhibit exactly the opposite behavior. The dynamic gratings in this case are induced through beating of orthogonal pump and probe components, and scatter each component of the pump into a signal with orthogonal polarization. Therefore, these processes contribute tensor components of the form χ_{ijij} and χ_{ijji} with $i \neq j$.

Incidentally, the same selcetion rules apply to the case of bulk SOAs, except that in that case any pair of orthogonal polarization states, not just TE and TM, could be used in the above discussion.

Finally we notice that these selection rules can be given a simple explanation for the special case of highly-strained QWs, in which, to a good degree of approximation, the relevant valence-band states have pure light-hole (for tensile strain) or heavy-hole (for compressive strain) character. In this case, it is well-known [6] that the optical transition between any pair of conduction-band and valence-band states

is only allowed to either TE- or TM-polarized light (never to both). The above selection rules then immediately follow by inspection of the diagrams of Figs. 3.1 and 3.2. Furthermore, compressive wells have negligible gain for TM waves, so that the FWM polarization selection rules further simplify to $\chi_{ijkl} = \chi_{1111}\delta_{i,1}\delta_{j,1}\delta_{k,1}\delta_{l,1}$, and no processes based on modulation of relative coherences are allowed.

3.4 Polarization Properties of the Converted Signal

Based on the results discussed in the previous section, we can write the FWM signal field at the SOA output in terms of the input fields as follows:

$$E_i^{(s)}(L) = \left(E^{(p)}(0)\right)^2 \left(E^{(q)}(0)\right)^* \left[\left(p_i \sum_{k=1}^{2} M_{iikk}\, p_k\, q_k^* \right) + M_{ilil}\Big|_{l\neq i} p_l p_i q_l^* + M_{illi}\Big|_{l\neq i} p_l^2 q_i^* \right], \tag{3.9}$$

where p_i and q_i are the i^{th} components of the polarization unit vector of the pump and the probe waves respectively at the SOA input. Furthermore, we defined the "transfer tensor" $M_{ijkl} = \chi_{ijkl} R_{ijkl}$, where the factor R_{ijkl} accounts for wave propagation effects; its expression is derived and given in Appendix B [see Eq. (B.11)].

Equation (3.9) can in principle be used for detailed numerical verifications of experimental results, provided all the relevant material and operational parameters are known. Here, we simply use it to provide a qualitative explanation of the experimentally observed polarization dependence of the FWM conversion efficiency [3]. First, notice that the last two terms in Eq. (3.9) are negligible in the sub-TeraHertz detuning range (where the contribution from SHB is small compared to those from CDM

and CH), since both M_{ilil} and M_{illi} $(i \neq l)$ are proportional to $\chi_{SHB(2)}$. In fact, we will neglect their contribution in most of the remainder (also see section 3.5).

With this approximation, the polarization selection rules appropriate to CDM and CH apply, and each component of the FWM signal is generated through scattering of the same component of the pump from two "types" of gain and index gratings, i.e., those formed by beating of the TE components of the input waves ("TE-induced gratings") and those formed by beating of their TM components ("TM-induced gratings"). The degree to which these two contributions to $E_i^{(s)}$ add up depends on the relative phase between the two types of gratings, which, in turn, varies with the angle between the polarizations of the beating waves. In particular, as illustrated in the inset of Fig. 3.3, if the pump and the probe have parallel polarizations, the two types of gratings are in phase, so that their contributions to $E_i^{(s)}$ add constructively and the FWM conversion efficiency is maximum. Vice versa, if the pump and the probe are orthogonally polarized, the two types of gratings are out of phase and tend to cancel each other. In QW active layers the amplitudes associated with the two contributions (i.e., M_{ii11} and M_{ii22}) are in general unequal (see Appendix A), so that this cancellation is incomplete. As a result, unlike the case of a perfectly isotropic gain medium, the FWM conversion efficiency of a QW SOA can be finite even for orthogonally polarized pump and probe waves.

This prediction was experimentally verified by measuring the FWM conversion efficiency for different combinations of the pump and probe polarizations. The SOA used has an active region consisting of three pairs of tensile and compressively strained

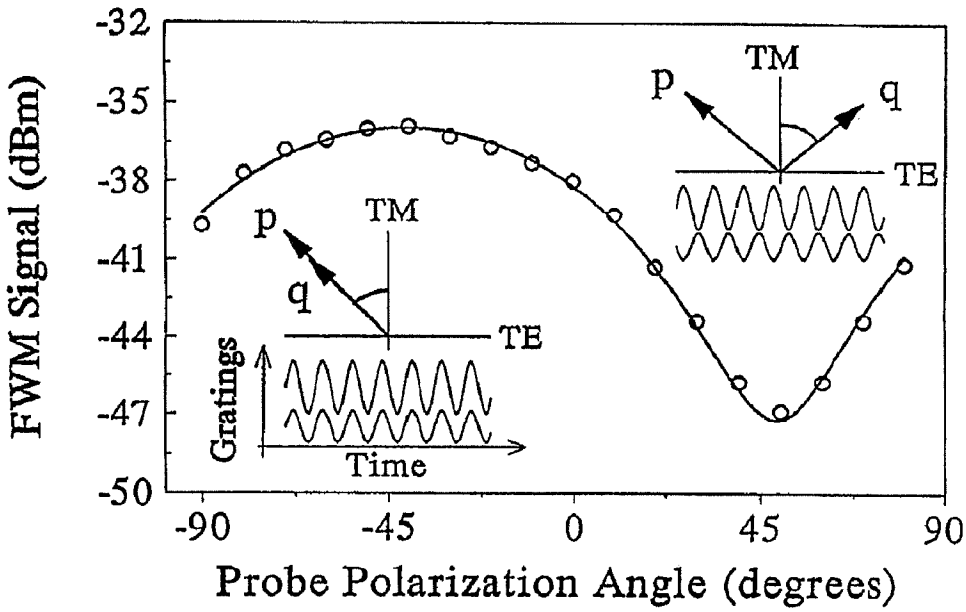

Figure 3.3: FWM signal power as a function of the linear polarization angle of the input signal relative to the TM direction, with a linearly polarized pump wave at -45°, and 1.5 nm detuning. The continuous line is a theoretical fit to Eq. (3.9), with fitting parameters M_{iikk}.

QWs, (incidentally, this device was designed for polarization-independent small signal gain [7]). A tunable fiber ring laser and a distributed feedback (DFB) semiconductor laser, followed by an EDFA, were used for the pump and the probe waves, and the optical spectrum at the output of the SOA was measured with an HP 70950A optical spectrum analyzer. The detuning frequency was chosen to be small enough (1.5 nm) so that the difference in the birefringence experienced by the two waves is small and thus the angle between their polarization states remains essentially constant throughout the interaction length. This ensures that any observed variation in the FWM conversion efficiency with the input polarizations is due to the interference

between the different types of gratings just described, as opposed to averaging effects associated with birefringence.

A typical set of data is shown in Fig. 3.3, where we plot FWM signal power as a function of the angle of linear polarization of the probe wave, with a linearly polarized pump wave at $-45°$. The continuous line is a fit to Eq. (3.9), with the coefficients M_{iikk} used as fitting parameters. These results are consistent with the discussion of the previous paragraph; in particular, notice the finite FWM conversion efficiency observed even in the case of orthogonal input polarizations.

Finally, notice that the model presented here also provides knowledge on how the polarization of the converted signal depends on that of the input waves. To illustrate, we selected the input polarizations such that the pump wave and the converted signal exit the SOA output linearly polarized at -45° and +45°, respectively. The nonzero components of M_{ijkl} were determined by fitting sets of data such as that in Fig. (3.3) to Eq. (3.9), for different pump polarizations. The result of this measurement is shown in Fig. 3.4, where the peaks shown are, from right to left, input signal, pump wave, (pump DFB sidemode), and converted signal (the detuning is 4 nm). The upper scan was taken directly at the SOA output, whereas for the middle scan a linear polarizer set at +45° was placed between the SOA and the detection stage (the lower trace is the ratio of the first two). Notice that the pump is suppressed by more than 30 dB, while the signal is essentially unattenuated by the polarizer. This idea may be considered as a scheme for pump suppression in wavelength conversion applications, although it has the disadvantage of requiring control of the input signal polarization.

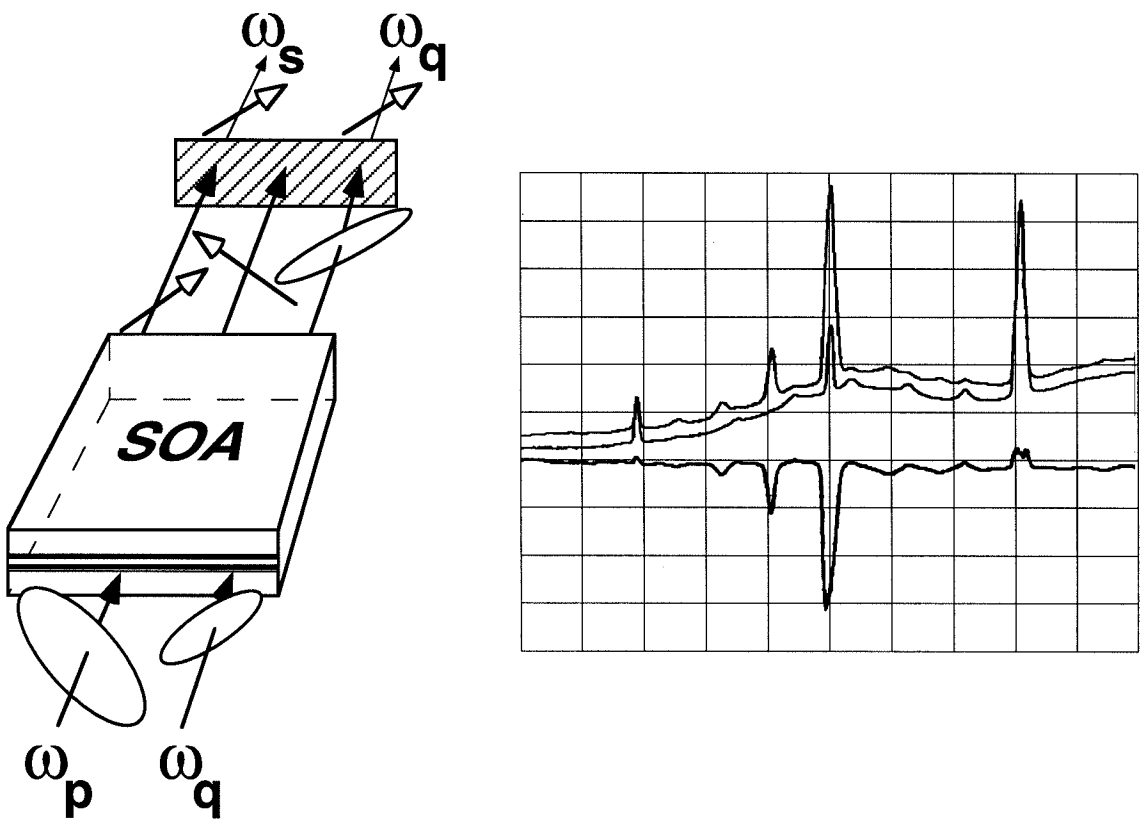

Figure 3.4: Illustration of the pump suppression experiment (left panel): at the output of the SOA the converted signal has polarization orthogonal to that of the pump, which is then suppressed using a linear polarizer. The right panel shows the SOA output spectrum before (upper trace) and after (middle trace) the polarizer (the lower trace is the ratio of the upper two). The pump (center peak) is suppressed by more than 30 dB, while the FWM signal (left peak) is essentially unattenuated.

Also, the ability to control the polarization of the FWM signal, illustrated with this example, may be of importance in optical switching applications.

3.5 FWM by Modulation of the Optically-Induced Phase Coherence between Spin-Degenerate States

In the presence of an external optical field, a relative phase coherence is established between two spin-degenerate states in, say, the conduction band (even if the dipole moment between them is obviously zero), if the field couples both states to a same state in the valence band. In particular, if the optical intensity involves a beat note at some frequency Ω (as in the case of FWM), this phase coherence (described in Eqs. (3.2)-(3.4) by the density matrix elements $\rho_{c\bar{c}}$ with $\bar{c} \neq c$) can be modulated at the same frequency. As was discussed in 3.3, this can only occur if the beating involves a TE-polarized pump wave and a TM-polarized probe wave (or vice versa); the TE (TM) component of the pump is then scattered into a TM-(TE-)polarized FWM signal.

This contribution to the converted signal (described by the last two terms on the right-hand side of Eq. (3.9)) can be easily isolated by setting the polarization state of one of the input waves exactly along the TE direction, and that of the other along the TM direction. The observation of a FWM signal under this condition would allow to study the dephasing dynamics of the spin-spin phase coherence just described. In particular, by measuring the corresponding FWM conversion efficiency versus detuning frequency (and appropriately subtracting all propagation effects), one

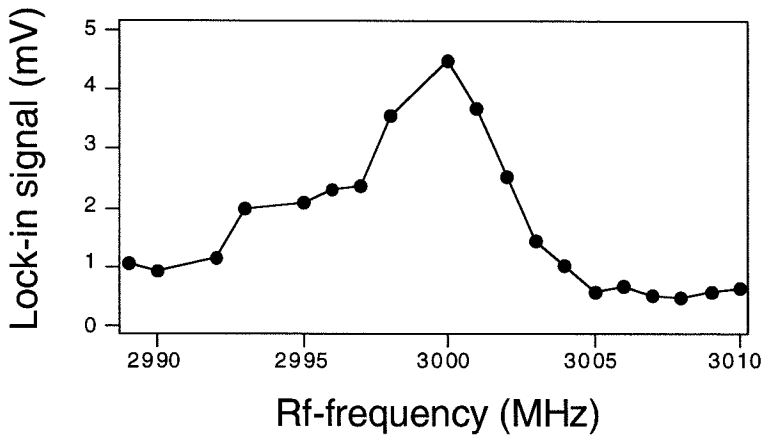

Figure 3.5: FWM signal generated with a TE-polarized pump wave and a TM-polarized probe wave, as measured with a lock-in amplifier.

could extrapolate the dephasing lifetime τ_2.

However, this FWM mechanism is strongly limited in the device used in these experiments, due to the high degree of birefringence typical of most (strained) MQW SOAs. We estimated the refractive index experienced by TM (TE) waves by measuring the frequency spacing between neighboring TM (TE) residual modes of the SOA; the difference $\Delta n = n_{TM} - n_{TE}$ was found to be quite large, approximately equal to 3×10^{-2}. As a result, the phase mismatch between the input waves is in this case significant. This leads to a strong reduction in the FWM conversion efficiency, which can be quantified using Eq. (B.11) of Appendix B for M_{illi} $(i \neq l)$. For simplicity, we assume that the total optical intensity is uniform along the interaction length (as appropriate to the high-saturation regime of operation), and furthermore we neglect the frequency dependence of the gain coefficient and refractive index (as appropriate

to sub-TeraHertz detuning frequencies). Then, the magnitude squared of M_{illi} $(i \neq l)$ is found to be smaller than that of M_{iikk} by almost 3 orders of magnitude. In other words, the phase matching requirement reduces the conversion efficiency for FWM with a TE-polarized pump wave and a TM-polarized probe wave (or vice versa) by almost 30 dB.

In a preliminary experiment, we found the FWM conversion efficiency under these conditions to be exceedingly small, so that a lock-in amplifier had to be used in conjunction with our optical heterodyne system to even see the converted signal (the experimental setup is similar to that described in section 6.2). The data shown in Fig. 3.5 give the TM-polarized FWM signal as measured with the lock-in amplifier, for a TE-polarized pump wave and a TM-polarized probe wave, and with detuning frequency of a few TeraHertz (i.e., large enough that spurious contributions resulting from any slight polarization misalignment of the input waves should be negligible). However, we could not map this FWM signal versus detuning frequency, due to its low signal-to-noise ratio (and to the observed oscillations in its strength versus Ω resulting from the above mentioned birefringence-induced phase mismatch).

Bibliography

[1] G. P. Agrawal, "Population pulsations and nondegenerate four-wave mixing in semiconductor lasers and amplifiers," *J. Opt. Soc. Am. B*, vol. 5, pp. 147–158, 1988.

[2] A. Uskov, J. Mϕrk, and J. Mark, "Wave mixing in semiconductor laser amplifiers due to carrier heating and spectral hole burning," *IEEE J. Quantum Electron.*, vol. 30, pp. 1769–1781, 1994.

[3] R. Paiella, G. Hunziker, J. Zhou, K. J. Vahala, U. Koren, and B. I. Miller, "Polarization properties of four-wave mixing in strained semiconductor optical amplifiers," *IEEE Photon. Technol. Lett.*, vol. 8, pp. 773–775, 1996.

[4] R. Paiella, G. Hunziker, U. Koren, and K. J. Vahala, "Polarization-dependent optical nonlinearities of multiquantum-well laser amplifiers studied by four-wave mixing," *IEEE J. Select. Topics Quantum Electron.*, vol. 3, pp. 529–540, 1997.

[5] S. Schmitt-Rink, D. Bennhardt, V. Heuckeroth, P. Thomas, P. Haring, G. Maidorn, H. Bakker, K. Leo, D. Kim, J. Shah, and K. Kohler, "Polarization dependence of heavy- and light-hole quantum beats," *Phys. Rev. B*, vol. 46, pp. 10460–10463, 1992.

[6] W. W. Chow, S. W. Koch, and M. Sargent III, *Semiconductor-Laser Physics.* Berlin, Germany: Springer-Verlag, 1994.

[7] M. A. Newkirk, B. I. Miller, U. Koren, M. G. Young, M. Chien, R. M. Jopson, and C. A. Burrus, "1.5 μm multiquantum-well semiconductor optical amplifier with tensile and compressively strained wells for polarization-independent gain," *IEEE Photon. Technol. Lett.*, vol. 4, pp. 406–408, 1993.

Chapter 4

Interwell Carrier Transport Studied by Polarization-Resolved FWM

4.1 Introduction

Four-wave mixing in SOAs is a powerful spectroscopic technique to study the optical nonlinearities of semiconductor gain media. In the simplest FWM configuration, two copolarized cw waves, the pump and the probe, are coupled into the SOA waveguide, and the intensity of the resulting FWM signal is measured as a function of the pump-probe detuning frequency. This approach has been successfully used to study the ultrafast intraband carrier dynamics of semiconductor active layers (such as carrier heating and spectral hole burning), and to measure, in the frequency domain, the corresponding lifetimes [1], [2].

Further applications of FWM spectroscopy can be devised based on more complex configurations. In particular, in this chapter we present an experiment in which FWM is used to investigate interwell carrier transport in a multiquantum-well (MQW) SOA [3]. As discussed in chapter 2, transport processes in MQW active layers effectively increase the nonlinear gain compression [4]–[11], so that it should be possible to directly study these processes in a properly designed FWM experiment. In the following, we will describe one such experiment based on the polarization properties of FWM in a SOA consisting of alternating pairs of tensile and compressively strained QWs. We will also extend the theoretical model of the previous chapter to account for interwell coupling [12], which then allows us to infer from the experimental data an estimate for the interwell transport lifetime. As an aside, in the final section of the chapter, we show how a similar polarization-resolved FWM configuration provides an extremely simple method of measuring the interband stimulated recombination lifetime τ_s [13].

4.2 Measurement of the Interwell Carrier Transport Lifetime in an Alternating-Strain Multiquantum-Well Optical Amplifier

As pointed out in the previous chapter, in conjunction with Fig. 3.1, an important feature of FWM by carrier density modulation (and carrier heating) is that the formation of the dynamic gratings and the scattering of the pump wave into the converted signal are entirely distinct processes. As such, they do not even need to take place in the same spatial region of the SOA. For example, in a MQW SOA with interwell cou-

pling, we may consider a FWM process in which the gratings are formed in one well and then transferred to a neighboring well where the pump is then scattered [3], [10]. The strength of this process strongly depends on the interwell transport rate $1/\tau_t$; in particular, we expect it to become negligibly small at detuning frequencies much larger than this rate. As a result, FWM can be used to measure τ_t, provided that the contribution to the overall FWM signal associated with the above process can somehow be isolated from all other contributions. As will be shown in the following, this can be done by taking advantage of the FWM polarization selection rules in an alternating-strain SOA. This technique provides an extremely clean way of studying interwell transport, which is an issue of considerable importance given its relation to the maximum direct modulation bandwidth of MQW lasers [4]–[9].

The FWM polarization configuration used in this work is illustrated in Fig. 4.1. The SOA consists of three alternating pairs of a 160 Å tensile and a 75 Å compressively strained QWs, separated by 125 Å barriers, and was designed for polarization independent small-signal gain [14]. The probe wave is linearly polarized along the growth axis (TM polarization), whereas both the TE and the TM components of the pump wave are nonzero (and equal to each other for simplicity). We only consider detuning frequencies below 100 GHz, so that carrier density modulation provides the strongest FWM mechanism.

With this choice for the input polarization states, the beating of the pump and the probe waves only results in "TM-induced gratings," as shown schematically in the upper panel of Fig. 4.1. Since compressive wells have negligible gain for TM-polarized

light, these gratings can be generated only in the tensile wells. Here, each polarization component of the pump is then scattered into the same component of the FWM signal. Furthermore, if the carrier density modulation underlying the dynamic gratings can be transfered into the neighboring compressive wells, an additional contribution to the TE component of the converted signal can be generated there. The lower panel of Fig. 4.1 gives a schematic representation of the different processes contributing to the FWM signal field $\vec{E}^{(s)}$, which can accordingly be written as

$$E_1^{(s)} = R_{1122}\left(\chi_{1122}^T + \chi_{1122}^{C\leftarrow T}\right)\left(E^{(p)}\right)^2\left(E^{(q)}\right)^*$$

$$E_2^{(s)} = R_{2222}\chi_{2222}^T\left(E^{(p)}\right)^2\left(E^{(q)}\right)^*. \tag{4.1}$$

In these expressions, χ_{ijkl} is as defined in the previous chapter, the subscripts $i = 1, 2$ denote the TE and TM directions respectively, and we have taken $\vec{E}^{(q)} = \hat{e}_2 E^{(q)}$ and $\vec{E}^{(p)} = (\hat{e}_1 + \hat{e}_2)\, E^{(p)}$. Furthermore, the superscripts T and C are used to distinguish between quantities in the tensile and compressive wells, and the term proportional to $\chi_{1122}^{C\leftarrow T}$ describes the contribution involving interwell transport.

Then, information about the interwell coupling is obtained by plotting P_1^s/P_2^s (P_i^s denoting the optical power in the i^{th} component of the FWM signal) versus detuning frequency. The wave propagation factors R_{iikk} can be regarded as independent of Ω over the small detuning range (< 100 GHz) considered in this work (see Appendix B), so that we may regard $P_1^s/P_2^s\,(\Omega) \propto \left|\left(\chi_{1122}^T + \chi_{1122}^{C\leftarrow T}\right)/\chi_{2222}^T\right|^2$. Consequently, we expect this curve to approach a constant value (proportional to $\left|\chi_{1122}^T/\chi_{2222}^T\right|^2$) as Ω exceeds the interwell transport rate. Any feature observed at lower detuning frequencies is ascribed to interwell coupling.

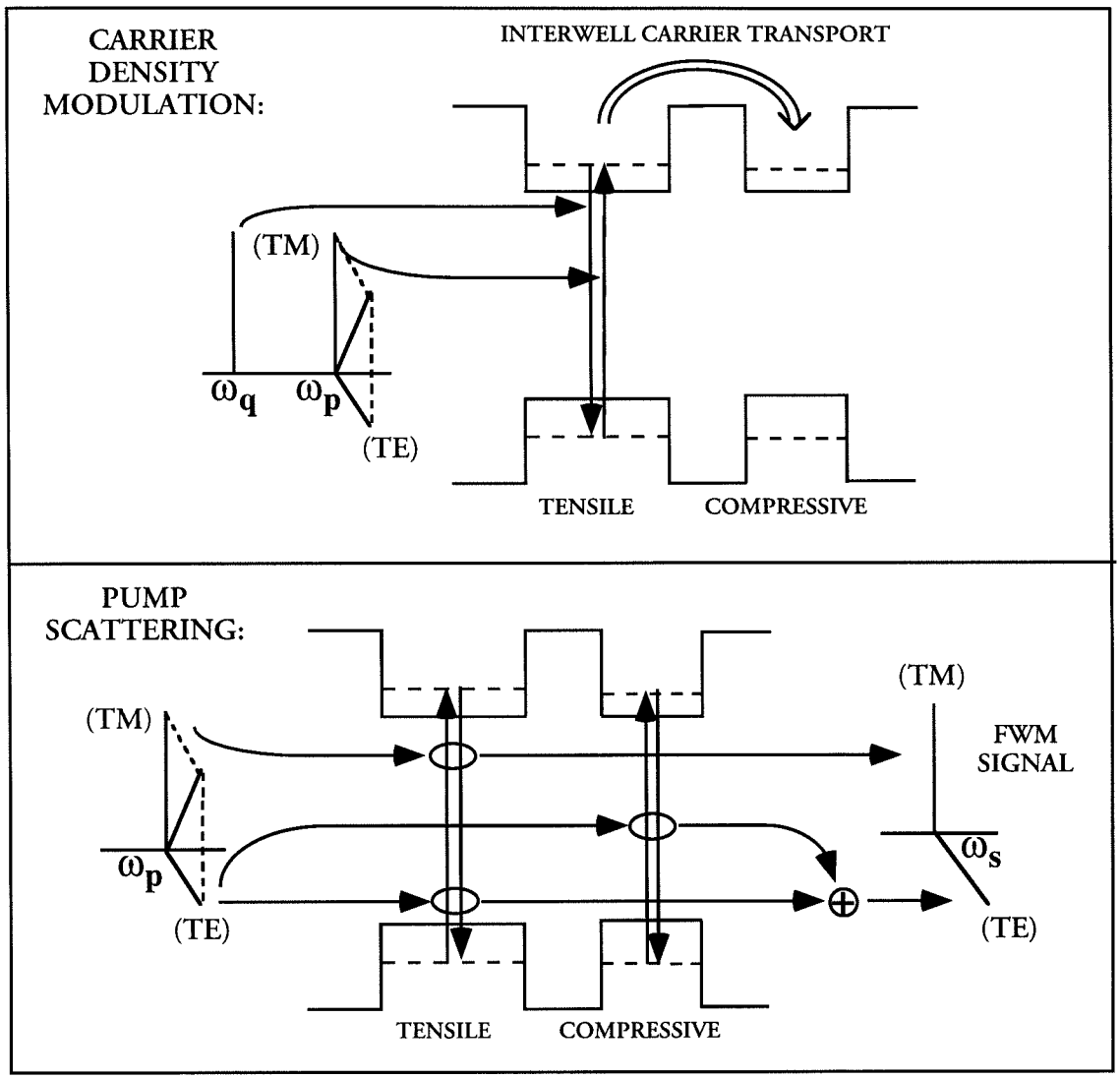

Figure 4.1: Schematics of the FWM processes taking place with the polarizations used in the interwell transport lifetime measurement. As shown in the upper panel, modulation of the carrier density is generated directly (through beating of the TM components of the input waves) only in the tensile wells, from which it can then be transferred to the neighboring compressive wells. Each polarization component of the pump is then correspondingly scattered into the same component of the FWM signal as shown in the lower panel.

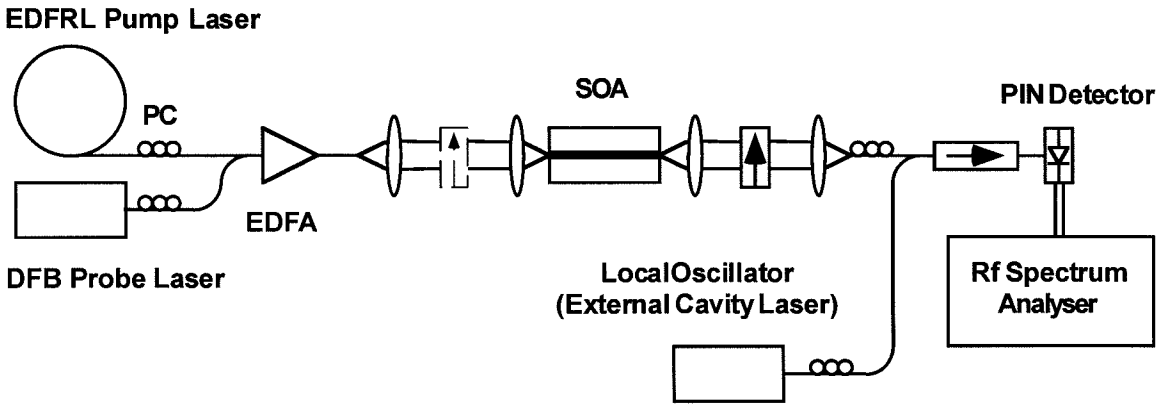

Figure 4.2: Experimental setup for the interwell transport lifetime measurement.

The experimental setup used to carry out this measurement is shown in Fig. 4.2. The pump wave (provided by a tunable Erbium-doped fiber ring laser (EDFRL) built in the lab) and the probe (provided by a commercial DFB laser) are combined in a fiber bidirectional coupler, amplified in a high-power EDFA, and then coupled into the SOA. The desired polarization states at the input of the SOA are obtained with two polarization controllers (PCs) immediately following the two lasers. At the output of the SOA a linear polarization filter is used to select the TE or the TM component of the FWM signal, which is then detected using a optical heterodyne system. In particular, the SOA output beam is combined with an optical local oscillator (LO) with frequency closely tuned to ω_s, and the beat note between the LO and the FWM signal is then measured at a constant frequency in a radio-frequency (rf) spectrum analyzer.

The results are shown in Fig. 4.3, where we plot the measured optical power in the TE and TM components of the FWM signal (Fig. 4.3a), and their ratio (Fig.

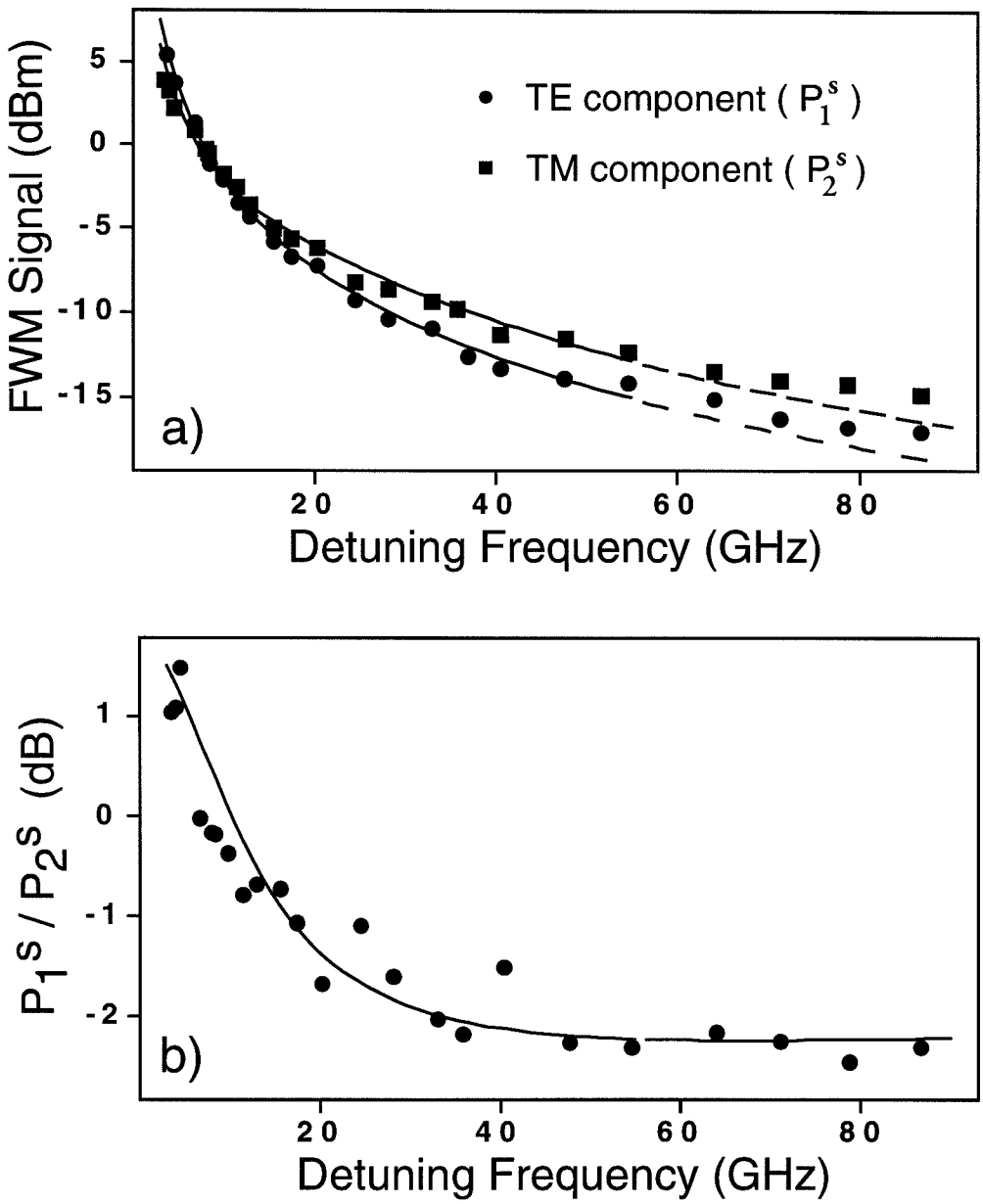

Figure 4.3: Results of the interwell transport lifetime measurement: TE (circles) and TM (squares) components of the FWM signal (a), and their ratio (b) versus detuning frequency. The continuous lines are fits to the theory discussed in the text. As emphasized by the dashing, the fit becomes inaccurate in (a) for $\Omega >$ about 50 GHz, where carrier heating, not included in the fit, becomes important (however, since this contribution is approximately the same for the TE and TM components, the fit remains good for their ratio in (b)).

4.3b). These data are consistent with the previous discussion: in particular, the ratio approaches a constant at the larger values of Ω, while for Ω smaller than approximately 40 GHz an obvious deviation from this constant value is observed, which we regard as a signature of interwell coupling. Notice that with this measurement interwell coupling is observed as a qualitatively new feature in the experimental results, and from the data we can directly obtain an upper limit to the interwell equilibration rate $1/\tau_t$, 40 GHz in this device.

For more quantitative results, we fit the experimental data of Fig. 4.3 to the theoretical framework of the previous chapter, properly generalized to include a simple model for the interwell carrier dynamics. In particular, we assume that the transfer of carriers between neighboring wells mainly results from phonon-assisted capture/escape processes between 2D QW states and semiclassical wavepackets of 3D states localized near the same well [6], [7]. We describe the dynamics of these wavepackets as dominated by classical diffusion. Drift, on the other hand, is expected to be of minor importance, due to the nearly flat-band conditions typical of forward-bias SOA operation [6], [7]. Tunneling is also neglected, which is a fair assumption given the relatively large barrier width L_b (125 Å) in the SOA under study. Furthermore, the dynamics of holes, which are known to a have a shorter capture lifetime [15], is not considered explicitly.

With these assumptions, the Bloch equations (3.2)-(3.4) remain appropriate, except that two distinct sets of such equations are required for the two types of wells. The interwell coupling is then introduced in the model by replacing the rate equation

for the carrier density, Eq. (3.5), by the following

$$\dot{N}_{2D}^{X} + \left(\frac{1}{\tau_s} + \frac{1}{\tau_{esc}^{X}}\right) N_{2D}^{X} - \frac{N_{3D}^{X}}{\tau_{cap}^{X}} = -\frac{i}{\hbar}\frac{1}{V^{X}} \sum_{\vec{k},v,c} \left(\rho_{cv}^{X}\vec{\mu}_{cv}^{X*} - \vec{\mu}_{cv}^{X}\rho_{cv}^{X*}\right) \cdot \vec{E}(t)$$

$$X = T, C \tag{4.2}$$

$$\dot{N}_b + \frac{N_b}{\tau_s} = D\frac{\mathrm{d}^2 N_b}{\mathrm{d}x^2}. \tag{4.3}$$

Here, N_{2D} denotes the number density of electrons confined inside the QW under consideration; N_{3D} is the density of unconfined electrons localized near the same QW so as to be involved in the capture/escape processes; $N_b(x)$ is the density of unconfined electrons as a function of position x along the growth axis; τ_{esc} and τ_{cap} are the quantum escape and capture lifetimes; D is the diffusion coefficient; and again the superscript X = T, C refers to quantities of tensile and compressive wells.

In principle, the rate equations for the carrier temperatures should also be generalized in a similar fashion; however, in the experiment described here the detuning frequency is kept small enough that inclusion of carrier heating effects is not critical. Finally, we point out that when the interwell coupling results from resonant tunneling, this description becomes inappropriate and one has to include the coupling directly in the density-matrix equations of motion; this case will be considered in the next chapter.

The coupled equations (4.2)-(4.3) can be solved given an appropriate set of boundary conditions satisfied by $N_b(x)$ near each QW. For instance, we may require $N_b(x_i^T \pm L_w^T/2) = N_{3D}^T$ and $D\frac{\mathrm{d}N_b}{\mathrm{d}x}(x_i^T \pm L_w^T/2) = \pm\frac{L_w^T}{2}\left(\frac{N_{3D}^T}{\tau_{cap}^T} - \frac{N_{2D}^T}{\tau_{esc}^T}\right)$, where x_i^T denotes the position of the center of the i^{th} tensile well, of width L_w^T (and similarly for each compressive well). Notice that these conditions introduce further approximations to the model,

since they implicitly assume an infinite chain of pairs of oppositely strained wells, and furthermore neglect any diffusion process occurring over the finite width of the wells.

In any case, regardless of the detailed form of the boundary conditions (provided they are linear), the solution of Eq. (4.3) can be used to recast Eq. (4.2) in the following form (in the frequency domain)

$$\begin{aligned}
\left(-i\Omega+\frac{1}{\tau_e^T}\right)N_{2D}^{T(\Omega)}-\frac{N_{2D}^{C(\Omega)}}{\tau_t^{T\leftarrow C}}=\\
-\frac{i}{\hbar}\frac{1}{V^T}\sum_{\vec{k},v,c}\left[\rho_{cv}^{T(\omega_p)}\left(\vec{\mu}_{cv}^T\cdot\vec{E}_q\right)^*-\vec{\mu}_{cv}^T\cdot\vec{E}_p\left(\rho_{cv}^{T(\omega_q)}\right)^*\right],\\
\left(-i\Omega+\frac{1}{\tau_e^C}\right)N_{2D}^{C(\Omega)}-\frac{N_{2D}^{T(\Omega)}}{\tau_t^{C\leftarrow T}}=\\
-\frac{i}{\hbar}\frac{1}{V^C}\sum_{\vec{k},v,c}\left[\rho_{cv}^{C(\omega_p)}\left(\vec{\mu}_{cv}^C\cdot\vec{E}_q\right)^*-\vec{\mu}_{cv}^C\cdot\vec{E}_p\left(\rho_{cv}^{C(\omega_q)}\right)^*\right]
\end{aligned}\tag{4.4}$$

where $1/\tau_e^T$ is an effective escape rate from each tensile well, and $1/\tau_t^{C\leftarrow T}$ is the overall transport rate from each tensile well to the neighboring compressive wells.

Simple expressions for these quantities can be obtained if (I) we use the boundary conditions on N_b mentioned above, (II) we take the diffusion length $L_D=\left|\sqrt{\frac{D\tau_s}{1-i\Omega\tau_s}}\right|$ to be much larger than the barrier width L_b (which is certainly the case at the detuning frequencies of interest here), (III) we neglect differences between the two types of wells. The result is

$$\begin{aligned}
\frac{1}{\tau_t}&=\frac{1}{2\tau_{esc}}\frac{1}{1-i\Omega\tau_{cap}L_b/L_w},\\
\frac{1}{\tau_e}&=\frac{1}{\tau_s}+\frac{1}{2\tau_{esc}}\frac{1-i\Omega 2\tau_{cap}L_b/L_w}{1-i\Omega\tau_{cap}L_b/L_w}.
\end{aligned}\tag{4.5}$$

Notice how both rates are complex-valued functions of the detuning frequency Ω (the frequency of the carrier density modulation being coupled between adjacent wells).

This dependence results from the Ω dependence of the diffusion length; the complex character implies that a phase shift is introduced in the escape/transport process. At low detuning frequencies, where diffusion is essentially instantaneous, interwell transport is mainly limited by quantum escape, and $\tau_t \approx \tau_e \approx 2\tau_{esc}$ (the factor of two appears because, if the two types of wells have equal capture lifetime, as assumed in Eq. (4.5), each escaped carrier from a well can be transferred to an adjacent well or recaptured in the same well with equal probability).

In any case, given the rate equations (4.4) and the density-matrix equations (3.2)-(3.4) for both types of wells, one can proceed as before to solve for the FWM susceptibility tensor components. The contribution from each compressive well can be written as $\chi_{ijkl}|_C = \chi^C_{ijkl} + \chi^{C\leftarrow T}_{ijkl}$, where (including the carrier density modulation terms only, as appropriate to the present experiment)

$$\chi^C_{ijkl} = \left\langle \sum_{v',c'} (\vec{\mu}^C_{c'v'})_j (\vec{\mu}^C_{v'c'})_i \right\rangle \left\langle \sum_{v,c} (\vec{\mu}^C_{cv})_k (\vec{\mu}^C_{vc})_l \right\rangle \chi^{C\leftarrow C}_{CDM},$$

$$\chi^{C\leftarrow T}_{ijkl} = \left\langle \sum_{v',c'} (\vec{\mu}^C_{c'v'})_j (\vec{\mu}^C_{v'c'})_i \right\rangle \left\langle \sum_{v,c} (\vec{\mu}^T_{cv})_k (\vec{\mu}^T_{vc})_l \right\rangle \chi^{C\leftarrow T}_{CDM}, \tag{4.6}$$

(the contribution from each tensile well can be written in exactly the same manner with the superscripts T and C interchanged). Again, we are neglecting here any dependence of $\vec{\mu}_{cv}$ on $|\vec{k}|$, as appropriate to highly strained QWs; full expressions for the scalar susceptibilities just defined are given in Appendix A [Eqs. (A.11) and (A.12)].

The continuous lines in Fig. 4.3 are the fits to the model theory just described. The agreement with the experimental data is excellent, except for the points at detuning frequencies in excess of about 50 GHz, where carrier heating (not included in the

model) is known [2] to cause an increase in the FWM conversion efficiency. Note, however, that since this increase is approximately the same for both the TE and TM components, the fit remains good for their ratio in Fig. 4.3b. From this fit, we obtain an estimate of 16 psec for the low-detuning interwell transport lifetime τ_t (as well as for τ_e). Furthermore, if we assume that τ_t and τ_e are related to the quantum capture/escape lifetimes as given by Eq. (4.5), we find $\tau_{esc} \approx 8$ psec, and $\tau_{cap} \approx 1.5$ psec; we point out, however, that these estimates further rely on the simplifying assumptions used to derive Eq. (4.5), and they should be interpreted accordingly. Anyway, we note that these values are consistent with previous reports [4]-[11], and with the observed maximum modulation bandwidth of QW lasers.

4.3 Measurement of the Stimulated Recombination Lifetime

A polarization-resolved FWM configuration similar to the one described in the previous section can be used to measure the stimulated recombination lifetime τ_s in a very straightforward manner [13]. As discussed in chapter 2, this lifetime sets the speed of the carrier density modulation contribution to the FWM signal. More in general, in SOA devices based on cross-gain or cross-phase modulation (e.g., for wavelength conversion), τ_s is directly related to the maximum bit-rate at which the device can operate, and therefore much effort has been recently devoted to shorten it (see, for instance, Refs. [16] and [17]). This time constant can be directly obtained by measuring the 3-dB corner frequency of the FWM frequency response at very low

detuning frequencies (less than a GigaHertz). This, however, is complicated by the strong variation in the FWM signal power with Ω in this frequency range, so that extremely accurate readings of both power and frequency are required. As it will become clear in the following, the technique presented here overcomes this problem in a very simple way (it should be mentioned, however, that since it requires both TE and TM transitions, this method is not suitable for SOAs with only compressively strained QWs).

The experiment is schematically explained in Fig. 4.4. Instead of using a laser beam as the probe, we use the broadband amplified spontaneous emission (ASE) noise power from an EDFA, filtered in a 200 GHz optical bandpass filter centered about the pump laser frequency (otherwise, the experimental setup is the same as shown in Fig. 4.2). We refer to the ASE as the probe, despite the fact that it is not a single-frequency wave but rather an incoherent superposition of frequencies. Furthermore, the ASE noise power is polarized along the TM direction before being coupled into the SOA, along with a single-frequency pump wave polarized at 45° with respect to the growth axis (i.e., equal TE and TM components). The TM components of these input waves will modulate the carrier density at all frequencies within the half-bandwidth of the optical bandpass filter (0-100GHz). This modulation will result in gain and index modulation for both polarization modes in the SOA, and thus generate a FWM signal along both the TE and the TM directions (from the M_{1122} and M_{2222} terms in Eq. 3.9, respectively).

At the output of the SOA, we select only the TE polarized waves by way of

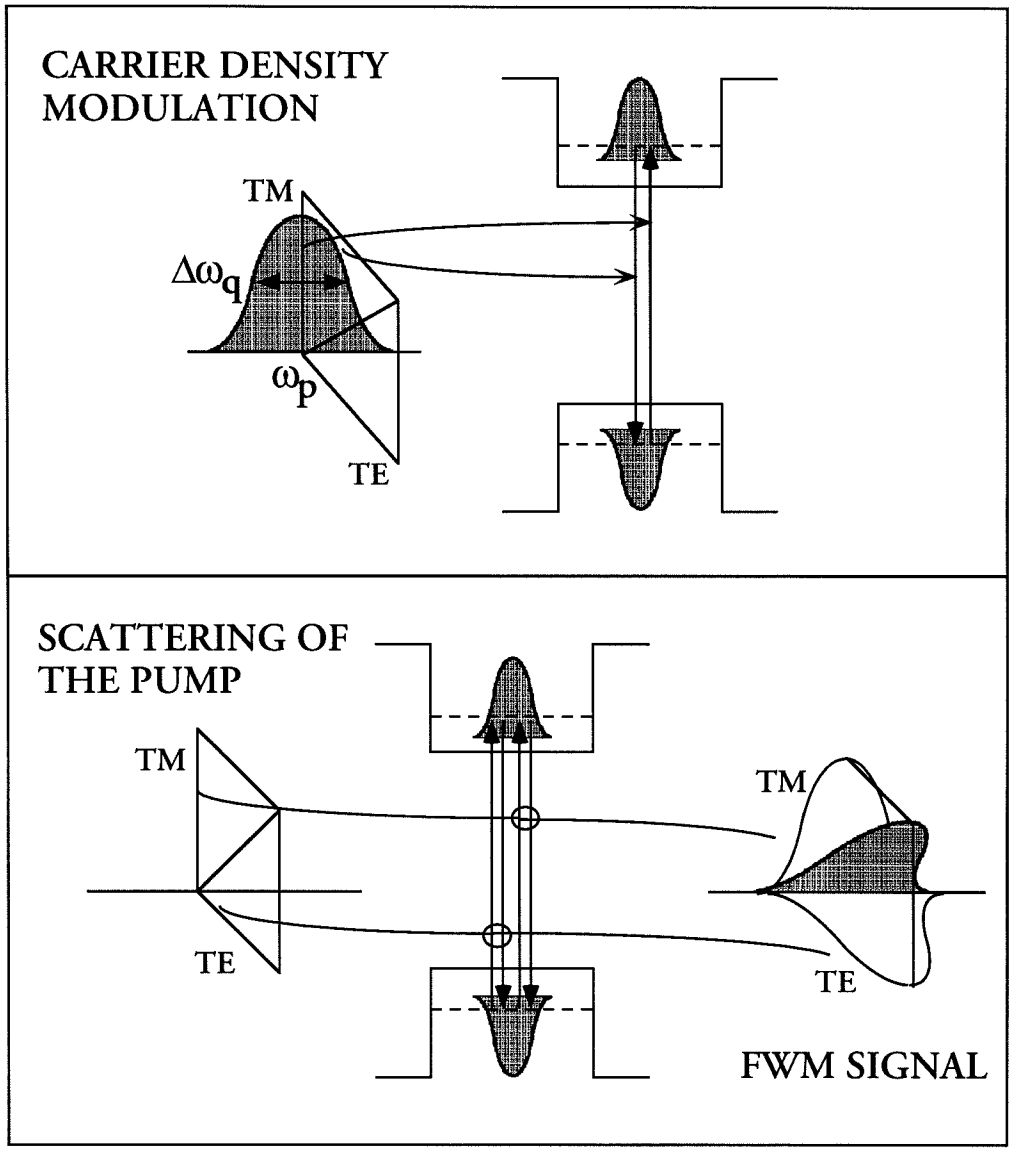

Figure 4.4: Schematics of the FWM processes taking place with the polarizations used in the recombination lifetime measurement. In the upper panel, we show the modulation of the carrier density by beating of the input waves (TM components only). In the lower panel, we show the scattering of each pump component into the corresponding FWM component. The probe (and, consequently, the FWM signal) is not a single frequency source but rather a continuum of frequencies within a 200 GHz bandwidth.

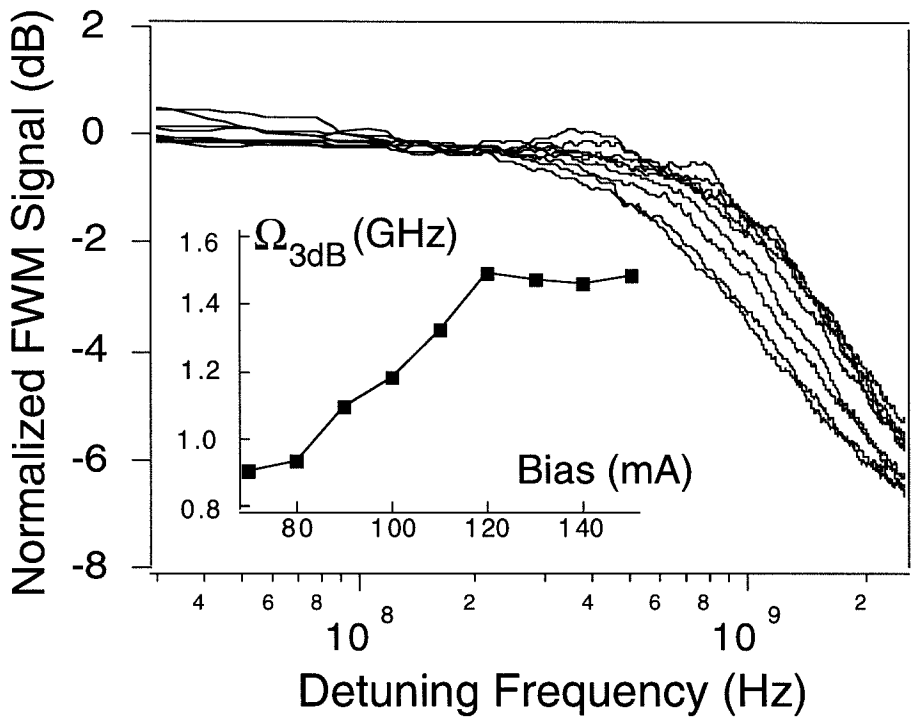

Figure 4.5: Results of the recombination lifetime measurement. The FWM efficiency is plotted as a function of detuning frequency for SOA bias currents ranging from 50 to 150 mA (left to right). The roll-off associated with the stimulated recombination lifetime is clearly seen; the corresponding 3dB corner frequency ($1/2\pi\tau_s$) is shown in the inset as a function of the bias current.

a polarization filter. This yields a signal which, upon direct detection, contains the pump-FWM signal beatnote in the rf-frequency domain. On the other hand, since the probe has no component along TE, the pump-probe beatnote (which would otherwise overpower the pump-FWM rf signal) is suppressed with the polarizer. Furthermore, the use of a broad superposition of probe frequencies centered around the pump frequency allows us to map out the detuning frequency dependence of the FWM efficiency (at low values of Ω) in just one scan of the rf-spectrum analyzer. The TM

component of the SOA output beam, upon direct detection, gives the pump-probe beatnote (the TM pump-FWM signal beatnote is much weaker). In fact, we used this latter rf signal to normalize out (from the TE products) the rf-frequency dependence of the probe envelope and the detection system.

The results are shown in Fig. 4.5, where we plot the normalized FWM signal versus detuning frequency, measured in an alternating-strain MQW SOA (the same device used in the interwell transport lifetime measurement), for different values of the SOA bias current. The corner frequency $1/2\pi\tau_s$ appears very clearly, from which the stimulated recombination lifetime is immediately inferred. This measurement then allows us to plot τ_s versus the bias current, as shown in the inset of the figure; incidentally, notice how this curve reflects the change in the saturated gain of the SOA with the injection current. More in general, the technique presented here should be quite useful in the characterization of any optoelectronic device whose performance depends on τ_s.

Bibliography

[1] K. Kikuchi, M. Kakui, C. E. Zah, and T. P. Lee, "Observation of highly nondegenerate four-wave mixing in 1.5 μm traveling-wave semiconductor optical amplifiers and estimation of nonlinear gain coefficient," *IEEE J. Quantum Electron.*, vol. 28, pp. 151–156, 1992.

[2] J. Zhou, N. Park, J. W. Dawson, K. J. Vahala, M. A. Newkirk, and B. I. Miller, "Terahertz four-wave mixing spectroscopy for study of ultrafast dynamics in a semiconductor optical amplifier," *Appl. Phys. Lett.*, vol.63, pp. 1179 – 1181, 1993.

[3] R. Paiella, G. Hunziker, K. J. Vahala, and U. Koren, "Measurement of the interwell carrier transport lifetime in multiquantum-well optical amplifiers by polarization-resolved four-wave mixing," *Appl. Phys. Lett.*, vol. 69, pp. 4142-4144, 1996.

[4] W. Rideout, W. F. Sharfin, E. S. Koteles, M. O. Vassell, and B. Elman, "Well-barrier hole burning in quantum well lasers," *IEEE Photon. Technol. Lett.*, vol. 3, pp. 784–786, 1991.

[5] R. Nagarajan, T. Fukushima, S. W. Corzine, and J. E. Bowers, "Effects of carrier transport on high-speed quantum well lasers," *Appl. Phys. Lett.*, vol. 59, pp. 1835–1837, 1991.

[6] S. Weiss, J. M. Wiesenfeld, D. S. Chemla, G. Raybon, G. Sucha, M. Wegener, G. Eisenstein, C. A. Burrus, A. G. Dentai, U. Koren, B. I. Miller, H. Temkin, R. A. Logan, and T. Tanbun-Ek, "Carrier capture times in 1.5 μm multiple quantum well optical amplifiers," *Appl. Phys. Lett.*, vol. 60, pp. 9–11, 1992.

[7] S. C. Kan, D. Vassilovski, T. C. Wu, and K. Y. Lau, "On the effects of carrier diffusion and quantum capture in high speed modulation of quantum well lasers," *Appl. Phys. Lett.*, vol. 61, pp. 752–754, 1992.

[8] N. Tessler and G. Eisenstein, "On carrier injection and gain dynamics in quantum well lasers," *IEEE J. Quantum Electron.*, vol. 29, pp. 1586–1595, 1993.

[9] C. Y. Tsai, C. Y. Tsai, Y. H. Lo, R. M. Spencer, and L. F. Eastman, "Nonlinear gain coefficients in semiconductor quantum-well lasers: effects of carrier diffusion, capture, and escape," *IEEE J. Selected Topics in Quantum Electron.*, vol. 1, pp. 316–330, 1995.

[10] J. Zhou, N. Park, K. J. Vahala, M. A. Newkirk, and B. I. Miller, "Study of interwell carrier transport by terahertz four-wave mixing in an optical amplifier with tensile and compressively strained quantum wells," *Appl. Phys. Lett.*, vol. 65, pp. 1897–1899, 1994.

[11] G. Lenz, E. P. Ippen, J. M. Wiesenfeld, M. A. Newkirk, and U. Koren, "Femtosecond dynamics of the nonlinear anisotropy in polarization insensitive semiconductor optical amplifiers," *Appl. Phys. Lett.*, vol. 68, 2933, (1996).

[12] R. Paiella, G. Hunziker, U. Koren, and K. J. Vahala, "Polarization-dependent optical nonlinearities of multiquantum-well laser amplifiers studied by four-wave mixing," *IEEE J. Select. Topics Quantum Electron.*, vol. 3, pp. 529–540, 1997.

[13] G. Hunziker, R. Paiella, K. J. Vahala, and U. Koren, "Measurement of the stimulated carrier lifetime in semiconductor optical amplifiers by four-wave mixing of polarized ASE noise," *IEEE Photon. Technol. Lett.*, vol. 9, pp. 907–909, 1997.

[14] M. A. Newkirk, B. I. Miller, U. Koren, M. G. Young, M. Chien, R. M. Jopson, and C. A. Burrus, "1.5 μm multiquantum-well semiconductor optical amplifier with tensile and compressively strained wells for polarization-independent gain," *IEEE Photon. Technol. Lett.*, vol. 4, pp. 406–408, 1993.

[15] B. Deveaud, J. Shah, T.C. Damen, and W.T. Tsang, "Capture of electrons and holes in quantum wells," *Appl. Phys. Lett.*, vol. 52, pp. 1886-1888, 1988.

[16] D. Marcenac, A. Kelly, D. Nesset, and D. Davis, "Bandwidth enhancement of wavelength conversion via cross-gain modulation by semiconductor optical amplifier cascade," *Electron. Lett.*, vol. 31, pp. 1442–1443, 1995.

[17] T. Durhuus, B. Mikkelsen, and C. Joergensen, "All-optical wavelength conversion by semiconductor optical amplifiers," *IEEE J. Lightwave Technol.*, vol. 14, pp. 942–954, 1996.

Chapter 5

FWM and Generation of TeraHertz Radiation in a Coupled Quantum-Well Structure

5.1 Introduction

In the previous chapter we showed that FWM can be effectively used to study carrier transport dynamics in MQW structures. In particular, we considered the case in which interwell transport is dominated by quantum capture/escape processes and classical diffusion across the barrier region. The results presented there indicate that these processes introduce qualitatively new features in the FWM frequency response, when this is measured under the appropriate conditions. In the following we will extend the same idea to a structure consisting of pairs of QWs coupled through resonant tunneling. This semiconductor double-well potential has received considerable

attention in recent years [1]–[5], both for fundamental investigations of the dynamics of quantum-mechanical wavepackets, and as a source of far-infrared radiation.

Here, we theoretically investigate the FWM frequency response of a SOA based on the alternating-strain coupled quantum well (ASCQW) structure schematically shown in Fig. 5.1. In particular, we propose a scheme for exciting in this structure coherent electric-dipole oscillations across the barrier, which, in turn, introduce a resonance peak in the FWM conversion efficiency at TeraHertz detuning rates [6], [7]. These results suggest a relatively simple way to experimentally study these oscillations, in the frequency domain; furthermore, they indicate the possibility of tailoring the (third-order) nonlinear optical susceptibility associated with FWM in SOAs by appropriate design of the active layer structure. Finally, we show how the same excitation scheme of this structure can in principle lead to efficient generation of far-infrared radiation through a concomitant second-order wave mixing process.

5.2 The Alternating-Strain Coupled Quantum-Well System

A coupled-well structure such as that shown in Fig. 5.1 consists of two QWs separated by a barrier thin enough to allow significant overlap of energetically close single-well states. The ground-state levels of the two wells in the conduction band ($|l\rangle$ and $|r\rangle$ for the left and right well respectively) can be aligned with each other (at some energy E_0) by proper design of the structure and application of a fine-tuning dc field along the growth direction, as illustrated in the right panel of Fig. 5.1. Then, as a result of state coupling across the heterostructure barrier, $|l\rangle$ and $|r\rangle$ mix to form

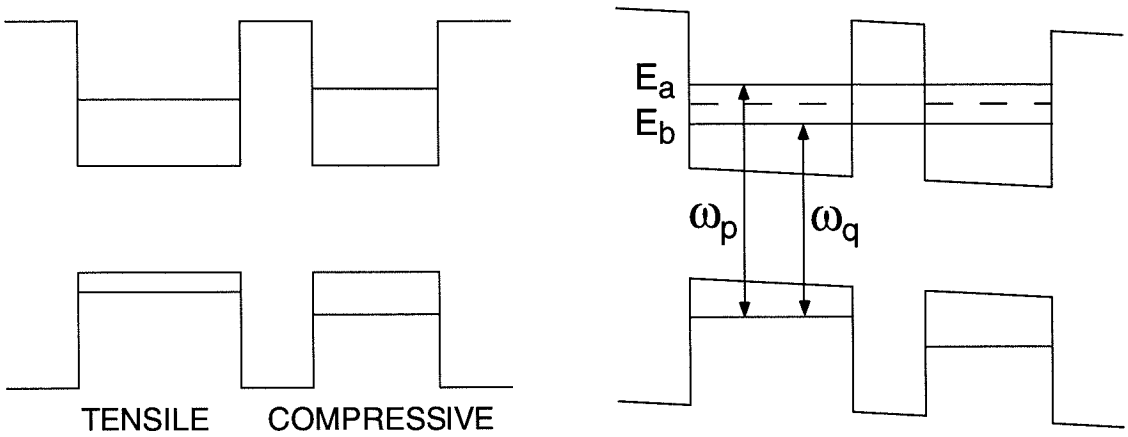

Figure 5.1: Schematic band diagram of the alternating-strain coupled quantum well structure. Under the bias condition shown in the right panel, the ground-state levels of the two QWs in the conduction band mix to form new delocalized eigenstates.

new stationary states that are delocalized over the two wells. At resonance, these are approximately given by the bonding and antibonding combinations

$$|b\rangle = \frac{1}{\sqrt{2}}\left(|l\rangle + |r\rangle\right) \qquad E_b = E_0 - \frac{\hbar\omega_t}{2}$$

$$|a\rangle = \frac{1}{\sqrt{2}}\left(|l\rangle - |r\rangle\right) \qquad E_b = E_0 + \frac{\hbar\omega_t}{2} \tag{5.1}$$

where ω_t is proportional to the coupling matrix element. On the other hand, for the polarity of the dc bias shown above, the valence band levels (both heavy and light holes) in the two wells are sufficiently separated in energy that the holes remain localized in either well.

Since the localized states $|l\rangle$ and $|r\rangle$ are no longer stationary under the bias condition of Fig. 5.1 (right panel), if an electron is initially prepared in either state, it will then tunnel back and forth through the heterostructure barrier at frequency ω_t.

The coupled-well structure can then be used to set up an electronic wavepacket oscillating across the barrier [1]–[4], provided one is able to initially excite a single-well wavepacket only. Note that this requires simultaneous excitation of both stationary states $|a\rangle$ and $|b\rangle$. This coherent wavepacket dynamics was demonstrated in a series of experiments on (Al)GaAs coupled-well structures [2], [3], where the required initial state was prepared by means of ultrashort laser pulses of spectral width larger than ω_t (so as to excite both stationary states) and center frequency tuned to that of the longer-wavelength single-well transition (so as to discriminate between the two wells).

The excitation of a single well can also be accomplished in a FWM experiment. In particular, we consider introducing strain of the opposite polarity in the two wells, and then appropriately selecting the polarization states of the input pump and probe waves. This technique is similar to the one described in the previous chapter to study capture/escape processes in alternating-strain MQW SOAs [8], [9]. For instance, if tensile strain is introduced in the left well and compressive strain in the right well, and the input field consists of two TM-polarized waves with frequencies as shown in Fig. 5.1, then, since compressive QWs have negligible TM gain, only the linear combination of $|a\rangle$ and $|b\rangle$ corresponding to the single-well state localized in the tensile well, $|l\rangle$, will be modulated by the beating of these input waves.

Under these conditions, the occupation probability of each single-well state behaves like a harmonic oscillator driven at the pump-probe detuning frequency. A resonance peak is therefore introduced in the FWM frequency response at a detuning frequency equal to the natural oscillation frequency ω_t (typically a few TeraHertz).

Furthermore, a steady-state electric dipole oscillation at the driving frequency is established across the conduction band barrier, which acts as a source of submillimeter waves. In the presence of dissipative interactions, such as carrier-carrier and carrier-phonon scattering, the phase-coherent nature of the wavepacket oscillatory dynamics is destroyed with a characteristic dephasing time constant τ_d. This limits the effectiveness of both processes, and in practice low temperature operation is required to observe a resonance enhancement in their respective efficiencies. However, the susceptibility responsible for the generation of far-infrared radiation is found to be significant, on the order of 10^{-7} m/V, even at room temperature.

5.3 Density-Matrix Treatment

In this section, we formulate and solve the dynamic equations describing the time evolution of the system density matrix. For the sake of simplicity, we will treat the case of only one subband in each well. Since we are considering the case of copolarized input waves with fixed polarization (i.e., linear along the growth axis), there is no need to include in this analysis the spin-degenerate states in each subband. Notice, however, that the incident optical field couples both the bonding and the antibonding conduction subbands with the valence subband of the left (tensile) well, $|v(\vec{k})\rangle$: as a result, we need to treat the ASCQW structure as a set of inhomogeneously broadened three-level systems (labeled by the two-dimensional wavevector $\vec{k}$ parallel to the junction plane). We find it convenient to write the density matrix ρ corresponding to each such system in the $\{|r\rangle, |l\rangle, |v\rangle\}$ representation, which amounts to replacing

the pair of stationary states $|a\rangle$ and $|b\rangle$ at any given $\vec{k}$ with their linear combinations given by Eq. 5.1.

Coupling among these basis states includes tunneling across the barrier in the conduction band, and the optically induced dipole interactions. Taking the origin of the growth axis at the center of the left well, and neglecting dipole moment matrix elements between single-well states in different wells (in view of their small overlap), the Hamiltonian of the system in this representation is then approximately given by

$$H = \begin{bmatrix} E_0(\vec{k}) - \mu_r(\vec{k})\mathcal{E}(t) & -\frac{1}{2}\hbar\omega_t & 0 \\ -\frac{1}{2}\hbar\omega_t & E_0(\vec{k}) & \mu_{lv}(\vec{k})\mathcal{E}(t) \\ 0 & \mu_{vl}(\vec{k})\mathcal{E}(t) & E_v(\vec{k}) \end{bmatrix} \tag{5.2}$$

where E_v is the eigenenergy of $|v\rangle$, μ is the electric dipole moment operator along the TM axis (which will be taken to be real-valued), and the explicit dependence on the in-plane wavevector $\vec{k}$ will be suppressed from here on. Notice that ω_t can be assumed to be independent of $\vec{k}$, as appropriate if the two-dimensional bands $|l\rangle$ and $|r\rangle$ have equal in-plane dispersion relations.

The main damping mechanism responsible for relaxation of the density matrix is provided by carrier-carrier and carrier-phonon scattering. The effects of these scattering processes are best formulated in the $\{|a\rangle, |b\rangle, |v\rangle\}$ representation, since they involve relaxation towards quasi-equilibrium Fermi distributions, which are properly defined only for the coupled-well energy eigenstates. In this basis the collisional

relaxation rate can be written as

$$R_{coll} = \begin{bmatrix} \frac{1}{\tau_1}(\rho_a - f_a) & \frac{1}{\tau_d}\rho_{ab} & \frac{1}{\tau_2}\rho_{av} \\ \frac{1}{\tau_d}\rho_{ba} & \frac{1}{\tau_1}(\rho_b - f_b) & \frac{1}{\tau_2}\rho_{bv} \\ \frac{1}{\tau_2}\rho_{va} & \frac{1}{\tau_2}\rho_{vb} & \frac{1}{\tau_1}(\rho_v - f_v) \end{bmatrix} \tag{5.3}$$

Here, the diagonal elements account for intraband scattering, which establishes a quasi-equilibrium Fermi distribution f_x in each subband ($x = a, b$, or v) with time constant τ_1 (assumed to be the same for all subbands). The off-diagonal term between $|a\rangle$ and $|b\rangle$ accounts for the loss of phase coherence of the tunneling oscillations, due to carrier-carrier and carrier-phonon scattering as well as interface roughness (in general the dephasing time constant τ_d is expected to be shorter than τ_1). Finally, the off-diagonal elements coupling $|v\rangle$ to either $|a\rangle$ or $|b\rangle$ describe the damping of the interband optical dipole oscillations. The matrix R_{coll} may be readily converted to the $\{|r\rangle, |l\rangle, |v\rangle\}$ representation using Eq. (5.1) and the definition of the density matrix.

Finally, we notice that the term proportional to μ_r in the Hamiltonian of Eq. (5.2) only introduces nonresonant contributions (at optical frequencies) to the density matrix time evolution. Neglecting these terms, we finally arrive at the following set of coupled equations

$$\dot{\rho}_v + \frac{\rho_v - f_v}{\tau_1} = -\frac{i}{\hbar}\mu_{lv}\mathcal{E}(t)\left(\rho_{vl} - \rho_{lv}\right) \tag{5.4}$$

$$\dot{\rho}_l + \frac{\rho_l + \rho_r - f_b - f_a}{2\tau_1} + \frac{\rho_l - \rho_r}{2\tau_d} = -\frac{i}{\hbar}\mu_{lv}\mathcal{E}(t)\left(\rho_{lv} - \rho_{vl}\right) - i\frac{\omega_t}{2}\left(\rho_{lr} - \rho_{rl}\right) \tag{5.5}$$

$$\dot{\rho}_r + \frac{\rho_r + \rho_l - f_b - f_a}{2\tau_1} + \frac{\rho_r - \rho_l}{2\tau_d} = -i\frac{\omega_t}{2}\left(\rho_{rl} - \rho_{lr}\right) \tag{5.6}$$

$$\dot{\rho}_{lv} + \left(i\omega_0 + \frac{1}{\tau_2}\right)\rho_{lv} = -\frac{i}{\hbar}\mu_{lv}\mathcal{E}(t)\left(\rho_l - \rho_v\right) + i\frac{\omega_t}{2}\rho_{rv} \tag{5.7}$$

$$\dot{\rho}_{rv} + \left(i\omega_0 + \frac{1}{\tau_2}\right)\rho_{rv} = -\frac{i}{\hbar}\mu_{lv}\mathcal{E}(t)\rho_{rl} + i\frac{\omega_t}{2}\rho_{lv} \tag{5.8}$$

$$\dot{\rho}_{rl} + \frac{\rho_{rl} + \rho_{lr} - f_b + f_a}{2\tau_1} + \frac{\rho_{rl} - \rho_{lr}}{2\tau_d} = -\frac{i}{\hbar}\mu_{lv}\mathcal{E}(t)\rho_{rv} - i\frac{\omega_t}{2}\left(\rho_r - \rho_l\right) \tag{5.9}$$

where ω_0 is the interband transition frequency in the left well in the absence of interwell coupling.

Under the experimental conditions considered here, the optical field input to the SOA induces in the active region a macroscopic polarization

$$\mathcal{P}(t) = P^{(\omega_p)}e^{-i\omega_p t} + P^{(\omega_q)}e^{-i\omega_q t} + P^{(\omega_s)}e^{-i\omega_s t} + P^{(\Omega)}e^{-i\Omega t} + c.c. \tag{5.10}$$

which can be expressed as

$$\mathcal{P}(t) = \frac{1}{V}\sum_{\vec{k}} \mu_{lv}\left(\rho_{lv} + \rho_{vl}\right) + \mu_r\rho_r \tag{5.11}$$

where V is the volume of the active region, and the summation may be replaced by an integral over the appropriate density of states. In Eq. (5.10) ω_p, ω_q, and ω_s are, as usual, the frequencies of the pump, probe and converted signal respectively, and $\Omega = \omega_p - \omega_q = \omega_s - \omega_p$ is the detuning frequency. Microscopic expressions for all the harmonic components of the polarization density can then be immediately derived given ρ_{lv} and ρ_r.

The set of equations (5.4)-(5.9) can be solved using a procedure similar to that outlined in chapter 3 (where we solved the density-matrix dynamic equations for FWM in a bulk or uncoupled-well SOA). While the approach is essentially the same, the algebra is more involved here since three mutually coupled energy levels are involved

(in particular, following Ref. [1], it is convenient to introduce a vector representation for the reduced density matrix $\{\rho_l, \rho_r, \rho_{lr}\}$, and then transform the corresponding equations of motion to a reference frame rotating about the "z-axis" with radian frequency ω_t). The details of the calculation can be found in Ref. [7], together with the resulting expressions for all the relevant elements of the density matrix. In the following, we will use these results to solve for the nonlinear susceptibilities associated with generation of the FWM signal (section 5.4) and of a TeraHertz wave at the detuning frequency (section 5.5).

5.4 FWM Conversion Efficiency

In order to compute the FWM conversion efficiency of the ASCQW structure, we need to evaluate the harmonic component of the polarization density at ω_s, which provides the source of the FWM signal. This can be cast in the form [7]

$$P^{(\omega_s)} = -\frac{i}{V}\sum_{\vec{k}} \frac{\mu_{lv}^2}{\hbar}\tilde{\chi}'(\omega_s)\Big\{ \left(\rho_l^{(0)} - \rho_v^{(0)})\right) E^{(\omega_s)} + \left(\rho_l^{(\Omega)} - \rho_v^{(\Omega)})\right) E^{(\omega_p)} + \\ + i\frac{\omega_t\tilde{\chi}(\omega_s)}{2}\left(\rho_{rl}^{(0)}E^{(\omega_s)} + \rho_{rl}^{(\Omega)}E^{(\omega_p)}\right)\Big\} \tag{5.12}$$

where we defined

$$\tilde{\chi}(\omega) = \frac{\tau_2}{1 - i\tau_2(\omega - \omega_0)}, \qquad \tilde{\chi}'(\omega) = \frac{\tilde{\chi}(\omega)}{1 + (\frac{\omega_t\tilde{\chi}(\omega)}{2})^2}. \tag{5.13}$$

In the case under consideration, $P^{(\omega_s)}$ has the general form [10] $P^{(\omega_s)} = \chi_L E^{(\omega_s)} + \chi_{FWM}(E^{(\omega_p)})^2(E^{(\omega_q)})^*$, where the second term is responsible for FWM, and in general has contributions from carrier density modulation, carrier heating and spectral hole burning.

At detuning frequencies on the order of ω_t (i.e., of a few TeraHertz), spectral hole burning is expected to be the dominant FWM process [11]. Therefore, in this detuning frequency range, χ_{FWM} is well approximated by the spectral hole burning contribution; from the analysis outlined in the previous section, this is found to be given by [7]

$$\chi_{SHB} = \frac{i}{V}\sum_{\vec{k}} \frac{\mu_{lv}^4}{\hbar^3}\Delta f\ \tilde{\chi}'(\omega_s)\left\{\frac{3}{2}\frac{\tau_1}{1-i\Omega\tau_1}L_1(\Omega;\omega_t)+\right.$$
$$+\frac{1}{4}\frac{\tau_d}{1-i(\Omega+\omega_t)\tau_d}\left(1+i\frac{\omega_t\tilde{\chi}(\omega_s)}{2}\right)L_2(\Omega;\omega_t)+$$
$$\left.+\frac{1}{4}\frac{\tau_d}{1-i(\Omega-\omega_t)\tau_d}\left(1-i\frac{\omega_t\tilde{\chi}(\omega_s)}{2}\right)L_2(\Omega;-\omega_t)\right\} \tag{5.14}$$

where the Fermi inversion factor is $\Delta f = (f_b+f_a)/2-f_v$, and furthermore we defined the lineshape functions

$$L_1(\Omega;\omega_t) = \tilde{\chi}'(\omega_p)+\tilde{\chi}'(\omega_q)^* - \frac{\omega_t^2}{4}\tilde{\chi}(\omega_s)\left(\tilde{\chi}'(\omega_p)\tilde{\chi}(\omega_p)-\tilde{\chi}'(\omega_q)^*\tilde{\chi}(\omega_q)^*\right) \tag{5.15}$$

$$L_2(\Omega;\omega_t) = \tilde{\chi}'(\omega_p)+\tilde{\chi}'(\omega_q)^* + i\frac{\omega_t}{2}\left(\tilde{\chi}'(\omega_p)\tilde{\chi}(\omega_p)-\tilde{\chi}'(\omega_q)^*\tilde{\chi}(\omega_q)^*\right) \tag{5.16}$$

The expression for χ_{SHB} in Eq. (5.14) reduces to that of a bulk or uncoupled-well amplifier (given in Appendix A) as ω_t approaches zero (and $\tau_d = \tau_1$). In the presence of interwell coupling, however, two effects contribute to significantly enhance the magnitude of χ_{SHB} near ω_t. First, consistent with the interpretation of the spectral hole producing the gratings as a harmonic oscillator driven at its natural frequency, a resonance is introduced at ω_t for both positive and negative detuning frequencies, as indicated by the complex Lorentzians in the second and third terms in curly brackets respectively. Furthermore, the overall lineshape of the third-order transitions leading

to generation of the FWM signal photons, given by L_2 in Eq. 5.16, is also affected by the interwell coupling in a way so as to enhance such transitions.

For a numerical estimate, we consider an ASCQW optical amplifier based on the InGaAsP material system and consisting of pairs of 40-Å compressive wells and 160-Å tensile wells separated by a 20-Å barrier, with carrier density $N = 2.3 \times 10^{24}$ m^{-3}. We assumed alloy compositions appropriate to operation at 1.55 μm. The interband dipole moment of the tensile well (the one providing gain in this context) was estimated to be $\mu_{lv} = q \times 11.5$ Å, giving a peak material gain coefficient of approximately 5,800 cm^{-1} at room temperature. The energy separation between the valence subband edges in the two wells (under zero bias condition) was found to be on the order of 20 meV at $\vec{k} = 0$ (and larger at finite $\vec{k}$ due to the different dispersion in the two oppositely strained wells), which amply justifies neglect of hole interwell coupling. Finally, we took $\omega_t = 4$ THz.

The magnitude squared of $\chi_{SHB}(\Omega)$ at TeraHertz detuning frequencies is plotted in Fig. 5.2, where χ_{SHB} is evaluated in MKS units and plotted in decibels for convenience. The relaxation time constants τ_1, τ_2, and τ_d were taken equal to 1 psec, as appropriate to a temperature of about 30 degrees Kelvin and operation near the Fermi edge [12]. For comparison, $|\chi_{SHB}|^2$ in the limit of no coupling between the wells is also shown (dashed line). A pronounced peak, preceded by a dip, is clearly introduced at the resonance frequency, giving rise to a maximum increase in conversion efficiency of approximately two orders of magnitude at $\Omega = \omega_t$. The asymmetry between the peak and the dip is due to the Ω dependence of the lineshape function

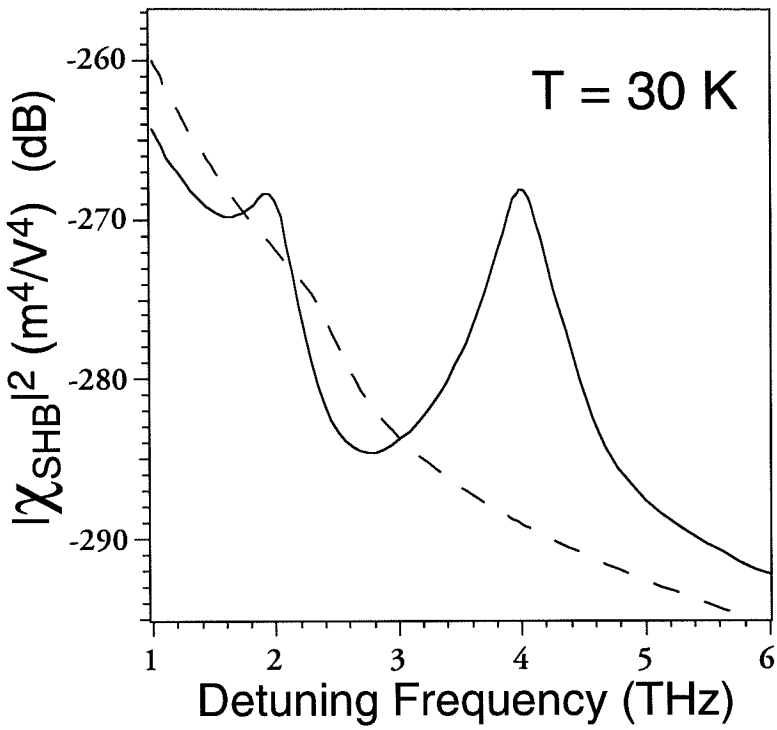

Figure 5.2: Spectral hole burning contribution to the FWM conversion efficiency of the ASCQW structure (continuous line) and of an otherwise identical uncoupled-well SOA (dashed line) versus detuning frequency, for $\tau_1 = \tau_2 = \tau_d = 1$ psec and $\omega_t = 4$ THz.

of Eq. (5.16). Note that at detuning frequencies well below ω_t, $|\chi_{SHB}|^2$ is smaller in the ASCQW structure than in the uncoupled case by approximately 4 dB; this is attributed to the reduction of the (time-average) amplitude of the "spectral hole" by the oscillations across the barrier.

The size of the resonance peak is obviously limited by the damping rate $1/\tau_d$. This is illustrated in Fig. 5.3, where the ratio of $|\chi_{SHB}|^2$ to its value in the uncoupled case ($|\chi_{SHB}^{UNC}|^2$) is plotted for different values of τ_d. As shown in this figure, the effect of the interwell coupling should be detectable for τ_d as small as a few hundred femtoseconds,

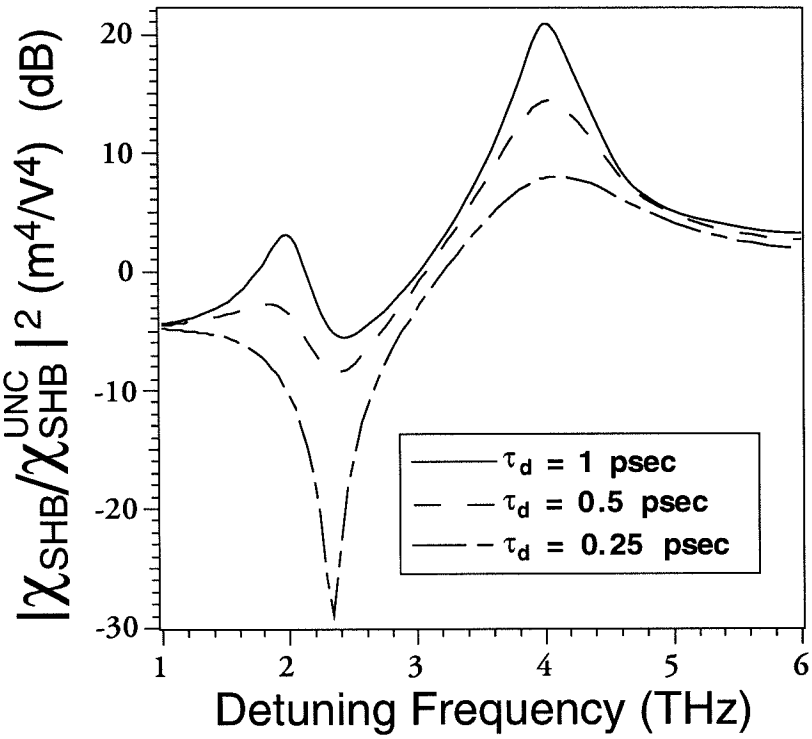

Figure 5.3: Enhancement in the FWM conversion efficiency of the ASCQW structure versus detuning frequency, for $\omega_t = 4$ THz and $\tau_1 = \tau_2 = \tau_d = 1, 0.5, 0.25$ psec, corresponding to an estimated temperature of 30, 60, and 90 K, respectively [12].

indicating that higher temperature operation may be possible.

5.5 Generation of TeraHertz Radiation

The TeraHertz spectral region (1-10 THz) still awaits the development of convenient sources of coherent narrowband radiation, which may be quite useful for applications such as local oscillator sources in high-resolution laser heterodyne spectrometers. In the past few years, several schemes have been proposed [1], [13]–[15] followed by promising experimental demonstrations [3], [5], [16]–[17]. In this section, we consider

the generation of TeraHertz radiation by the steady-state electronic wavepacket oscillations across the conduction-band barrier in the present configuration. The results suggest a novel scheme for the generation of far-infrared radiation, based on wave mixing in the ASCQW structure.

The harmonic component of the polarization density at Ω is given by [7]

$$P^{(\Omega)} = \frac{1}{V}\sum_{\vec{k}} \mu_r \rho_r^{(\Omega)} \tag{5.17}$$

and can be immediately evaluated from the analysis outlined in section 5.3. The corresponding (second order) susceptibility χ_{TH}, defined so that $P^{(\Omega)} = \chi_{TH} E^{(\omega_p)} (E^{(\omega_q)})^*$, is found to be given by [7]

$$\chi_{TH} = -\frac{1}{V}\sum_{\vec{k}} \frac{\mu_r \mu_{lv}^2}{\hbar^2} \Delta f \left\{ \frac{1}{2} \frac{\tau_1}{1 - i\Omega\tau_1} \left[\tilde{\chi}'(\omega_p) + \tilde{\chi}'(\omega_q)^* \right] + \right.$$

$$\left. -\frac{1}{4} \frac{\tau_d}{1 - i(\Omega + \omega_t)\tau_d} L_2(\Omega; \omega_t) - \frac{1}{4} \frac{\tau_d}{1 - i(\Omega - \omega_t)\tau_d} L_2(\Omega; -\omega_t) \right\} \tag{5.18}$$

where L_2 is defined in Eq. (5.16).

The magnitude of χ_{TH} is plotted in Fig. 5.4a versus detuning frequency, for $\mu_r = q \times 110$ Å , and assuming T = 30 K as in the previous section. Again consistent with the harmonic oscillator picture, there appears a peak about the resonance frequency ω_t (4 THz), where $|\chi_{TH}| = 5 \times 10^{-6}$ m/V, with lineshape determined by the dephasing time constant τ_d. In Fig. 5.4b, $|\chi_{TH}(\Omega)|$ is plotted under room temperature conditions, for which we took $\tau_1 = \tau_2 = \tau_d = 50$ fsec. The peak at resonance is now completely smeared out due to the ultrafast dephasing of the tunneling oscillations. However, the continuous excitation of such oscillations enabled by our proposed scheme still provides a large $|\chi_{TH}(\Omega)|$, on the order of 10^{-7} m/V for Ω up to about

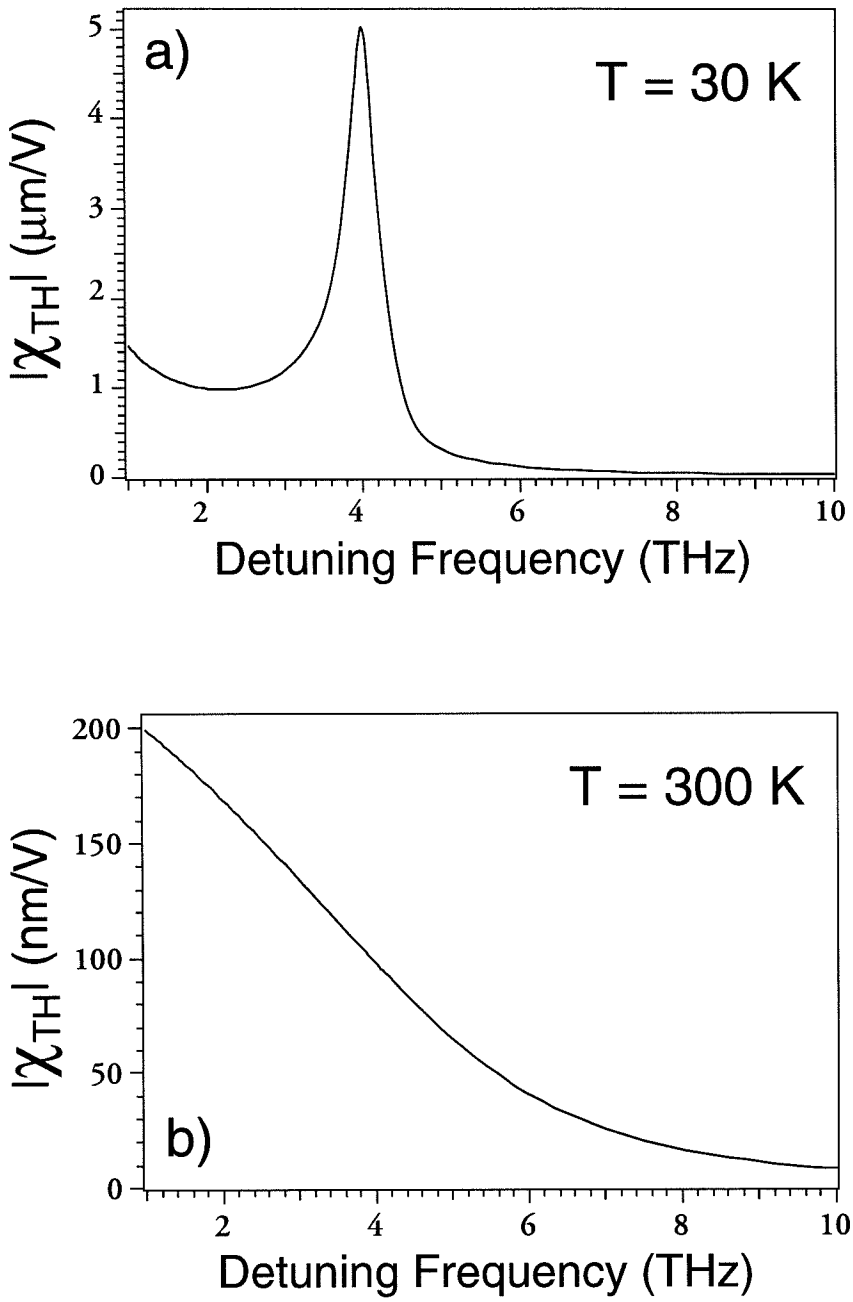

Figure 5.4: Magnitude of the second-order susceptibility associated with generation of TeraHertz radiation in the ASCQW structure versus detuning frequency, for T = 30 K (a) and 300 K (b).

4 THz.

In conclusion we point out that, while both the wavelength converted signal and the TeraHertz signal are simultaneously generated in the ASCQW structure by the nonlinear interactions considered here, optimization of one effect (through design considerations involving the waveguide structure, operating wavelength, pumping level, etc.) may be accompanied by a reduction of the other. In particular, for efficient generation of far-infrared radiation at the output of the device, one has to deal with phase-matching considerations and with the strong absorption at TeraHertz frequencies due to plasma heating (phase-matching is much less of a problem in the case of FWM, as discussed in section 7.2).

The phase mismatch between the input waves and the generated TeraHertz signal may be minimized using (quasi)phase-matching techniques [18], [19]. Also, one may try to take advantage of the acoustic-phonon contribution to the dielectric response at TeraHertz frequencies. Because of the variation of such contribution with both frequency and wavevector, one may envision a generation scheme in which pump, probe, and TeraHertz wave propagate along different directions (parallel to the heterojunction plane) for which the phase-matching conditon is satisfied. Similarly, as suggested by recent work [13], [15], [17] free-carrier absorption may be minimized by appropriate design of the overall device structure. The scheme for generation of far infrared radiation described above seems then very promising in view of the large nonlinearity involved. In fact, in the work of Ref. [17], the authors report extremely efficient generation of 2.5 THz radiation from difference frequency mixing in (Al)GaAs

MQW waveguides associated with an estimated $\chi^{(2)}$ comparable to the value for χ_{TH} computed here. It would then be quite interesting to consider the design and practical implementation of a parametric oscillator based on wave mixing in the ASCQW structure.

Bibliography

[1] S. Luryi, "Polarization oscillations in coupled quantum wells–A scheme for the generation of submillimeter electromagnetic waves," *IEEE J. Quantum Electron.*, vol. 27, pp. 54–60, 1991.

[2] K. Leo, J. Shah, E. O. Gobel, T. C. Damen, S. Schmitt-Rink, W. Schafer, and K. Kohler, "Coherent oscillations of a wave packet in a semiconductor double-quantum-well structure," *Phys. Rev. Lett.*, vol. 66, pp. 201–204, 1991.

[3] H. G. Roskos, M. C. Nuss, J. Shah, K. Leo, D. A. B. Miller, A. M. Fox, S. Schmitt-Rink, and K. Kohler, "Coherent submillimeter-wave emission from charge oscillations in a double-well potential," *Phys. Rev. Lett.*, vol. 68, pp. 2216–2219, 1992.

[4] K. Leo, J. Shah, T. C. Damen, A. Schulze, T. Meier, S. Schmitt-Rink, P. Thomas, E. O. Gobel, S. L. Chuang, M. S. C. Luo, W. Schafer, K. Kohler, and P. Ganser, "Dissipative dynamics of an electronic wavepacket in a semiconductor double well potential," *IEEE J. Quantum Electron.*, vol. 28, pp. 2498–2507, 1991.

[5] C. Sirtori, F. Capasso, J. Faist, L. N. Pfeiffer, and K. W. West, "Far-infrared generation by doubly resonant difference frequency mixing in a coupled quantum-well two-dimensional electron gas system," *Appl. Phys. Lett.*, vol. 65, pp. 445–447, 1994.

[6] R. Paiella and K. J. Vahala, "Highly nondegenerate four-wave mixing efficiency of an asymmetric coupled quantum-well structure," *Appl. Phys. Lett.*, vol. 66, pp. 2619–2621, 1995.

[7] R. Paiella and K. J. Vahala, "Four-wave mixing and generation of TeraHertz radiation in an alternating-strain coupled quantum-well structure," *IEEE J. Quantum Electron.*, vol. 32, pp. 721–728, 1996.

[8] J. Zhou, N. Park, K. J. Vahala, M. A. Newkirk, and B. I. Miller, "Study of interwell carrier transport by terahertz four-wave mixing in an optical amplifier with tensile and compressively strained quantum wells," *Appl. Phys. Lett.*, vol. 65, pp. 1897–1899, 1994.

[9] R. Paiella, G. Hunziker, K. J. Vahala, and U. Koren, "Measurement of the interwell carrier transport lifetime in multiquantum-well optical amplifiers by polarization-resolved four-wave mixing," *Appl. Phys. Lett.*, vol. 69, pp. 4142-4144, 1996.

[10] A. Uskov, J. Mϕrk, and J. Mark, "Wave mixing in semiconductor laser amplifiers due to carrier heating and spectral hole burning," *IEEE J. Quantum Electron.*, vol. 30, pp. 1769–1781, 1994.

[11] J. Zhou, N. Park, J. W. Dawson, K. J. Vahala, M. A. Newkirk, and B. I. Miller, "Terahertz four-wave mixing spectroscopy for study of ultrafast dynamics in a semiconductor optical amplifier," *Appl. Phys. Lett.*, vol.63, pp. 1179 – 1181, 1993.

[12] K. Meissner, B. Fluegel, H. Gieben, G. Mohs, R. Binder, S. W. Koch, and N. Peyghambarian, "Carrier dephasing in the gain region of an inverted semiconductor," *Phys. Rev. B*, vol. 50, pp. 17647–17650, 1994.

[13] J. Khurgin, "Second-order intersubband nonlinear-optical susceptibilities of asymmetric quantum-well structures," *J. Opt. Soc. Am. B*, vol. 6, pp. 1673–1682, 1989.

[14] M. Helm, in *Intersubband Transitions in Quantum Wells*, E. Rosencher, B. Vinter, and B. Levine, Eds. Plenum: New York, 1992, p. 151.

[15] A. N. Korotkov, D. V. Averin, and K. K. Likharev, "TASERs: possible dc pumped terahertz lasers using interwell transitions in semiconductor heterostructures," *Appl. Phys. Lett.*, vol. 65, pp. 1865-1867, 1994.

[16] E. R. Brown, K. A. Mcintosh, K. B. Nichols, and C. L. Dennis, "Photomixing up to 3.8 THz in low-temperature-grown GaAs," *Appl. Phys. Lett.*, vol. 66, pp. 285-287, 1995.

[17] B. N. Saif, B. D. Seery, J. Khurgin, and C. Wood, "Generation of 2.5 terahertz radiation by difference frequency mixing in GaAs/GaAlAs multiple quantum-well waveguides," *QELS*, paper QThA6, 1995.

[18] G. Almogy, M. Segev, and A. Yariv, "Intersubband-transition-induced phase-matching," *Optics Lett.*, vol. 19, pp. 1192-1194, 1994.

[19] I. Vurgaftman, J. R. Meyer, L. R. Rammohan, "Optimized second-harmonic generation in asymmetric double-quantum wells," *IEEE J. Quantum Electron.*, vol. 32, pp. 1334–1346, 1996.

Chapter 6

FWM Mediated by Quantum-Well Carrier Capture

6.1 Introduction

The electrical carriers injected to the barrier region of a semiconductor QW structure are captured in the QW bound states with a finite characteristic rate, the inverse capture lifetime $1/\tau_{cap}$. Such capture processes (effectively intersubband transitions between 3D states delocalized across the barrier region and quantum-confined 2D states in the QW) have attracted considerable attention in recent years [1]–[8], within the broad context of ultrafast spectroscopy of semiconductor microstructures [1]. Furthermore, they are of significant interest to the semiconductor laser community, because of their direct relevance to the dynamic and spectral features of QW lasers [5]–[8]. It is generally agreed that the capture of electrons and holes in polar semiconductors mainly occurs through the emission of optical phonons, although carrier-carrier scat-

tering also plays a role [8] in the presence of the large carrier densities typical of laser operation. In any case, the direct measurement of the "intrinsic" capture lifetime is complicated, because experiments typically measure a compound response including, e.g., drift and diffusion across the barrier region, or energy relaxation within the 3D continuum and within the 2D subbands.

In chapter 4, we described a FWM experiment aimed at studying interwell transport dynamics in MQW SOAs [9]. From the results of this measurement, and through a somewhat involved numerical fit, we inferred an estimate of 1.5 psec for τ_{cap}. In this chapter, we present a different experimental technique [10], based on wavelength-resolved FWM, to directly study capture processes in QW active layers. In the experiment, a small-signal carrier density modulation is generated in the electronic states near the barrier band edges (by photomixing of two nondegenerate pump waves), and is then probed in the QWs as a function of the modulation frequency. As we will discuss in the next section, this technique allows to directly infer the capture lifetime from the data, with no need for involved numerical fits (provided that the impact of wave propagation effects on the data is minimized). Finally, in section 6.3 we present a full microscopic theory of phonon-assisted QW capture: in particular, the rate equations used to interpret the wavelength-resolved FWM results are rigorously derived (including microscopic expressions for the relevant time constants), and the possible impact of hot-phonon effects [11]–[15] on the capture process is discussed.

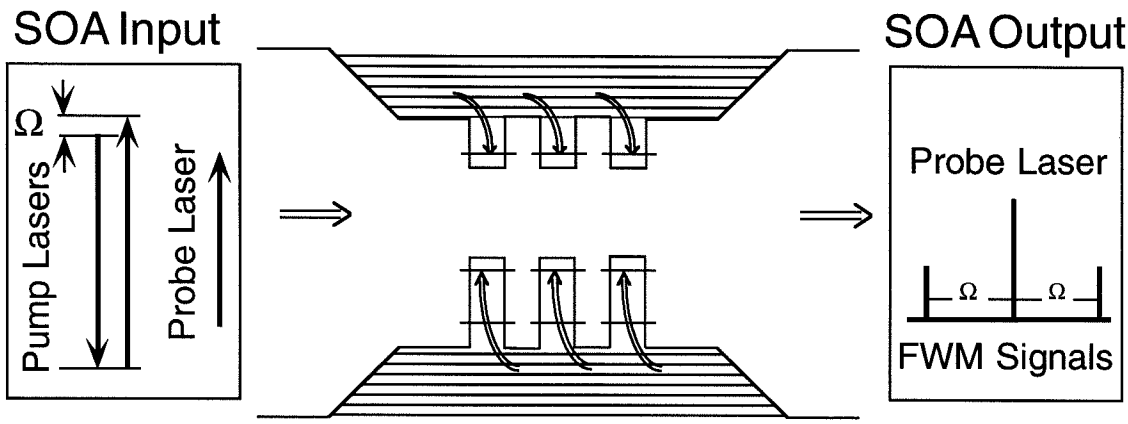

Figure 6.1: Schematics of the capture lifetime measurement. In this experiment, a carrier density modulation is generated in the barrier region through beating of two 1.3 μm pump waves. A fraction of this modulation is captured into the QW bound states, where it then partially scatters a 1.5 μm probe wave into two FWM sidebands.

6.2 Measurement of the Capture Lifetime

A pictorial description of the experimental configuration is given in Fig. 6.1. The structure studied is a MQW InGaAs/InGaAsP SOA consisting of three pairs of tensile and compressively strained QWs [16] (the same device used in the measurements of the previous chapters; notice, however, that the presence of strain is not essential to this experiment). Three cw waves, generated by temperature-tunable DFB lasers, are coupled into the SOA waveguide: two pump waves with frequencies matching the bandgap of the InGaAsP barriers (in the 1.3 μm band), and one probe wave with frequency near the gain peak of the SOA (in the 1.5 μm band).

The beating of the two pump waves generates a modulation of the carrier density in the barrier region, at their difference frequency Ω. A fraction of this modulation

is captured into the QWs where it then acts to scatter energy from the probe laser beam into two FWM sidebands. Information on the carrier capture process can then be inferred from the relative intensity of either FWM signal as a function of the modulation frequency Ω. In particular, we expect the FWM conversion efficiency to become negligibly small at modulation frequencies much larger than the capture rate (at these frequencies, the probability of the modulated carrier distribution being captured into the QWs within a few modulation periods becomes negligibly small).

It is important to emphasize that the photon energy of the pump waves (approximately 0.94 eV) is very close to (actually slightly lower than) the barriers bandgap energy (nominally 0.97 eV): accounting for thermal broadening, we conclude that the electronic states directly modulated by these waves are not bound in any QW (i.e., they are purely 3D states), although their wavefunctions are somewhat localized near the wells. As a result, in this experiment the limiting rate is most likely that of the intrinsic, "quantum" capture (fully isolated from all other transport effects), which is expected to be a relatively fast process, on the order of about one picosecond (see for instance chapter 4).

The use of photomixing to generate the carrier density modulation, and of a optical heterodyne system to detect the modulation sidebands on the probe wave, allows us to extend the measured bandwidth to a few hundreds of GigaHertz, i.e., well beyond such intrinsic capture rate, which can then be measured directly. Incidentally, a similar technique has been used to study capture in a QW laser in Ref. [7], where the carrier density modulation was produced by injection of a directly modulated beam

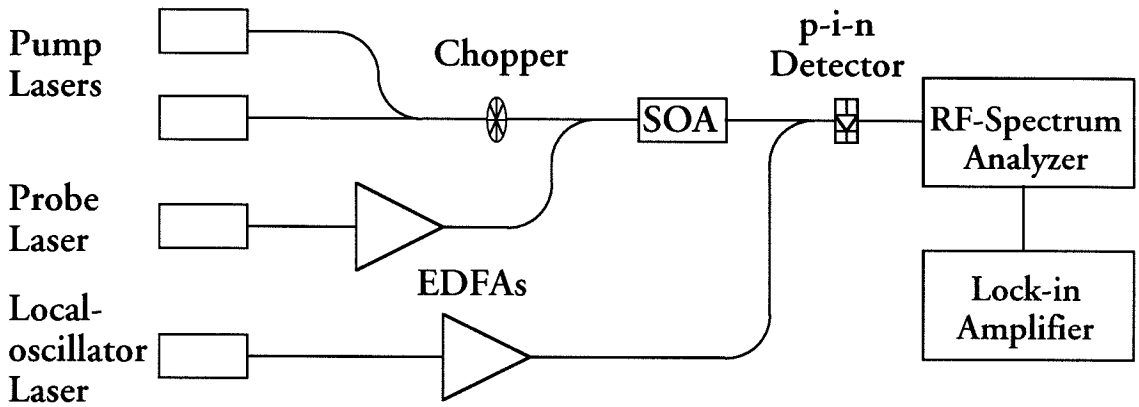

Figure 6.2: Experimental setup for the capture lifetime measurement.

from another semiconductor laser; in that work, however, the modulation frequency was limited by the bandwidth of the laser source and the detection electronics to around 20 GHz, so that the intrinsic capture could not be directly isolated from the other transport processes.

The physical layout of the experiment is shown in Fig. 6.2. Approximately 2 mW of pump power and 17 mW of probe power (after preamplification in a high-gain EDFA) were coupled into the SOA (780 μm long, biased with a dc current of 100 mA). The probe wave was linearly polarized along the TM axis of the SOA waveguide, so that only the tensile wells are probed (compressively strained QWs have negligible gain for TM light); this avoids any complication arising from possibly having different capture rates in the two types of wells. The SOA output was combined with a tunable optical local oscillator, and the beat signal between the local oscillator and either FWM sideband was detected at a constant frequency in a radio-frequency spectrum analyzer. In order to increase the signal-to-noise ratio, we fed the analog output of

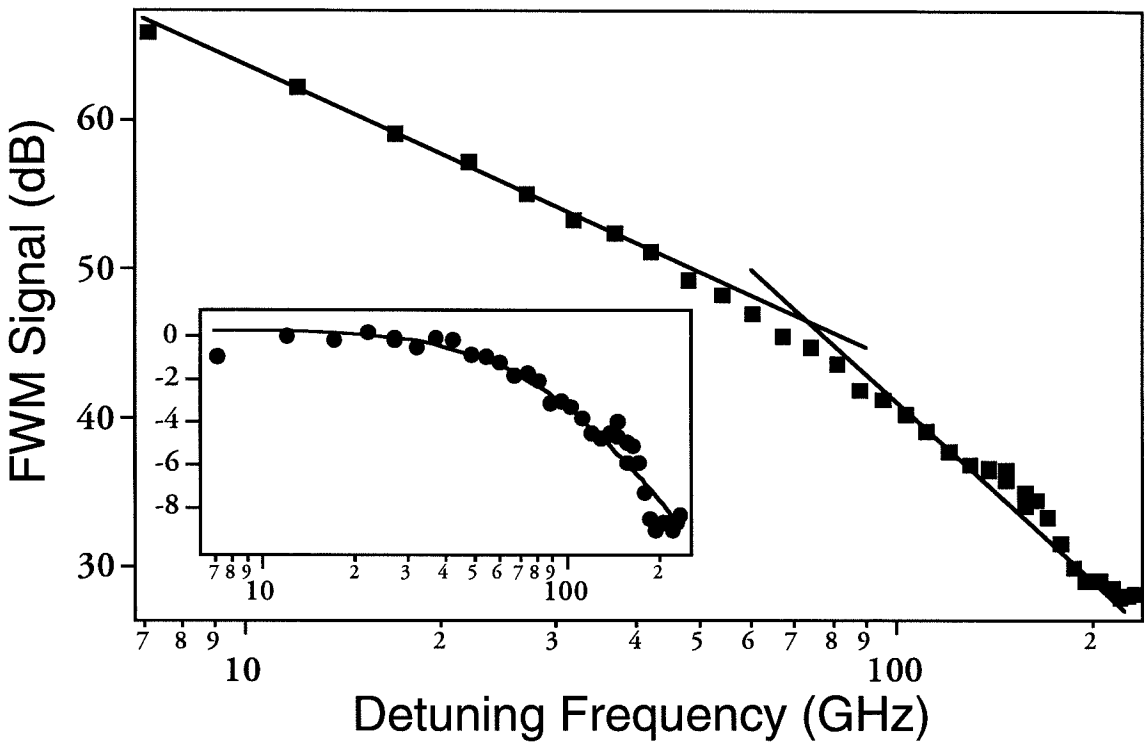

Figure 6.3: Measured FWM signal power versus modulation frequency (the origin of the vertical axis is arbitrary). As emphasized by the continuous lines, the slope of the data changes from -20 to -40 dB/dec with increasing detuning frequency. The inset displays the same data with the initial 20 dB/dec roll-off subtracted out; the continuous curve is a single-pole frequency response with pole at 88 GHz = $1/(2\pi \times 1.8$ psec).

the spectrum analyzer to a lock-in amplifier (locked to a chopper placed in the optical path of the pump waves), where the signal was measured.

A typical trace is shown in Fig. 6.3, which gives to the frequency-upconverted FWM sideband with the modulation frequency ranging from 7 to 230 GHz. As emphasized by the continuous lines, the data exhibit a 20 dB/dec roll-off at low modulation frequencies and a 40 dB/dec roll-off at modulation frequencies exceeding

about 90 GHz. The former roll-off is associated with the interband stimulated recombination of the carriers in the QWs (occurring at a rate $1/(2\pi\tau_s)$ of approximately 1.2 GHz under the present experimental condition [17]). Since the emphasis here is on the features related to the capture process, this initial roll-off was normalized out (notice that the exact value of $1/(2\pi\tau_s)$ used in this normalization is irrelevant, provided it is smaller than the smallest modulation frequency measured). The result is shown in the inset of Fig. 6.3, which clearly suggests the presence of another pole at 88 GHz (corresponding to a lifetime of 1.8 psec). Additional structures are observed at larger modulation frequencies. The same features were observed in the frequency-downconverted data.

A two-pole frequency response is consistent with a model of the capture dynamics based on the following set of rate equations (in the frequency domain)

$$\begin{aligned} -i\Omega N_{2D}^{(\Omega)} &= -\left(\frac{1}{\tau_s}+\frac{1}{\tau_{esc}}\right)N_{2D}^{(\Omega)}+\frac{N_{3D}^{(\Omega)}}{\tau_{cap}}, \\ -i\Omega N_{3D}^{(\Omega)} &= -\left(\frac{1}{\tau_s}+\frac{1}{\tau_{cap}}\right)N_{3D}^{(\Omega)}+\frac{N_{2D}^{(\Omega)}}{\tau_{esc}}+g_{3D}^{(\Omega)}. \end{aligned} \tag{6.1}$$

Here $N_{2D}^{(\Omega)}$ denote the small-signal density of carriers confined inside each (tensile) well; $N_{3D}^{(\Omega)}$ is the density of unbound carriers localized near the same QW (and directly modulated by the beating of the pump waves, at a rate $g_{3D}^{(\Omega)}$); and τ_{cap} and τ_{esc} are the intrinsic capture and escape lifetimes. In the next section we present a rigorous derivation of these equations (including microscopic expressions for the capture and escape lifetimes), and we discuss in detail their range of validity. At this stage we simply point out that we are not including in this model any effect related to transport in real space, such as diffusion or drift, as appropriate for excitation near

the barriers' band edges. Furthermore, we do not explicitly consider the capture of both electrons and holes, since the frequency response measured in this experiment should be dominated by the slower carrier type (presumably the electrons [3]).

As it follows from the analysis of chapter 2, the field amplitude of the FWM signal (carrier density modulation contribution) as a function of Ω is proportional to the amplitude of the carrier density modulation that generates it, $N_{2D}^{(\Omega)}$. Solving the coupled set of equations (6.1), one finds

$$N_{2D}^{(\Omega)} = \frac{1/\tau_{cap}}{(-i\Omega + 1/\tau_s)(-i\Omega + 1/\tau_{cap} + 1/\tau_{esc} + 1/\tau_s)} g_{3D}^{(\Omega)}, \tag{6.2}$$

so that on the basis of this simple model we expect the FWM conversion efficiency to exhibit one pole at $1/\tau_s$ and another at $1/\tau_{cap} + 1/\tau_{esc} + 1/\tau_s$ ($\approx 1/\tau_{cap}$ since in general the capture lifetime is shorter than both the stimulated recombination and the escape lifetimes [6], [9]). As a result, τ_{cap} can be directly read off the experimental data, provided that their frequency dependence is entirely ascribed to the carrier density modulation response described by Eq. (6.2). If we assume that this is indeed the case for the data of Fig. 6.3, we immediately obtain an electronic capture lifetime of 1.8 psec. Incidentally, this estimate is consistent with the results of the experiment [9] described in chapter 4, from which a value of 1.5 psec for τ_{cap} in the same SOA (and 8 psec for τ_{esc}) was inferred.

However, it is obvious from Fig. 6.3 that the two-pole frequency response of Eq. (6.2) is inadequate to fit the data at the higher measured modulation frequencies. In particular, notice the two shoulders in the data around 140 and 200 GHz, which resemble the first two nulls of a phase-matching frequency response. Due to the large

frequency difference between the pump waves on the one hand, and the probe and FWM signal on the other, the wavenumber mismatch Δk entering the FWM conversion efficiency may be large enough to produce zeroes at these detuning frequencies. However, the observed pronounced features can be fit to a damped phase-matching frequency response only if the damping (i.e., the total absorption of the pump waves in the SOA) is smaller than approximately 10 dB, whereas a loss of more than 20 dB was actually measured. Alternative explanations for the high-frequency features of the data of Fig. 6.3 are under consideration. In order to resolve this issue, further experimental work is required, in particular, to test for the presence of phase-matching. This could be accomplished by using pump waves of shorter wavelength or SOA active layers having lower QW barrier energies, so as to increase pump absorption and hence decrease the effective interaction length (these measurements are planned for the near future in our labs).

The ambiguities just discussed regarding the role of phase-matching prevent us from making a definite statement on the magnitude of τ_{cap}. In particular, if the high-frequency features in the data are due to phase-matching effects, these same effects could be responsible for most of the roll-off observed in the normalized data (inset of Fig. 6.3). Then the above mentioned estimate of $1/(1.8$ psec) should be regarded as an upper limit to the capture rate under the present experimental conditions. Furthermore, at the larger measured modulation frequencies, the temperature dynamics of the captured carrier distributions may also affect the frequency response. In any case, the results presented here clearly indicate how the proposed technique can be

used to measure the strength of the carrier density modulation captured in the well, up to modulation frequencies larger than the expected capture rate. This feature makes the technique particularly attractive, because (provided that phase-matching can be eliminated as a source of frequency dependence) the capture lifetime can be directly read off the data, after the simple normalization carried out in the inset of Fig. 6.3.

6.3 Microscopic Theory of Phonon-Assisted Capture

In this section, we present a detailed microscopic theory of phonon-assisted capture and escape processes in QWs. Our goal is to derive an analytic expression for the capture efficiency (as measured in a FWM experiment, i.e., in the frequency domain), and to underline the approximations involved in the rate equation model used above. This procedure also leads naturally to microscopic expressions for the capture and escape lifetimes. Furthermore, we study how the capture efficiency is affected by the characteristics of the carrier-phonon interaction in semiconductors. To this purpose, we explicitly include in the analysis hot-phonon effects, i.e., the deviation from equilibrium in the phonon distribution function due to phonon emission [11]–[15]. These effects have been shown [13]–[15] to strongly affect the intraband relaxation dynamics of photoexcited carriers, by significantly reducing their cooling rate. Here, we consider (for the first time to our knowledge) the impact of these same effects on the capture dynamics; the results show that the effective capture rate is, in general, modified by these effects, and that interesting new regimes of carrier-phonon interaction may be

observed in the capture process.

We emphasize from the start that carrier-carrier scattering will not be included in this analysis, aside from its role in establishing a thermal distribution in each subband. In the presence of large densities of electrons and holes, it has been suggested [8] that carrier-carrier scattering may also give a contribution to the capture process comparable to that of phonon emission. Strictly speaking then the present analysis applies to conditions of moderate electrical pumping and/or high optical saturation (which is actually appropriate to SOA operation).

In order to make a connection with the FWM experiment described in the previous section, we will study the capture process in the frequency domain; to this purpose, we introduce in the analysis a time-harmonic perturbation to the occupancy of the 3D barrier states, and study the resulting coupled time evolution of the distribution functions of all electronic states (confined and unconfined) and phonon modes.

The carrier distribution functions are assumed to be quasi-Fermi functions at all times, so that their time evolution is entirely determined by that of the corresponding carrier numbers and temperatures. This is a valid assumption whenever the time scale of interest is longer than the intrasubband thermalization time, approximately 100 fsec under typical SOA conditions. In this analysis, the time scale of interest is set by the capture lifetime, typically longer than a picosecond, so that the above assumption is fully justified. For the same reason (which implies that thermalization within each subband is much faster than equilibration between bound and unbound carriers) we describe the 2D and 3D states (for each carrier type) as populated according

to two distinct Fermi distributions. These will be denoted by $f_{x2}(\vec{k})$ and $f_{x3}(\vec{k}, k_z)$ respectively, where the index x refers to the carrier type ($x : e, h$ for electrons and holes), and $\vec{k}$ is a 2D wavevector parallel to the plane of the QW.

Carrier-phonon scattering in polar semiconductors mainly occurs through the Fröhlich polar interaction which involves LO phonons only, although for holes non-polar deformation-potential scattering with both LO and TO vibrational modes also gives a contribution. The details of this interaction and its modification in the presence of quantum confinement [18]–[20] are not important at this stage, and we simply consider a generic set of LO phonon modes $\{n, \vec{q}\}$ (where n is the relevant branch index and $\vec{q}$ is a 2D in-plane wavevector), with energy $\hbar\omega_n$ (essentially constant with $\vec{q}$ as appropriate for optical phonon modes). The interaction of these modes with the electrical carriers will be characterized by some potential $V_n(\vec{q})$ (e.g., see Eq. 6.20 below). It is important to point out that the thermalization of these modes (which is governed by the anharmonic interaction with acoustic phonons [11], [12]) takes place on a relatively long time scale. From the available literature [12], [14], the phonon lifetime, τ_p, can be extrapolated to be approximately 2.5 psec (in GaAs) at room temperature, which is of the same order as the capture lifetime. As a result, the optical phonon distribution function $\eta_n(\vec{q})$ cannot be taken in this analysis to be a thermal distribution (i.e., a Bose-Einstein distribution corresponding to some time-varying temperature).

The Boltzmann equations governing the time evolution of $f_{x2}(\vec{k})$, $f_{x3}(\vec{k}, k_z)$ and $\eta_n(\vec{q})$ can be derived formally from the Heisenberg equations of motion for the cor-

responding quantum-mechanical number operators. This procedure is described in some detail in, e.g., Ref. [21], and in the case at hand it leads to the following set of coupled equations:

$$\frac{df_{x2}(\vec{k})}{dt} = -\frac{f_{x2}(\vec{k}) - f_{x2}^{eq.}(\vec{k})}{\tau_s} +$$
$$+\sum_{n,\vec{q}}\Bigg\{\left[P_{x2(\vec{k});x2(\vec{k}-\vec{q})}^{n(\vec{q})}\right]\left[\eta_n(\vec{q})\left(f_{x2}(\vec{k}-\vec{q}) - f_{x2}(\vec{k})\right) - f_{x2}(\vec{k})\left(1 - f_{x2}(\vec{k}-\vec{q})\right)\right] +$$
$$+\left[P_{x2(\vec{k}+\vec{q});x2(\vec{k})}^{n(\vec{q})}\right]\left[\eta_n(\vec{q})\left(f_{x2}(\vec{k}+\vec{q}) - f_{x2}(\vec{k})\right) + f_{x2}(\vec{k}+\vec{q})\left(1 - f_{x2}(\vec{k})\right)\right] +$$
$$+\sum_{k_z}\left[P_{x3(\vec{k}+\vec{q},k_z);x2(\vec{k})}^{n(\vec{q})}\right]\Big[\eta_n(\vec{q})\left(f_{x3}(\vec{k}+\vec{q},k_z) - f_{x2}(\vec{k})\right)$$
$$+f_{x3}(\vec{k}+\vec{q};k_z)\left(1 - f_{x2}(\vec{k})\right)\Big]\Bigg\}, \tag{6.3}$$

$$\frac{df_{x3}(\vec{k},k_z)}{dt} = -\frac{f_{x3}(\vec{k},k_z) - f_{x3}^{eq.}(\vec{k},k_z)}{\tau_s} + g_{x3}(\vec{k},k_z) +$$
$$+\sum_{n,\vec{q}}\Bigg\{\sum_{k_z'}\left[P_{x3(\vec{k},k_z);x3(\vec{k}-\vec{q},k_z')}^{n(\vec{q})}\right]\Big[\eta_n(\vec{q})\left(f_{x3}(\vec{k}-\vec{q},k_z') - f_{x3}(\vec{k},k_z)\right)$$
$$-f_{x3}(\vec{k},k_z)\left(1 - f_{x3}(\vec{k}-\vec{q},k_z')\right)\Big] +$$
$$+\sum_{k_z'}\left[P_{x3(\vec{k}+\vec{q},k_z');x3(\vec{k},k_z)}^{n(\vec{q})}\right]\Big[\eta_n(\vec{q})\left(f_{x3}(\vec{k}+\vec{q},k_z') - f_{x3}(\vec{k},k_z)\right)$$
$$+f_{x3}(\vec{k}+\vec{q},k_z')\left(1 - f_{x3}(\vec{k},k_z)\right)\Big] +$$
$$+\left[P_{x3(\vec{k},k_z);x2(\vec{k}-\vec{q})}^{n(\vec{q})}\right]\Big[\eta_n(\vec{q})\left(f_{x2}(\vec{k}-\vec{q}) - f_{x3}(\vec{k},k_z)\right)$$
$$-f_{x3}(\vec{k},k_z)\left(1 - f_{x2}(\vec{k}-\vec{q})\right)\Big]\Bigg\}, \tag{6.4}$$

$$\frac{d\eta_n(\vec{q})}{dt} = -\frac{\eta_n(\vec{q}) - \eta_n^{eq.}(\vec{q})}{\tau_p} +$$

$$-\sum_{x:e,h}\sum_{\vec{k}}\Bigg\{\left[P_{x2(\vec{k});x2(\vec{k}-\vec{q})}^{\;\;n(\vec{q})}\right]\left[\eta_n(\vec{q})\left(f_{x2}(\vec{k}-\vec{q})-f_{x2}(\vec{k})\right)-f_{x2}(\vec{k})\left(1-f_{x2}(\vec{k}-\vec{q})\right)\right]+$$

$$+\sum_{k_z,k_z'}\left[P_{x3(\vec{k},k_z);x3(\vec{k}-\vec{q},k_z')}^{\;\;n(\vec{q})}\right]\Big[\eta_n(\vec{q})\left(f_{x3}(\vec{k}-\vec{q},k_z')-f_{x3}(\vec{k},k_z)\right)$$

$$-f_{x3}(\vec{k},k_z)\left(1-f_{x3}(\vec{k}-\vec{q},k_z')\right)\Big]+$$

$$+\sum_{k_z}\left[P_{x3(\vec{k},k_z);x2(\vec{k}-\vec{q})}^{\;\;n(\vec{q})}\right]\Big[\eta_n(\vec{q})\left(f_{x2}(\vec{k}-\vec{q})-f_{x3}(\vec{k},k_z)\right)$$

$$-f_{x3}(\vec{k},k_z)\left(1-f_{x2}(\vec{k}-\vec{q})\right)\Big]\Bigg\}, \tag{6.5}$$

where the superscript *eq.* denotes the quasi-equilibrium distribution functions, determined by the steady-state electrical injection and by the lattice temperature, and τ_s is the interband recombination lifetime. Furthermore,

$$\left[P_{\alpha;\,\beta}^{\;\;n(\vec{q})}\right]=\frac{2\pi}{\hbar}\left|\langle\alpha|-eV_n(\vec{q})|\beta\rangle\right|^2\delta\left(\epsilon_\alpha-\epsilon_\beta-\hbar\omega_n(\vec{q})\right) \tag{6.6}$$

is the probability rate that a phonon is emitted into (absorbed from) mode $\{n,\vec{q}\}$, with a carrier simultaneously making a transition from state α to state β (or from β to α). The different terms in Eq. (6.3) and (6.4) describe all possible transitions in and out of state $x2(\vec{k})$ and $x3(\vec{k},k_z)$ respectively, under absorption and emission (both stimulated and spontaneous) of LO phonons (for simplicity we assume only one 2D subband for each carrier type). Finally, $g_{x3}(\vec{k},k_z)$ on the right-hand side of (6.4) denotes a time-harmonic external perturbation to the 3D carrier distribution at frequency Ω (e.g., arising from beating of the pump waves in a FWM experiment).

Before proceeding to solve Eqs. (6.3)–(6.5), we notice that this model implicitly assumes that the unbound states are Bloch waves extended over the entire separate confinement region, for which the transverse wavevector k_z remains a good quantum

number. In fact, carrier-carrier scattering causes a large lifetime broadening, and hence a strong reduction in the coherence length of the 3D carriers, so that they are expected to behave more like semiclassical wavepackets. Their dynamics can be included in this analysis using the formalism developed in Ref. [22]. However, while the formulation of the problem becomes much more involved, the result is simply a rescaling of the capture lifetime by a geometrical factor in the final expressions for the capture efficiency, Eqs. (6.16)–(6.19) below (for instance, using the simple model for carrier diffusion employed in chapter 4 to study interwell transport, this factor is the ratio of the QW width to the barrier width). For the sake of simplicity, we will continue to use Bloch waves in the analysis (furthermore, under the experimental conditions of the previous section, interwell transport is not important and it seems appropriate to leave it out of the analysis).

6.3.1 Rate Equations

Next we use the Boltzmann equations (6.3)–(6.5) to derive a set of rate equations for the densities of confined and unconfined carriers and for the occupation numbers of all the relevant phonon modes. To this purpose, we first expand the distribution functions about their quasi-equilibrium values as follows:

$$f_{x2(3)} \approx f^{eq.}_{x2(3)} + \frac{\partial f^{eq.}_{x2(3)}}{\partial N}\left[\Delta N^{(0)}_{x2(3)} + \left(N^{(\Omega)}_{x2(3)}\, e^{-i\Omega t} + c.c.\right)\right] \tag{6.7}$$

$$\eta_n(\vec{q}) \approx \eta^{eq.}_n(\vec{q}) + \Delta\eta^{(0)}_n(\vec{q}) + \left(\eta^{(\Omega)}_n(\vec{q})\, e^{-i\Omega t} + c.c.\right) \tag{6.8}$$

Notice that we are not including here the carrier temperature dynamics; this omission will considerably simplify the analysis, and it is based on the consideration that the

lattice temperature is restored in each subband with a lifetime of approximately 600 fsec [23], [24], which is relatively fast on the time scale of the capture process.

The rate equations for the carrier density modulations $N_{x2}^{(\Omega)}$ and $N_{x3}^{(\Omega)}$ are then obtained by substituting Eqs. (6.7)–(6.8) in (6.3)–(6.4), retaining only terms up to second order in the external perturbation, and summing the resulting equations over all values of $\vec{k}$ (and of k_z for (6.4)). This procedure gives

$$\left(-i\Omega + \frac{1}{\tau_s} + \frac{1}{\tau_{esc}^x}\right) N_{x2}^{(\Omega)} = \sum_{n,\vec{q}} r_{cp}^x(n,\vec{q})\eta_n^{(\Omega)}(\vec{q}) + \frac{1}{\tau_{cap}^x} N_{x3}^{(\Omega)}, \tag{6.9}$$

$$\left(-i\Omega + \frac{1}{\tau_s} + \frac{1}{\tau_{cap}^x}\right) N_{x3}^{(\Omega)} = g_{x3}^{(\Omega)} - \sum_{n,\vec{q}} r_{cp}^x(n,\vec{q})\eta_n^{(\Omega)}(\vec{q}) + \frac{1}{\tau_{esc}^x} N_{x2}^{(\Omega)}, \tag{6.10}$$

where we defined $g_{x3}^{(\Omega)} = \sum_{\vec{k},k_z} g_{x3}^{(\Omega)}(\vec{k},k_z)$, and furthermore we introduced the capture lifetime τ_{cap}^x, the escape lifetime τ_{esc}^x, and an additional carrier-phonon coupling rate $r_{cp}^x(n,\vec{q})$, given by

$$\frac{1}{\tau_{cap}^x} = \sum_{n,\vec{q}} \sum_{\vec{k},k_z} \left[P_{x3(\vec{k},k_z);x2(\vec{k}-\vec{q})}^{n(\vec{q})}\right] \left(\eta_n^{eq.}(\vec{q}) + 1 - f_{x2}^{eq.}(\vec{k}-\vec{q})\right) \frac{\partial f_{x3}^{eq.}}{\partial N}(\vec{k},k_z), \tag{6.11}$$

$$\frac{1}{\tau_{esc}^x} = \sum_{n,\vec{q}} \sum_{\vec{k},k_z} \left[P_{x3(\vec{k},k_z);x2(\vec{k}-\vec{q})}^{n(\vec{q})}\right] \left(\eta_n^{eq.}(\vec{q}) + f_{x3}^{eq.}(\vec{k},k_z)\right) \frac{\partial f_{x2}^{eq.}}{\partial N}(\vec{k}-\vec{q}), \tag{6.12}$$

$$r_{cp}^x(n,\vec{q}) = \sum_{\vec{k},k_z} \left[P_{x3(\vec{k},k_z);x2(\vec{k}-\vec{q})}^{n(\vec{q})}\right] \left(f_{x3}^{eq.}(\vec{k},k_z) - f_{x2}^{eq.}(\vec{k}-\vec{q})\right). \tag{6.13}$$

As for the phonon occupation factors $\eta_n(\vec{q})$, we first notice that their time evolution is in principle coupled to that of both numbers and temperatures of both confined and unconfined carriers of both types. This is because phonons can be emitted and absorbed in a variety of relaxation processes, including capture/escape of both carrier types, as well as temperature equilibration of each subband to the lattice. However, due to the requirements of energy and momentum conservation, each one of these

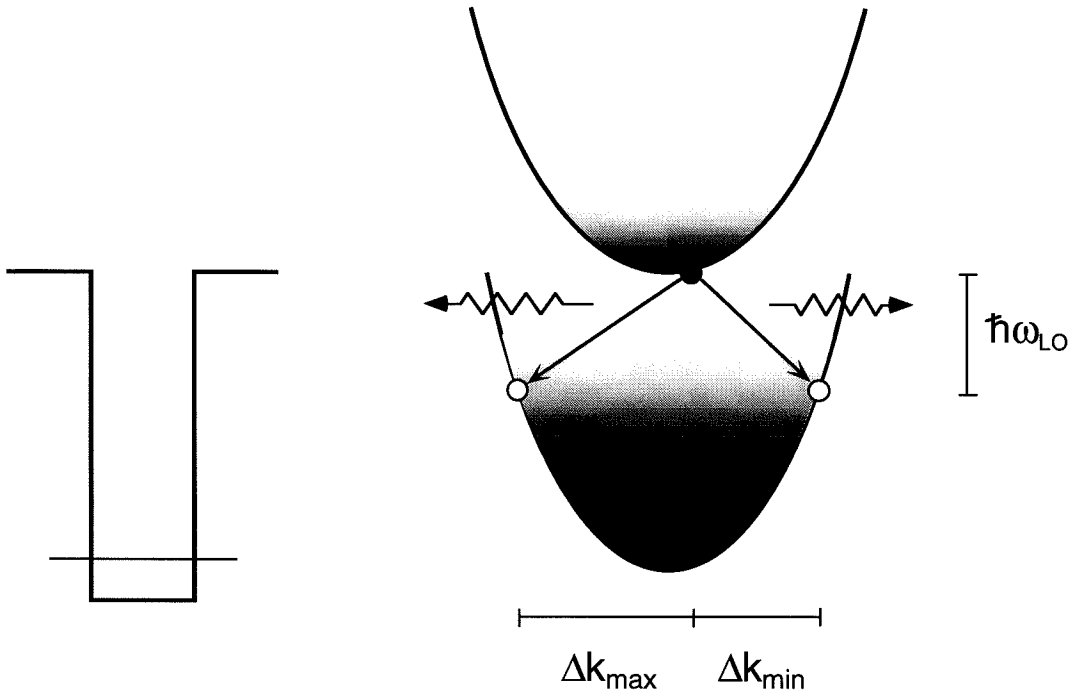

Figure 6.4: Schematics of the intersubband transitions involved in the electron capture process. Due to the requirements of conservation of energy and momentum, only a restricted set of phonon modes (the ones having parallel momentum between Δk_{min} and Δk_{max}) can participate in this process.

processes can only involve a restricted set of phonon modes. This is illustrated for the case of electron capture in Fig. 6.4: the states near the bottom of the 3D band (i.e., the only unconfined states with nonnegligible occupancy) can only emit phonons with a small range of values of in-plane momentum (with magnitude between Δk_{min} and Δk_{max} in the figure). In fact, a simple calculation based on a bulk phonon approximation for an InGaAsP MQW SOA (briefly described in the next section), shows that the rate $r_{cp}^{x=e}(\vec{q})$ is nonnegligible over a fraction of phase space on the order of 1% of the entire volume of the Brillouin zone. Similar considerations apply to the

capture of holes (as well as to the intrasubband processes responsible for temperature equilibration to the lattice).

In view of these considerations, we will assume that the phonon modes involved in the capture of carriers of type x are not significantly affected by any other relaxation process (ultimately, this depends on the details of the electronic band structure, which determines the momentum of the phonons that can be emitted and absorbed in each process). This approximation considerably simplifies the analysis because then the occupation numbers of these modes (which will be denoted by $\eta_{n,x}(\vec{q})$) are only coupled to N_{x2} and N_{x3}. The corresponding rate equations are obtained by substituting Eqs. (6.7)–(6.8) in (6.5) and simplifying, which gives

$$\left(-i\Omega + \frac{1}{\tau_p} - r_{cp}^{x}(n,\vec{q})\right)\eta_{n,x}^{(\Omega)}(\vec{q}) = \frac{1}{\tau_{cap}^{x}(n,\vec{q})}N_{x3}^{(\Omega)} - \frac{1}{\tau_{esc}^{x}(n,\vec{q})}N_{x2}^{(\Omega)} \tag{6.14}$$

where $1/\tau_{cap}^{x}(n,\vec{q})$ and $1/\tau_{esc}^{x}(n,\vec{q})$ denote the contributions to the overall capture and escape rates, respectively, associated with the phonon mode $\{n,\vec{q}\}$.

6.3.2 Phonon Amplification

It is apparent from the rate equation (6.14) that the carrier-phonon coupling rate $r_{cp}^{x}(n,\vec{q})$ effectively acts as an amplification rate for the phonon mode $\{n,\vec{q}\}$. According to (6.13), the sign of this parameter is determined by the Fermi inversion factor $f_{x3}^{eq.}(\vec{k},k_z) - f_{x2}^{eq.}(\vec{k}-\vec{q})$, which *can* be positive even if the 3D state $x3(\vec{k},k_z)$ is higher in energy than the 2D state $x2(\vec{k}-\vec{q})$. This is because the carriers injected in the barrier region relax to the bottom of the 3D band to establish the quasi-Fermi distribution $f_{x3}^{eq.}$ (via carrier-carrier scattering) with a characteristic time constant that

is typically much shorter than the capture lifetime. The resulting carrier distribution is schematically illustrated in Fig. 6.4, where the shading is used to denote the occupancy of the electronic states. We see from this figure that, while the lower band (consisting of quantum-confined states) is as a whole much more populated than the upper one, it is possible for the states at the bottom of the 3D parabola to have higher occupation probability than the 2D states lying lower in energy by the amount $\hbar\omega_n$. Then, the pairs of unbound/bound states involved in the capture process are effectively inverted, and as such provide gain for the appropriate phonon modes.

A careful examination of (6.13) shows that the value of $r_{cp}^{x}(n,\vec{q})$ (magnitude and sign) depends on a wide variety of material and structural parameters. For instance, it increases with increasing QW width, barrier height, density of 2D states, and number of QWs, and with decreasing density of 3D states, volume of the separate confinement region, and LO phonon energy. It would then seem possible to design a structure in which this rate can be made positive and large; in fact, it is found to be (slightly) positive in the simple calculation described in the next section. In particular, if it were made larger than the inverse phonon lifetime $1/\tau_p$, and an appropriate cavity were designed (in particular the isotropy of $r_{cp}^{x}(n,\vec{q})$ on the QW plane suggests a circular cavity), one could envision a coherent source of optical phonons based on carrier capture.

6.3.3 Capture Efficiency

Under the experimental conditions considered in this work (i.e., in the presence of an external modulation of the unbound carriers at some frequency Ω), a quantitative

measure of the capture efficiency is provided by the complex amplitude at Ω of the number of quantum-confined carriers. Notice that $N_{x2}^{(\Omega)}$ is always proportional to $1/(-i\Omega+1/\tau_s)$, which simply reflects the damping of any external perturbation to the carrier density due to interband recombination. Since this contribution is completely unrelated to the capture process, we normalize out this factor and define the capture efficiency (for the carriers of type x) as follows:

$$Z_x(\Omega) \equiv \frac{(-i\Omega + 1/\tau_s)\, N_{x2}^{(\Omega)}}{g_{x3}^{(\Omega)}}. \tag{6.15}$$

Notice that this frequency response function (for x corresponding to the slower carrier type, i.e., the electrons [3]) is what we measure in the FWM experiment of the previous section, after subtracting out the low-frequency 20 dB/dec roll-off (as shown in the inset of Fig. 6.3).

Using the coupled set of equations (6.9), (6.10) and (6.14), we find after some straightforward algebra

$$Z_x(\Omega) = \frac{\sum_{n,\vec{q}} 1/\tau_{cap}^x(n,\vec{q}) \frac{-i\Omega+1/\tau_p}{-i\Omega+1/\tau_p - r_{cp}^x(n,\vec{q})}}{\sum_{n,\vec{q}} \frac{1/\tau_{esc}^x(n,\vec{q})+1/\tau_{cap}^x(n,\vec{q})}{1/\tau_{esc}^x+1/\tau_{cap}^x} \frac{\left(-i\Omega+r_+^x(n,\vec{q})\right)\left(-i\Omega+r_-^x(n,\vec{q})\right)}{-i\Omega+1/\tau_p-r_{cp}^x(n,\vec{q})}} \tag{6.16}$$

where

$$r_\pm^x(n,\vec{q}) = \frac{1}{2}\left(\frac{1}{\tau_{eff}^x} + \frac{1}{\tau_p} - r_{cp}^x(n,\vec{q})\right) + \pm\sqrt{\frac{1}{4}\left(\frac{1}{\tau_{eff}^x} + \frac{1}{\tau_p} - r_{cp}^x(n,\vec{q})\right)^2 + \frac{r_{cp}^x(n,\vec{q})}{\tau_s} - \frac{1}{\tau_p\tau_{eff}^x}} \tag{6.17}$$

and

$$\frac{1}{\tau_{eff}^x} \equiv \frac{1}{\tau_s} + \frac{1}{\tau_{esc}^x} + \frac{1}{\tau_{cap}^x}. \tag{6.18}$$

The capture efficiency given in Eq. (6.16) is a complicated function of the modulation frequency Ω, and an involved numerical integration is required for an exact study

of its properties. As a final simplification we again take advantage of the fact that the rate $r_{cp}^x(n,\vec{q})$ (as well as $1/\tau_{cap}^x(n,\vec{q})$ and $1/\tau_{esc}^x(n,\vec{q})$) are sharply peaked in the (same) small volume of the phonon state space. Since the terms in the summations of both the numerator and the denominator of (6.16) are weighted by these rates, the main contribution to both summations comes from those modes for which $r_{cp}^x(n,\vec{q})$ is nearly equal to its peak value (which will be denoted by r_{cp}^x). If we discard all other contributions, the capture efficiency takes on the simple form

$$Z_x(\Omega) \approx \frac{1}{\tau_{cap}^x} \frac{-i\Omega + 1/\tau_p}{(-i\Omega + r_+^x)(-i\Omega + r_-^x)} \tag{6.19}$$

where $r_\pm^x$ is given by (6.17) with $r_{cp}^x(n,\vec{q})$ replaced by r_{cp}^x.

The frequency dependence of the capture efficiency of Eq. (6.19) is determined by the nature of its two poles $r_\pm^x$. Consider first the limit of very weak carrier-phonon coupling, in which the carrier-phonon coupling rate r_{cp}^x is negligible (relative to $1/\tau_p$ and $1/\tau_{eff}^x$). In this limit, $r_+^x \approx 1/\tau_{eff}^x$ and $r_-^x \approx 1/\tau_p$, so that the capture efficiency simply becomes a single-pole function of the modulation frequency Ω, with 3-dB corner frequency equal to $1/(2\pi\tau_{eff}^x)$. Incidentally, we point out that this 3-dB corner frequency is a measure of the largest modulation frequency that is efficiently captured in the QW. The model used in the previous section to interpret the measured data implicitly assumed this regime of carrier-phonon coupling.

On the other hand, if we imagine increasing the magnitude of r_{cp}^x, $Z_x(\Omega)$ will initially retain the same qualitative frequency dependence as above, but with a larger or smaller bandwidth depending on whether r_{cp}^x is positive or negative. Physically, this

reflects the fact that the additional phonons created in the capture process lead to an increased effective capture rate through stimulated emission or to a decreased effective capture rate through reabsorption, depending on the sign of the Fermi inversion factor for the capture transitions, $f_{x3}^{eq.}(\vec{k}, k_z) - f_{x2}^{eq.}(\vec{k} - \vec{q})$. This is entirely analogous to the effect of hot-phonons on the thermal relaxation of excited carrier distributions [13]–[15], except that in that case the corresponding inversion factor (associated with intraband transitions) is always negative, and hence the net result is always a decrease in the cooling rate.

Finally, in the limit of large positive r_{cp}^{x}, the quantity under square root in Eq. (6.17) becomes negative, so that $Z(\Omega)$ is characterized by a pair of complex-conjugate poles, $r_{\pm}^{x} \equiv K \pm i\Omega_R$. As a result, a resonance peak is introduced in the capture efficiency at Ω_R, of width proportional to K. In this regime, the capture rate undergoes damped harmonic oscillations in time at the frequency Ω_R, similar to the relaxation oscillations characteristic of, e.g., laser operation.

6.4 Conclusions and Outlook

From the discussion above, the question arises of what is the numerical value of the carrier-phonon coupling rate r_{cp}^{x} in a typical InGaAsP SOA, such as the one used in the experiment of section 6.2. The evaluation of this quantity, through Eq. (6.13), is nontrivial, both from a numerical standpoint, and because it requires detailed knowledge of both the electron and the phonon dispersions.

For a rough estimate, we will assume a bulk-like LO phonon dispersion with

wavevector-independent energy. The electron-phonon polar interaction potential is then given by [19]

$$V(\vec{q}, q_z) = \sqrt{\frac{\hbar\omega_n}{2V_a\epsilon_0}\left(\frac{1}{\kappa_s} - \frac{1}{\kappa_\infty}\right)}\frac{e^{i(\vec{q}.\vec{r}+q_z z)}}{\sqrt{q^2+q_z^2}}, \tag{6.20}$$

where κ_s and κ_∞ denote the static and high-frequency dielectric constants respectively, and V_a is the volume of the active region. Furthermore, we make the infinite-barrier approximation for the envelope functions of the 2D states, while the 3D states are taken to be plane waves, and a parabolic dispersion relation with the same effective mass m^* is assumed for both subbands. The following values of the relevant parameters are used: $m^* = 0.050\ m_0$; ΔE_c (the QW potential barrier) = 145 meV; $V_a = 780 \times 2.5 \times 0.1\ \mu m^3$; $\hbar\omega_{LO} = 34$ meV; $\kappa_s = 13.16$; $\kappa_\infty = 10.255$; I (the bias current) = 140 mA; $N_{e2}^{eq.}/N_{e3}^{eq.} = 5$ (approximately the ratio of the capture rate to the escape rate measured in section 4 [9]); $T^{eq.} = 300$ K.

With these prescriptions, we obtained an estimate of $r_{cp}^e \approx +0.12$ psec^{-1}. If we take $\tau_{cap} < 1.8$ psec, as it follows from the experimental data of section 6.2, the neglect of hot phonon effects from the interpretation of these data seems reasonable. It should be mentioned though that if phase matching turns out to be unimportant in the experiment, the high-frequency features observed in Fig. 6.3 could be revisited in light of Eq. (6.16).

In any case, the expression (6.13) for the carrier-phonon coupling rate suggests that it should be possible to vary this quantity over a fairly large range by proper design of the SOA active layer. This would then allow us to experimentally observe the different regimes of phonon-assisted capture discussed above. Hot-phonon effects

are well known to play an important role in the intraband thermalization of excited carriers, and therefore it should not be surprising that they might have an equally important impact on carrier capture in some devices. As we mentioned earlier the capture rate is a quantity of large practical interest due to its relation with the modulation bandwidth of QW lasers, and much effort has been devoted to maximize it. The results of this chapter offer new guidelines to this goal, regarding an aspect of the capture process (i.e., phonon dynamics) that has been overlooked so far.

Bibliography

[1] J. Shah, *Ultrafast Spectroscopy of Semiconductors and Semiconductor Nanostructures.* Berlin, Germany: Springer-Verlag, 1996.

[2] B.K. Ridley, "Hot electrons in low-dimensional structures," *Rep. Prog. Phys.*, vol. 54, pp. 169–256, 1991.

[3] B. Deveaud, J. Shah, T.C. Damen, and W.T. Tsang, "Capture of electrons and holes in quantum wells," *Appl. Phys. Lett.*, vol. 52, pp. 1886–1888, 1988.

[4] M.R.X. Barros, P.C. Becker, D. Morris, B. Deveaud, A. Regreny, and F.A. Beisser, "Ultrafast optical evidence for resonant electron capture in quantum wells," *Phys. Rev. B*, vol. 47, pp. 10951-10954, 1993.

[5] S. Weiss, J. M. Wiesenfeld, D. S. Chemla, G. Raybon, G. Sucha, M. Wegener, G. Eisenstein, C. A. Burrus, A. G. Dentai, U. Koren, B. I. Miller, H. Temkin, R. A. Logan, and T. Tanbun-Ek, "Carrier capture times in 1.5 μm multiple quantum well optical amplifiers," *Appl. Phys. Lett.*, vol. 60, pp. 9–11, 1992.

[6] S. C. Kan, D. Vassilovski, T. C. Wu, and K. Y. Lau, "Quantum capture and escape in quantum-well lasers-implications on direct modulation bandwidth limitations," *Appl. Phys. Lett.*, vol. 61, pp. 752–754, 1992.

[7] D. Vassilovski, T. C. Wu, S. Kan, K. Y. Lau, and C. E. Zah, "Unambiguous determination of quantum capture, carrier diffusion, and intrinsic effects in quantum-well laser dynamics using wavelength-selective optical modulation," *IEEE Photon. Tech. Lett.*, vol. 7, pp. 706–708, 1995.

[8] J.E.M. Haverkort, P.W.M. Blom, P.J. van Hall, J. Claes, and J.H. Wolter, "Capture of carriers into a GaAs/AlGaAs quantum well: relevance to laser performance," *Phys. Stat. Sol.*, vol. 188, pp. 139–152, 1995.

[9] R. Paiella, G. Hunziker, K. J. Vahala, and U. Koren, "Measurement of the interwell carrier transport lifetime in multiquantum-well optical amplifiers by polarization-resolved four-wave mixing," *Appl. Phys. Lett.*, vol. 69, pp. 4142–4144, 1996.

[10] R. Paiella, G. Hunziker, U. Koren, and K. J. Vahala, "Four-wave mixing mediated by the capture of electrons and holes in semiconductor quantum-well laser amplifiers," *Appl. Phys. Lett.*, vol.71, pp. 3601–3603, 1997.

[11] J. Shah, R.C.C. Leite, and J.F. Scott, "Photoexcited hot LO phonons in GaAs," *Solid State Commun.*, vol. 8, pp. 1089-1093, 1970.

[12] D. von der Linde, J. Kuhl, and H. Klingenberg, "Raman scattering from nonequilibrium LO phonons with picosecond resolution," *Phys. Rev. Lett.*, vol. 44, pp. 1505-1508, 1980.

[13] J. Collet, A. Cornet, M. Pugnet, and T. Amand, "Cooling of high-density electron-hole plasma," *Solid State Commun.*, vol. 42, pp. 883-887, 1982.

[14] W. Pötz, and P. Kocevar, "Electronic power transfer in pulsed laser excitation of polar semiconductors," *Phys. Rev. B*, vol. 28, pp. 7040-7047, 1983.

[15] J. Shah, A. Pinczuk, A.C. Gossard, and W. Wiegmann, "Energy-loss rates for hot electrons and holes in GaAs quantum wells," *Phys. Rev. Lett.*, vol. 54, pp. 2045-2048, 1985.

[16] M. A. Newkirk, B. I. Miller, U. Koren, M. G. Young, M. Chien, R. M. Jopson, and C. A. Burrus, "1.5 μm multiquantum-well semiconductor optical amplifier with tensile and compressively strained wells for polarization-independent gain," *IEEE Photon. Technol. Lett.*, vol. 4, pp. 406–408, 1993.

[17] G. Hunziker, R. Paiella, K. J. Vahala, and U. Koren, "Measurement of the stimulated carrier lifetime in semiconductor optical amplifiers by four-wave mixing of polarized ASE noise," *IEEE Photon. Technol. Lett.*, vol. 9, pp. 907–909, 1997.

[18] M. Babiker, "Longitudinal polar optical modes in semiconductor quantum wells," *J. Phys. C*, vol. 19, pp. 683-697, 1986.

[19] K. Huang and B. Zhu, "Dielectric continuum model and Fröhlich interaction in superlattices," *Phys. Rev. B*, vol. 38, pp. 13377-13386, 1988.

[20] H. Rücker, E. Molinari, and P. Lugli, "Microscopic calculation of the electron-phonon interaction in quantum wells," *Phys. Rev. B*, vol. 45, pp. 6747-6756, 1992.

[21] H. Haug and S. W. Koch, *Quantum Theory of the Optical and Electronic Properties of Semiconductors.* World Scientific, 1993.

[22] K. Vahala and A. Yariv, "Application of an electronic wave-packet formalism to local-operator equations of motion for semiconductor lasers," *Phys. Rev. A*, vol. 32, pp. 345-356, 1985.

[23] K. L. Hall, J. Mark, E. P. Ippen, and G. Eisenstein, "Femtosecond gain dynamics in InGaAsP optical amplifiers," *Appl. Phys. Lett.*, vol. 56, pp. 1740–1742, 1990.

[24] J. Zhou, N. Park, J. W. Dawson, K. J. Vahala, M. A. Newkirk, and B. I. Miller, "Terahertz four-wave mixing spectroscopy for study of ultrafast dynamics in a semiconductor optical amplifier," *Appl. Phys. Lett.*, vol. 63, pp. 1179 – 1181, 1993.

Chapter 7

Wavelength Conversion by FWM in Semiconductor Optical Amplifiers

7.1 Introduction

A worldwide consensus has recently emerged on the utilization of wavelength-division multiplexing (WDM) technologies in fiber-optic communication systems. Indeed, WDM networks with ever increasing aggregate bandwidth are already being realized and deployed. At the same time, new device concepts and implementations, as well as new network architectures, are being studied, specifically designed to meet the needs of the multiple WDM wavelength channels. An important example is provided by wavelength conversion devices: while their precise role in future network architectures is still a subject of investigation, it is clear that the function they provide is extremely

useful [1]–[3]. In particular, these devices could be used to improve the overall efficiency of a network (for instance by reducing channel blocking due to wavelength contention [2], [3]) and to increase its scalability [1].

As a result, several techniques are currently being investigated for the implementation of wavelength conversion [4]. Broadly speaking, they can be classified into three main categories, namely optoelectronic, optical gating, and wave mixing technologies. Optoelectronic wavelength conversion simply consists of detection of the optical signal and retransmission at a different wavelength [5]. While this is the simplest and most mature technology to date, it is expected to become less and less competitive as the bit rate and the number of elements increase, due to cost and packaging considerations. Optical gating refers to the change in the transmission properties of a nonlinear optical device by a digitally modulated input signal; this change is probed by a cw beam at a different wavelength, which is correspondingly modulated with the same information. This category of wavelength converters includes devices based on cross-gain [6], [7] or cross-phase modulation [8]–[10] in SOAs, which have recently demonstrated excellent performance in terms of speed and noise properties. Finally, in the case of wave mixing the converted signal is generated through the nonlinear optical mixing of the input signal with one (or more) cw pump waves. Because of the coherent nature of this process, it preserves both intensity and phase information: as a result, wave mixing wavelength converters have the unique advantage of being strictly transparent to the modulation format (as well as to the bit rate).

The wave mixing process studied in this thesis, i.e., nondegenerate FWM in SOAs,

is an important example of the latter category of wavelength conversion mechanisms [11]–[14]. Notice that unlike other wave mixing techniques (such as FWM in optical fibers [15] or difference frequency generation in $LiNbO_3$ [16] or in passive semiconductor waveguides [17]), this mechanism does not require any careful control of the mixing wavelengths to minimize the phase mismatch (which is negligibly small for practical device lengths and wavelength shifts, see Eq. 7.1 below). As a result, at present FWM in SOAs is the only wavelength conversion technique that offers arbitrary wavelength mapping while simultaneously being strictly transparent. Further advantages, common to all other wave mixing techniques, include the possibility of multi-channel operation [18]–[19], [13] and dispersion compensation by optical phase conjugation [20]–[21], [13].

The main challenges involved in the development of a high-performance wavelength converter based on FWM in SOAs are the limited conversion efficiency (and hence optical signal-to-noise ratio (OSNR) of the converted signal) at large wavelength shifts (see Fig. 2.4), and its polarization dependence (see section 3.4). As will be discussed and demonstrated in the next two sections, the former issue can be dealt with by: (I) using a high-power EDFA to amplify the input waves fed into the SOA (in conjunction with optical prefiltering of the EDFA amplified-spontaneous-emission (ASE) noise in the spectral region of the converted signal); (II) using longer SOAs to increase the FWM interaction length. With these prescriptions, we recently obtained error-free FWM wavelength conversion at 10 Gbit/sec over a record 30 nm shift [22] (results at 40 Gbit/sec have also been demonstrated by a group at British

Telecom [23]). Furthermore, in section 7.4 we show how the FWM conversion efficiency of SOAs can be made polarization insensitive using a dual-pump configuration [24], [25], and demonstrate this idea at 2.5 Gbit/sec. While further challenges remain to be overcome (most notably the present lack of a simple technique to suppress the pump wave and the input signal from the output of the SOA), these results are promising towards the development of a practical device based on FWM. Additional improvements in the design of this device, based on using a semiconductor laser in place of the SOA, will be discussed in the next chapter.

7.2 Wavelength Converter Design

The bit-error-rate (BER) performance of any wavelength conversion device is mainly determined by the OSNR of the converted signal, and therefore the design of such a device should focus on maximizing this quantity. In the case of FWM in SOAs, it is important to this purpose that the entire physical length of the amplifier be efficiently used in generating the FWM signal (as opposed to in amplifying the input waves). In practice, this is achieved by using a high-power EDFA to boost up the pump wave and the input signal before these are coupled into the SOA, which is then operated in a fully saturated regime.

Furthermore, in order to filter out the ASE noise power emitted by the EDFA in the spectral region of the converted signal, a broad band-pass filter (BPF) is inserted between the EDFA and the SOA [26] (with passband encompassing both the input signal and the pump wave). Then, the OSNR of the converted signal is limited by

the ASE noise power from the SOA itself. The importance of this filter is clearly illustrated in the bottom panel of Fig. 7.1 (from Ref. [13]), which shows a typical optical spectrum at the output of the SOA used in a FWM wavelength converter. We see from this figure that the ASE prefiltering improves the OSNR of the converted signal by more than 10 dB.

Incidentally, it has been demonstrated [27], [14] that increasing the pump power well beyond the SOA saturation power actually causes a degradation in the FWM conversion efficiency, due to gain saturation. However, in this regime a larger pump power also leads to a lower ASE noise power from the SOA: the net result is that the OSNR of the converted signal increases monotonically with pump power. Therefore, the largest input power available is used for optimum performance.

These prescriptions lead to the wavelength converter design [13] shown in Fig. 7.1. The pump wave is typically provided by a tunable external-cavity semiconductor laser (with wavelength tuned to select the desired destination wavelength of the converted signal). Two polarization controllers (PCs) are used to separately align the polarization states of the two input waves to each other (and to the axis of maximum optical gain) in the SOA. The pump wave and the input signal are then combined in a bidirectional coupler (BDC), amplified in a high-power EDFA, and passed through a BPF for ASE prefiltering (the broadest pass-band available in the lab was 14 nm). Finally, the two waves are input to the SOA, with approximately +13 dBm of typical total power coupled into the device. At the output of the SOA, a 1-nm BPF is used to isolate the desired output (i.e., the converted signal) and suppress the amplified

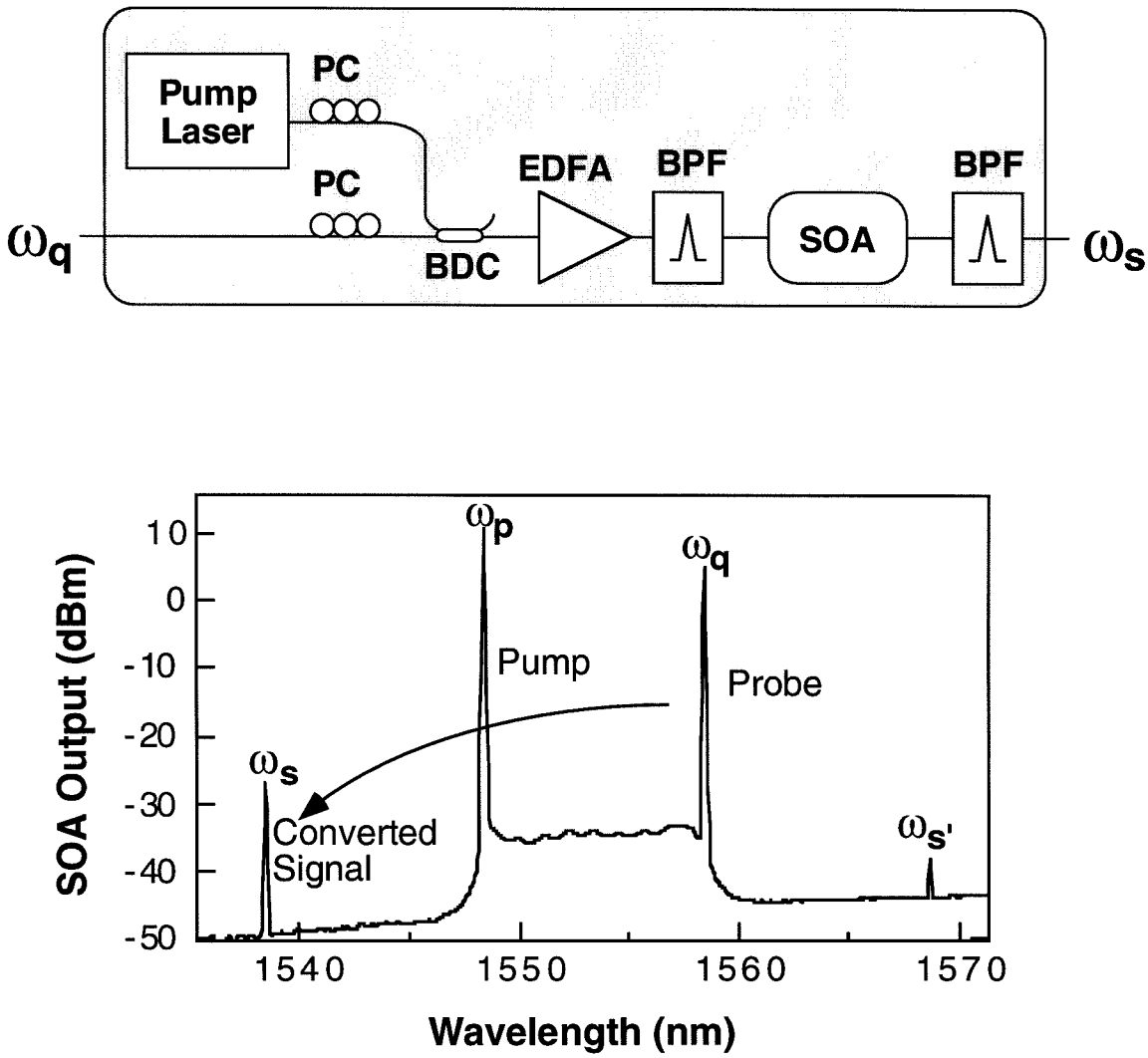

Figure 7.1: Schematic representation of the wavelength conversion device based on FWM in a SOA (all the acronyms are explained in the text). The bottom panel [13] shows the optical spectrum at the output of the SOA for a 20 nm wavelength downshift (0.1 nm resolution bandwidth).

pump wave and input signal.

Further improvements in the OSNR of the converted signal can be obtained using longer SOAs to increase the nonlinear interaction length. This leads to a larger FWM signal at the output of the SOA provided that the effect of phase-matching remains negligible. Based on a recent measurement of the group index dispersion in an InGaAsP SOA [28] ($dn_g/d\lambda \approx -0.7\mu\text{m}^{-1}$), we estimate that the first phase-matching null in the FWM conversion efficiency of a device of length L occurs at a wavelength shift equal to

$$\Delta\lambda_{null} \approx \frac{117 \text{ nm}}{\sqrt{\text{L(mm)}}}. \tag{7.1}$$

The largest SOA length used in this work, 1.5 mm, corresponds to $\Delta\lambda_{null} \approx 95$ nm, which is too large to be of practical interest anyway. Notice that increasing the length also causes a larger ASE noise power at the output of the SOA; the net effect, however, is an increase in the OSNR of the FWM signal (although by a smaller amount than the corresponding increase in FWM efficiency).

These predictions were first theoretically quantified by the authors of Ref. [14]. In Figs. 7.2a and 7.2b, we plot FWM conversion efficiency and OSNR, respectively, versus SOA length, computed using the expressions derived in Appendix B. The following values were used for the relevant parameters: P_p^{in} (in-fiber input pump power) = +16 dBm, P_q^{in} (in-fiber input signal power) = +6 dBm, C (light coupling efficiency into and out of the SOA) = 40%, P_{sat} (SOA saturation power) = +12.8 dBm, Γ (confinement factor) = 0.1, Γg_0 (unsaturated modal gain coefficient) = 117 cm^{-1}, γ (scattering loss coefficient) = 10 cm^{-1}, Γg^M (modal gain coefficient at full inversion,

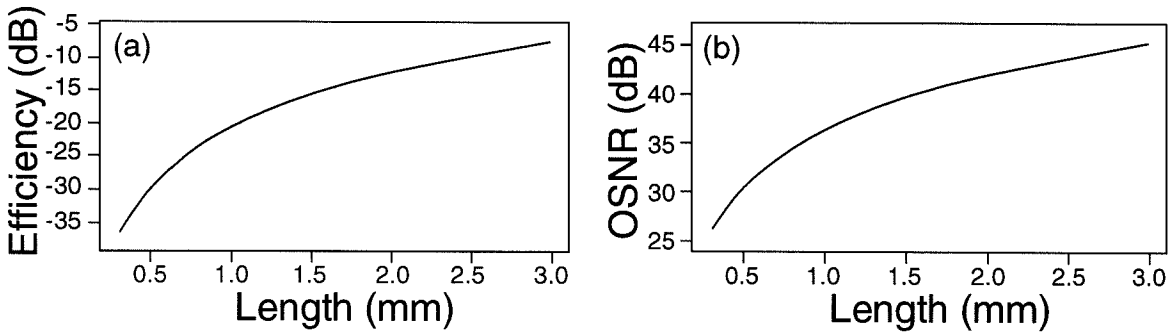

Figure 7.2: Theoretical conversion efficiency (a) and OSNR (b) of a wavelength converter based on FWM in a SOA, versus length of the active medium.

used to compute the ASE noise power as described in Appendix B) = 147 cm^{-1}; finally, the strength $|\chi(\Omega)|$ of the nonlinearity (which enters the relevant expressions as a multiplicative prefactor) was chosen arbitrarily (the same parameter values will be used in the next chapter to compare the present device with a wavelength converter based on self-pumped FWM in a semiconductor laser). The benefits resulting from using longer SOAs are apparent from these plots: for instance, we see that an increase in L from 0.5 to 2 mm causes an improvement of approximately 17 dB in conversion efficiency and 12 dB in OSNR.

Finally, it should be mentioned that the SOA gain profile is also important in determining the performance of the wavelength converter of Fig. 7.1. In particular, it is desirable that the gain coefficient be large and relatively flat near the wavelengths of the pump wave and the input signal; on the other hand, the gain at the converted signal wavelength should be small to minimize the ASE noise power in its spectral vicinity. Additional improvements can be achieved [23] by reducing the joint density

of states near the operating wavelength, to increase the inversion factor and hence decrease the SOA noise figure, and by positioning the bandgap wavelength near the operating wavelength, to increase the linewidth enhancement factor and hence the strength of the (index) nonlinearity.

7.3 Wide-Span Wavelength Conversion at 10 Gbit/sec

In this section, we present the system performance of the wavelength converter described above, with a relatively long (1.5 mm) SOA. In particular, in this experiment we used a fiber-pigtailed polarization-insensitive bulk optical amplifier; single-pass traveling-wave operation in this device is provided by coated angled facets [29], and its maximum fiber-to-fiber small-signal gain, at 1565 nm, is limited to approximately 24 dB by the ASE-induced gain saturation.

The experimental setup is shown in Fig. 7.3. A 10 Gbit/sec Hewlett-Packard bit-error-rate tester (BERT), consisting of a clock source, a pattern generator, a BER detector and a microwave transition analyzer (MTA), is used for signal generation, error detection and eye diagram analysis. The input signal is provided by an externally modulated laser source (a DFB laser in the downconversion experiment, a tunable external cavity diode laser in the upconversion experiment). In particular, we use a $LiNbO_3$ Mach-Zender modulator, driven by the BERT at 10 Gbit/sec with a nonreturn-to-zero $2^{31} - 1$ pseudorandom bit stream. To compensate for the losses in the modulator, the signal is passed through an EDFA (followed by a 1-nm BPF for ASE prefiltering) before being coupled into the wavelength converter.

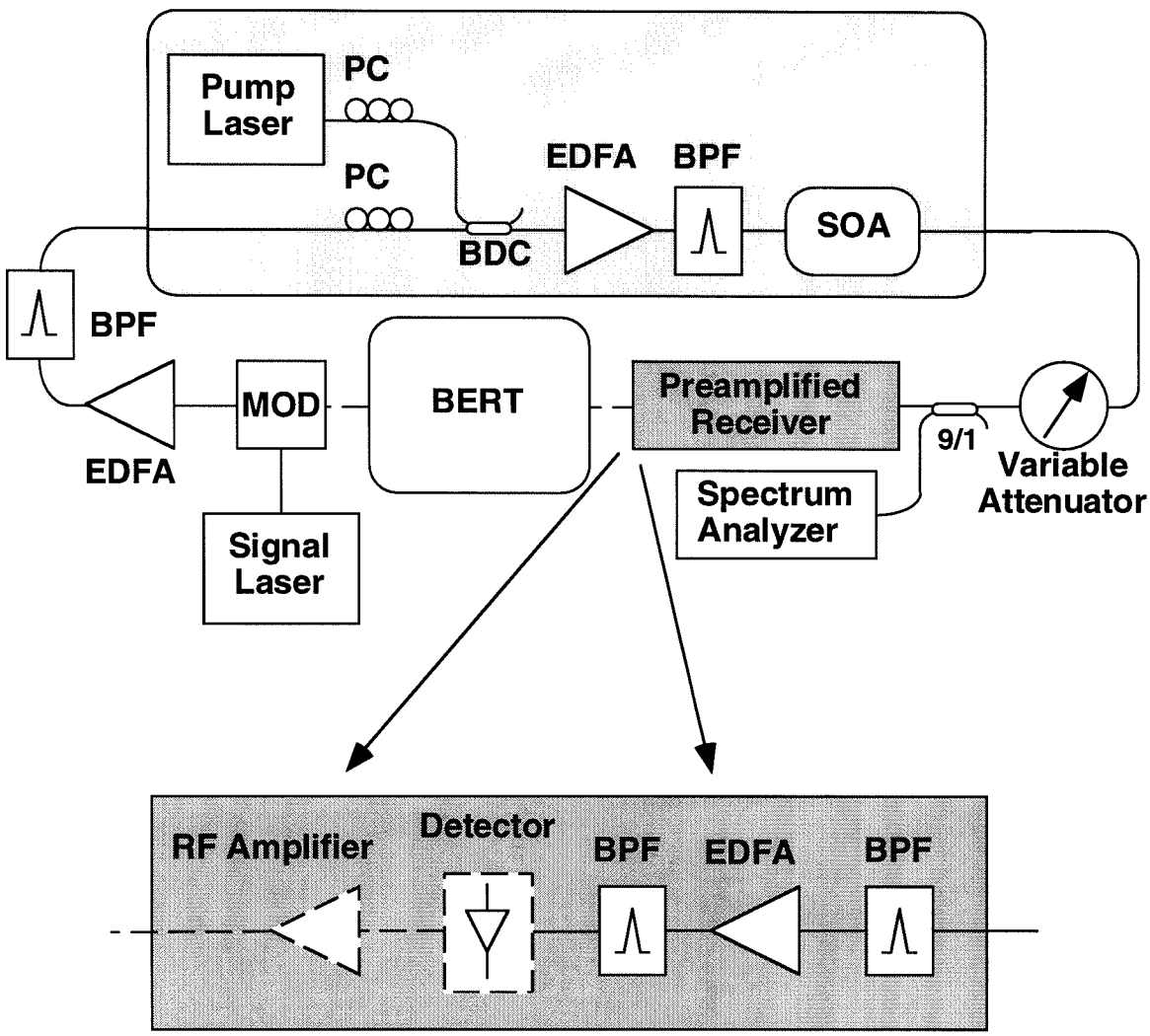

Figure 7.3: Experimental setup used to characterize the FWM wavelength converter system performance (all the acronyms are defined in the text).

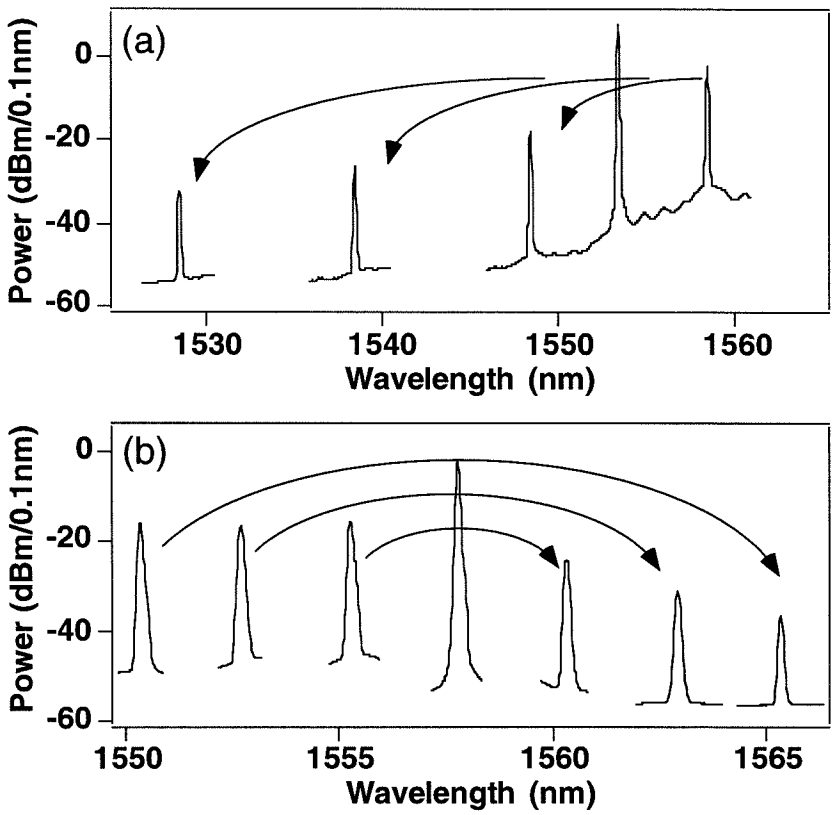

Figure 7.4: Optical spectra at the output of the SOA used in the FWM wavelength converter, for three different wavelength downshifts (a) up to 30 nm, and for three different upshifts (b) up to 15 nm.

At the output of the SOA, a variable attenuator and a tap (consisting of an optical spectrum analyzer with 0.2-nm resolution bandwidth) are used to measure the received power. The converted signal is then detected with a preamplified receiver consisting of a 1-nm BPF, a low-noise EDFA (with noise figure between 3 and 4.5 dB over the entire the Erbium gain bandwidth), another 1-nm BPF, a *p-i-n* receiver, and a 6-GHz bandwidth electrical amplifier. The electrical output finally reaches a 9:1 splitter with the 10% arm connected to the MTA for eye diagram analysis, and

the 90% arm connected to the BER detector.

In Fig. 7.4 we show slices of different output spectra of the SOA, for three different wavelength downshifts (Fig. 7.4a) up to 30 nm, and for three different wavelength upshifts (Fig. 7.4b) up to 15 nm. Due to the limited set of laser sources available in the lab, in the upconversion case we used a fixed pump wave and tuned the input signal wavelength instead (vice versa in the downconversion case). In all these traces, the OSNR of the FWM signal is larger than 20 dB, as required for error-free detection at 10 Gbit/sec in our setup. It is apparent from the figure that the device performs significantly better in the case of wavelength downconversion than for upconversion. This is mainly due to interference among the several physical mechanisms contributing to the FWM nonlinearity, as discussed in chapter 2 (see Fig. 2.4).

The BER vs received-power curves for the wavelength shifts of Figs. 7.4a and 7.4b are given in Figs. 7.5a and 7.5b, respectively (an eye diagram corresponding to the largest shift is also shown in each figure). We emphasize that the 30-nm downshift and the 15-nm upshift are the largest shifts reported to date for error-free wavelength conversion by FWM in SOAs. Because of the frequency dependence of our preamplified receiver performance, there is no single baseline against which we could compare all of these traces; instead, a different back-to-back BER vs received-power curve was measured at each FWM signal wavelength. From these measurements we found that the power penalty of all the downshifts is less than 1 dB; in fact, the maximum downshift measured (30 nm) was limited by the bandwidth of the ASE prefilters available in the lab (we did not have any BPF with pass-band larger than

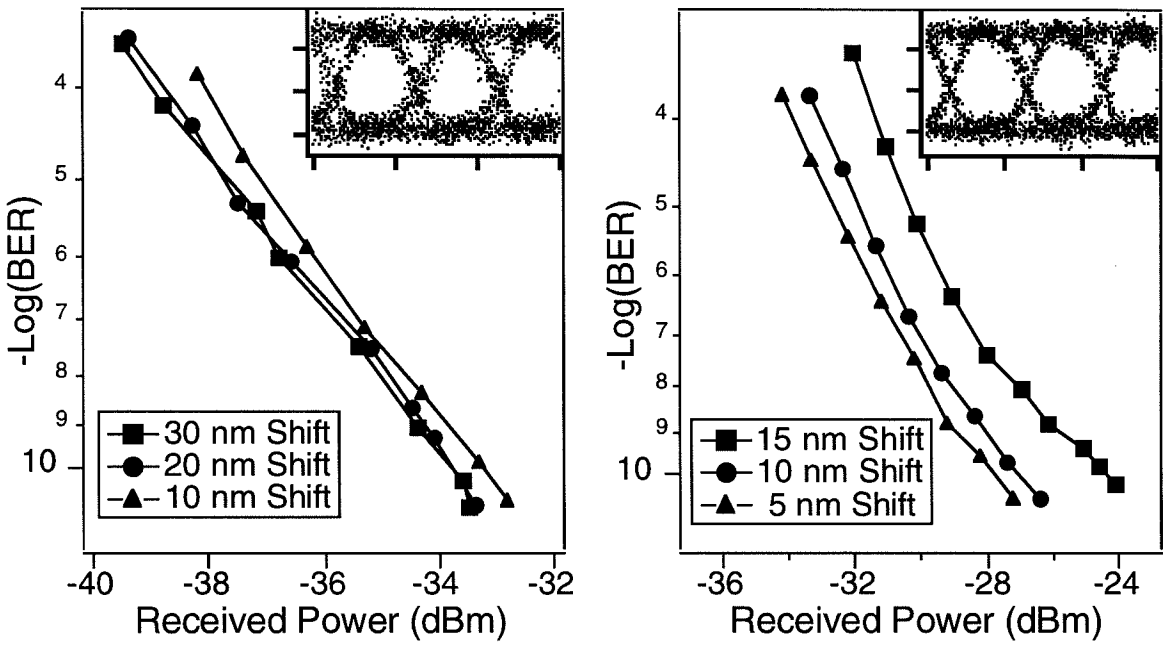

Figure 7.5: BER performance versus received power of the FWM wavelength conversion device (at 10 Gbit/sec), for the different wavelength downshifts (a) and upshifts (b) of Fig. 7.4. An error-free eye-diagram for the largest shift is also shown in each case.

15 nm).

On the other hand, the power penalty of the largest upshift (15 nm) was found to be approximately 4 dB (the corresponding BER curve also exhibits some flooring). In this case the main limiting factor is the OSNR of the FWM signal, and error-free operation becomes unpractical at larger wavelength upshifts. However, it should be mentioned that the gain profile of the present device is not particularly well suited to these wavelength upconversions, in which the FWM signal is generated near the SOA gain peak, where the ASE noise power is maximum. Therefore, using a different

pump wavelength (which was not possible at the time due to our limited choice of laser sources) could lead to even larger wavelength upshifts with this same device (and of course further improvements could be obtained with longer SOAs).

7.4 Polarization Insensitive Wavelength Conversion

As discussed in the introduction, a significant limitation of the wavelength conversion device described here is the polarization dependence of its conversion efficiency. Standard single-mode fibers used in most telecommunication networks are not polarization maintaining; in fact, as light signals travel in these waveguides, their polarization state is scrambled in a random fashion, varying with mechanical stress, temperature, etc. As a result, it is important that all components used in fiber-optic networks be polarization insensitive.

In order to see whether it is possible to make the FWM efficiency independent of the polarization state of the input signal, we use the results of chapter 3 regarding the polarization properties of FWM. From the general expression of Eq. 3.9 for the FWM signal vector field, the conversion efficiency $\eta \propto |E_s(L)|^2/|E_q(0)|^2$ can be written as

$$\eta(\hat{q}) = \left(|Aq_1|^2 + |Bq_2|^2 + Re\left[Cq_1^* q_2\right]\right)|E_p(0)|^4 \tag{7.2}$$

where $\hat{p}E_p(0)$ and $\hat{q}E_q(0)$ denote the vector fields of the pump wave and the input signal respectively at the input of the SOA ($\hat{p}$ and $\hat{q}$ are polarization unit vectors perpendicular to the waveguide axis, with the subscripts 1 and 2 denoting their TE and TM components respectively). Furthermore, we defined a set of complex-valued coefficients A, B and C, that depend only on $\hat{p}$ and on the tensor M_{ijkl} of Eq. 3.9

(which is determined by the material, structural and operational properties of the SOA). Explicit expressions for these coefficients can be immediately derived by taking the magnitude squared of Eq. 3.9 and comparing the result with Eq. 7.2.

Given the unit-vector normalization condition $|q_1|^2 + |q_2|^2 = 1$, we find from Eq. 7.2 that the following three conditions [24] must be simultaneously satisfied in order to make the FWM conversion efficiency η independent of the polarization state $\hat{q}$ of the input signal:

$$|A| = |B|$$

$$Re\,[C] = 0$$

$$Im\,[C] = 0. \tag{7.3}$$

An important result of this analysis is that, in general, given an arbitrary SOA with its "transfer tensor" M_{ijkl}, it is not possible to obtain polarization independent FWM by simply selecting a proper polarization state for the input pump wave. The reason is that the polarization unit vector $\hat{p}$ is completely specified by two real variables (the magnitude of either component and the relative phase between them), while, as we just showed, polarization independent FWM requires that three equations be simultaneously satisfied. In fact, mathematically there exists a set of tensors M_{ijkl} for which the three conditions of Eq. (7.3) admit a same solution for $\hat{p}$, and ways of designing SOAs with transfer tensors belonging to such a set have been considered theoretically [24], [30]. However, their practical implementation is still a subject of investigation.

An easier approach consists of using two nondegenerate pump waves of frequencies

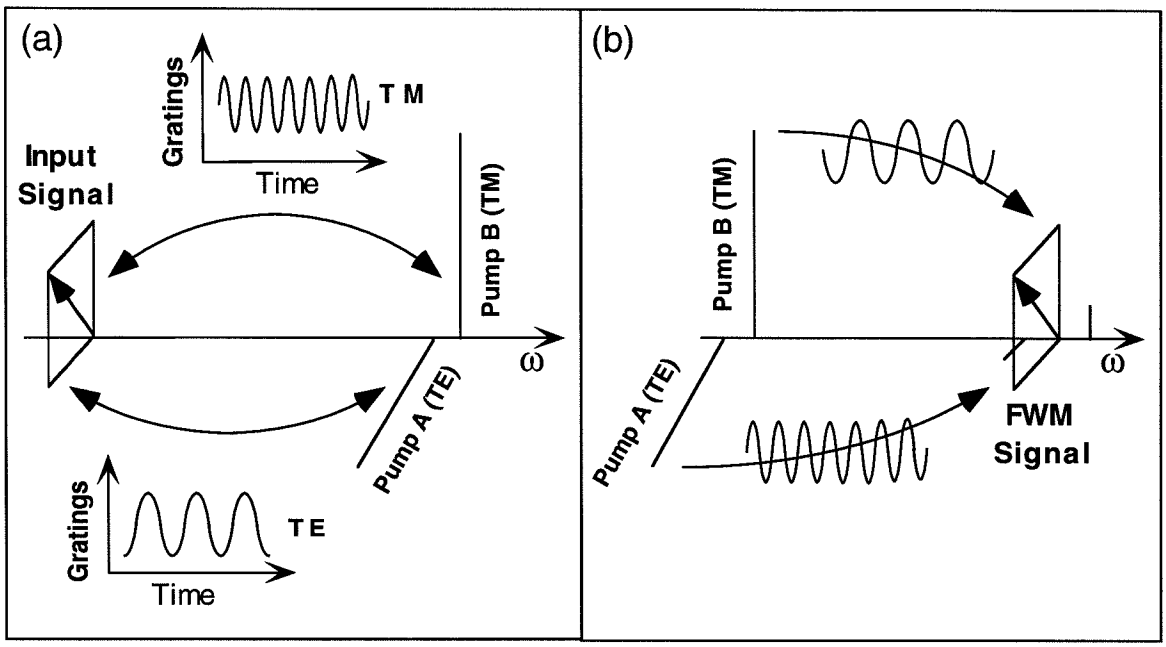

Figure 7.6: Schematics of the FWM processes taking place with two orthogonally polarized (TE and TM) pump waves closely spaced in frequency. As shown in (b), in this case only one "type" of gratings contribute to the formation of each component of the converted signal; as a result, the FWM efficiency is polarization insensitive.

ω_p^A and ω_p^B and detecting the FWM signal at frequency $\omega_p^A + \omega_p^B - \omega_q$. In this case, it is easy to show that the general expression (7.2) for the conversion efficiency, and hence the conditions (7.3) for polarization independent FWM, remain valid. However, the coefficients A, B, and C now depend on the polarization unit vectors of both pump waves, which are specified by a total of four independent variables. Therefore, regardless of the details of the SOA (i.e., for most practical transfer tensors M_{ijkl}), in general there will be a choice for the polarization states of the two pump waves that results in a polarization independent FWM efficiency.

In fact, based on the physical argument illustrated schematically in Fig. 7.6, we can show that the required dual-pump polarization configuration is simply given, to a good degree of approximation, by a TE and a TM pump wave closely spaced in frequency. Figure 7.6a shows the formation of the dynamic gain and index gratings in this case, which, as usual, only involves beating of equal polarization components. In particular, in this figure the "TE-induced (TM-induced) gratings" are formed by the beating of the TE (TM) component of the input signal with pump A (B). Notice that since the two pump waves are nondegenerate, the two types of gratings have slightly different frequencies (the TM-induced gratings are faster in the case shown).

The scattering of the pump waves by these gratings generates three FWM signals, as shown in Fig. 7.6b. In particular, the middle one, at frequency $\omega_p^A + \omega_p^B - \omega_q$, involves both pump waves and it is nearly polarization independent. The key feature is that each component of this FWM signal (say the TE component) is generated by scattering of the equally-polarized pump wave (pump A) by one type of gratings *only* (the TM-induced gratings, since scattering of pump A by the TE-induced gratings contributes to the FWM signal of frequency $2\omega_p^A - \omega_q$). Therefore, there is no longer interference between the two types of gratings in the generation of the FWM signal, which, as we argued in section 3.4, is the main cause of polarization dependence.

It is important to point out that the frequency separation between the two pump waves is critical. In particular, for maximum polarization insensitivity, this should be much smaller than the separation between either pump wave and the input signal, so that the TE-induced gratings and the TM-induced gratings are generated with

nearly equal efficiency (recall that the detuning frequency dependence of the FWM efficiency mainly arises from the gratings formation process). Otherwise if, say, the TE pump wave is much closer in frequency to the input signal, the resulting conversion efficiency will be stronger for a TE input signal. On the other hand, a lower limit to the minimum frequency spacing between the pump waves is set by the pass-band of the BPF used to separate the polarization insensitive FWM signal from the adjacent single-pump FWM products (which are strongly polarization dependent).

In the following we demonstrate this approach using an alternating-strain multi-quantum-well SOA (780 μm long) having polarization independent optical gain [31] (the same device used in the experiments described in chapters 4 and 6). Incidentally, this approach requires a relatively isotropic device, because any anisotropy in the propagation properties of the SOA waveguide results in additional polarization dependence of all three FWM signals. Furthermore, in a perfectly isotropic SOA any pair of orthogonal polarization states for the two pump waves (not just TE and TM) is appropriate. In fact, the use of a dual-pump configuration to obtain polarization insensitive FWM has been originally demonstrated in bulk SOAs and optical fibers [32], [33].

The setup used in this experiment is the same as that shown in Fig. 7.3, except that two pump sources are required in this case, and furthermore the input signal was provided by a directly modulated DFB laser. The input signal and both pump waves are amplified with a same EDFA: as a result (given that the EDFA output power is fixed) the use of two pump waves automatically results in a 6-dB degradation in FWM

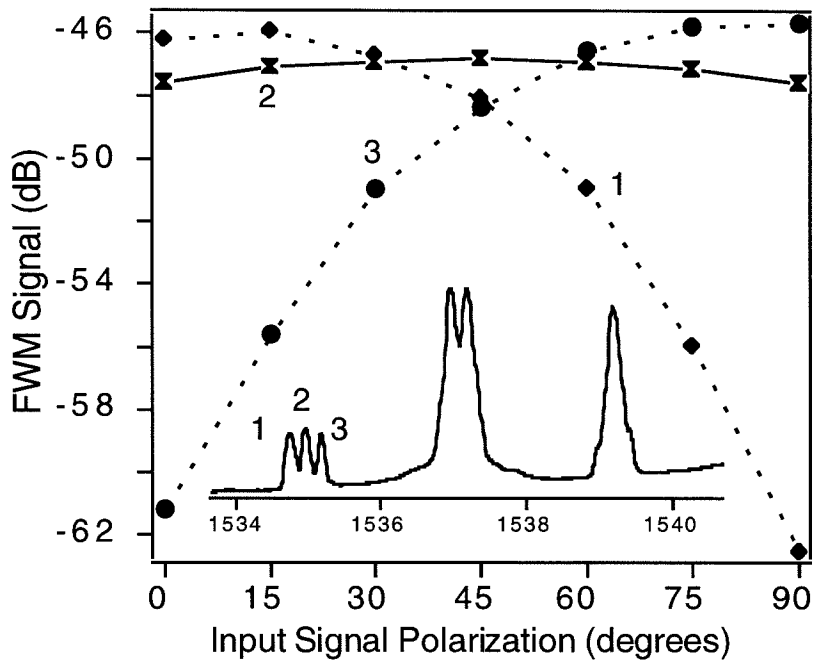

Figure 7.7: Measured intensity of the three FWM signals at the output of the SOA with two orthogonal (TE and TM) pump waves, for different states of linear polarization of the input signal. The inset shows the SOA output spectrum with input signal linearly polarized at 45° relative to the TM axis.

conversion efficiency and OSNR. The frequency separation between the two pump waves was set to 0.2 nm, and a 0.5-nm wide BPF was used at the SOA output (the residual polarization dependence of the FWM signal was found to be very sensitive to the center frequency of this filter).

In Fig. 7.7 we plot the measured intensity of all three FWM signals for different states of linear polarization of the input signal (the horizontal axis gives the angle θ between the input polarization unit vector of the input signal and the SOA growth axis). The optical spectrum at the output of the SOA for a wavelength downshift

of 6 nm and $\theta = 45°$ is also shown in the inset. The middle FWM signal (labeled 2 in the figure) is found to vary by less than 1.5 dB for all linear polarizations of the input signal; this remains the case for arbitrary elliptical polarizations. In contrast, the two single-pump FWM peaks vary by more than 15 dB.

We also repeated this measurement for different sets of orthogonal pump polarizations. We found that the polarization dependence of the FWM signal of interest increased relative to the TE-TM case, but not by a large amount (the largest measured variation was 3.5 dB for two linearly polarized pump waves at $+60°$ and $-30°$ relative to the growth axis). This is a consequence of the finite but weak anisotropy of the SOA waveguide used in this experiment.

Figure 7.8 shows the BER vs. received-power traces for the same set of input signal polarizations of Fig. 7.7. The wavelength shift is 4 nm in this case (similar results were found for different shifts) and the bit rate is 2.5 Gbit/sec. The polarization dependence of the power penalty is found to be small enough (< 2 dB) to qualify this device as a polarization insensitive wavelength converter.

Finally, we emphasize that the performance of the present device, in terms of bit rate and wavelength span, is limited by several factors, most of which are completely unrelated to the dual-pump configuration; these include the relatively short, non-fiber-pigtailed SOA, the limited stability of one of the pump sources (a tunable Erbium-doped fiber ring laser built in our labs), and the use of a directly modulated input signal (at the time of this experiment we did not have an external modulator). In fact, despite its intrinsic 6-dB degradation in FWM efficiency and OSNR and its added

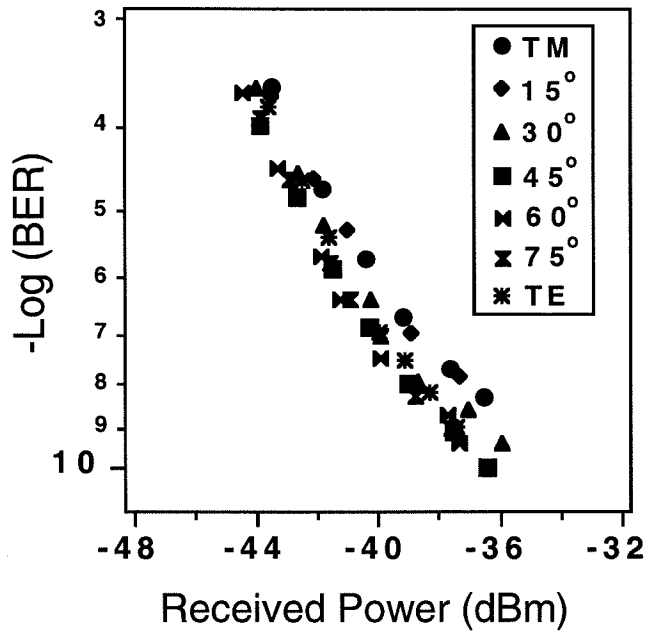

Figure 7.8: BER versus received power for a 4-nm wavelength downshift at 2.5 Gbit/sec, with two orthogonal (TE and TM) nearly degenerate pump waves, for different states of linear polarization of the input signal.

complexity, this approach (with all the above factors properly optimized) can be regarded as a practical technique for polarization insensitive wavelength conversion. Indeed, recently it has been succesfully demonstrated up to 10 Gbit/sec [34].

Bibliography

[1] C. A. Brackett, A. S. Acampora, J. Sweitzer, G. Tangonan, M. T. Smith, W. Lennon, K. C. Wang, and R. H. Hobbs, "A scalable multiwavelength multihop optical network: a proposal for research on all-optical networks," *J. Lightwave Technol.*, vol. 11, pp. 736–753, 1993.

[2] M. Kovačević and A. Acampora, "Benefits of wavelength translation in all-optical clear-channel networks," *IEEE J. Select. Areas Commun.*, vol. 14, pp. 868–880, 1996.

[3] R. A. Barry and Pierre A. Humblet, "Models of blocking probability in all-optical networks with and without wavelength changers," *IEEE J. Select. Areas Commun.*, vol. 14, pp. 858–867, 1996.

[4] S. J. B. Yoo, "Wavelength conversion technologies for WDM network applications," *J. Lightwave Technol.*, vol. 14, pp. 955–966, 1996.

[5] G. Raybon, U. Koren, B. I. Miller, M. Chien, K. Dreyer, S. Chandrasekhar, R. E. Behringer, R. E. Tennant, and K. Feder, "Reconfigurable optoelectronic wavelength translation based on an integrated electroabsorption modulated laser array," *IEEE Photon. Technol. Lett.*, vol. 10, pp. 215–217, 1998.

[6] J. M. Wiesenfeld, J. S. Perino, A. H. Gnauck, and B. Glance, "Bit error rate performance for wavelength conversion at 20 Gbit/s," *Electron. Lett.*, vol. 30, pp. 720–721, 1994.

[7] D. D. Marcenac, A. E. Kelly, D. Nesset, and D. A. O. Davies, "Bandwidth enhancement of wavelength conversion via cross-gain modulation by semiconductor optical amplifier cascade," *Electron. Lett.*, vol. 31, pp. 1442–1443, 1995.

[8] T. Durhuus, C. Joergensen, B. Mikkelsen, R. J. S. Pedersen, and K. E. Stubkjaer, "All optical wavelength conversion by SOA's in a Mach-Zender configuration," *IEEE Photon. Technol. Lett.*, vol. 6, pp. 53–55, 1994.

[9] X. Pan, J. M. Wiesenfeld, J. S. Perino, T. L. Koch, G. Raybon, U. Koren, M. Chien, M. Young, B. I. Miller, and C. A. Burrus, "Dynamic operation of a three-port, integrated Mach-Zender wavelength converter," *IEEE Photon. Technol. Lett.*, vol. 7, pp. 995–997, 1995.

[10] C. Joergensen, S. L. Danielsen, K. E. Stubkjaer, M. Schilling, K. Daub, P. Doussiere, F. Pommerau, P. B. Hansen, H. N. Poulsen, A. Kloch, M. Vaa, B. Mikkelsen, E. Lach, G. Laube, W. Idler, and K. Wunstel, "All optical wavelength conversion at bit rates above 10 Gb/s using semiconductor optical amplifiers," *IEEE J. Select. Topics Quantum Electron.*, vol. 3, pp. 1168–1180, 1997.

[11] M. C. Tatham, G. Sherlock, and L. D. Westbrook, "20-nm optical wavelength conversion using nondegenerate four-wave mixing," *IEEE Photon. Technol. Lett.*, vol. 5, pp. 1303–1306, 1993.

[12] J. Zhou, N. Park, J. W. Dawson, K. J. Vahala, M. A. Newkirk, and B. I. Miller, "Efficiency of broadband four-wave mixing wavelength conversion using semiconductor traveling-wave amplifiers," *IEEE Photon. Technol. Lett.*, vol. 6, pp. 50–52, 1994.

[13] D. F. Geraghty, R. B. Lee, M. Verdiell, M. Ziari, A. Mathur, and K. J. Vahala, "Wavelength conversion for WDM communication systems using four-wave mixing in semiconductor optical amplifiers," *IEEE J. Select. Topics Quantum Electron.*, vol. 3, pp. 1146–1155, 1997.

[14] A. D'Ottavi, F. Girardin, L. Graziani, F. Martelli, P. Spano, A. Mecozzi, S. Scotti, R. Dall'Ara, J. Eckner, and G. Guekos, "Four-wave mixing in semiconductor optical amplifiers: a practical tool for wavelength conversion," *IEEE J. Select. Topics Quantum Electron.*, vol. 3, pp. 522–528, 1997.

[15] K. Inoue, "Wavelength conversion experiment using fiber four-wave mixing," *IEEE Photon. Technol. Lett.*, vol. 4, pp. 69–72, 1992.

[16] C. Q. Xu, H. Okayama, K. Shinozaki, K. Watanabe, and M. Kawahara, "Wavelength conversions near 1.5 μm by difference frequency generation in periodi-

cally domain-inverted $LiNbO_3$ channel waveguides," *Appl. Phys. Lett.*, vol. 63, pp. 1170–1172, 1993.

[17] S. J. B. Yoo, C. Caneau, R. Bhat, M. A. Koza, A. Rajhel, and N. Antoniades, "Wavelength conversion by difference-frequency-generation in AlGaAs wave guides with periodic domain inversion achieved by wafer bonding," *Appl. Phys. Lett.*, vol. 68, pp. 2609–2611, 1996.

[18] J. P. R. Lacey, S. J. Madden, M. A. Summerfield, R. S. Tucker, and A. I. Faris, "Four-channel WDM optical phase conjugator using four-wave mixing in a single semiconductor optical amplifier," *Electron. Lett.*, vol. 31, pp. 743–745, 1995.

[19] D. Nesset, D. D. Marcenac, P. L. Mason, A. E. Kelly, S. Bouchoule, and E. Lach, "Simultaneous wavelength conversion of two 40 Gbit/s channels using four-wave mixing in a semiconductor optical amplifier," *Electron. Lett.*, vol. 34, pp. 107–108, 1998.

[20] M. C. Tatham, X. Gu, L. D. Westbrook, G. Sherlock, and D. M. Spirit, "Transmission of 10 Gbit/s directly modulated DFB signals over 200 km standard fibre using mid-span spectral inversion," *Electron. Lett.*, vol. 30, pp. 1335–1336, 1994.

[21] D. D. Marcenac, D. Nesset, A. E. Kelly, M. Brierly, A. D. Ellis, D. G. Moodie, and C. W. Ford, "40 Gbit/s transmission over 406 km of NDSF using mid-span spectral inversion in a 2 mm long semiconductor optical amplifier," *Electron. Lett.*, vol. 33, pp. 879–881, 1997.

[22] G. Hunziker, R. Paiella, A. D'Ottavi, P. Spano, R. Dall'Ara, G. Guekos, and K. J. Vahala, "30 nm Wavelength Conversion at 10 Gb/s by Four-Wave Mixing in a Semiconductor Optical Amplifier," presented at the *Optical Fiber Communication Conference*, San Jose, California, 1998, paper WB7.

[23] A. E. Kelly, D. D. Marcenac, and D. Nesset, "40 Gbit/s wavelength conversion over 24.6 nm using FWM in a semiconductor optical amplifier with an optimised MQW active region," *Electron. Lett.*, vol. 33, pp. 2123–2124, 1997.

[24] R. Paiella, G. Hunziker, J. Zhou, K. J. Vahala, U. Koren, and B. I. Miller, "Polarization Properties of Four-Wave Mixing in Strained Semiconductor Optical Amplifiers," *IEEE Photon. Technol. Lett.*, vol. 8, pp. 773–775, 1996.

[25] G. Hunziker, R. Paiella, D. F. Geraghty, K. J. Vahala, and U. Koren, "Polarization-Independent Wavelength Conversion at 2.5 Gb/s by Dual-Pump Four-Wave Mixing in a Strained Semiconductor Optical Amplifier," *IEEE Photon. Technol. Lett.*, vol. 8, pp. 1633–1635, 1996.

[26] J. Zhou and K. J. Vahala, "Noise reduction in FWM wavelength converters," *Conference on Lasers and Electro-Optics 1995*, Baltimore, Maryland, paper CThT1.

[27] M. A. Summerfield, and R. S. Tucker, "Optimization of pump and signal powers for wavelength converters based on four-wave mixing in semiconductor optical amplifiers," *IEEE Photon. Technol. Lett.*, vol. 8, pp. 1316–1318, 1996.

[28] K. L. Hall, G. Lenz, and E. P. Ippen, "Femtosecond time domain measurements of group velocity dispersion in diode lasers at 1.5 μm," *J. Lightwave Technol.*, vol. 10, pp. 616–619, 1992.

[29] C. Holtman, P. A. Besse, T. Brenner, and H. Melchior, "Polarization independent bulk active region semiconductor optical amplifiers for 1.3 μm wavelengths," *IEEE Photon. Technol. Lett.*, vol. 8, pp. 343–345, 1996.

[30] K. Ovsthus and V. Khalfin, "A novel method for polarization-insensitive four-wave mixing in semiconductor optical amplifiers," *IEEE Photon. Technol. Lett.*, vol. 8, pp. 527–529, 1996.

[31] M. A. Newkirk, B. I. Miller, U. Koren, M. G. Young, M. Chien, R. M. Jopson, and C. A. Burrus, "1.5 μm multiquantum-well semiconductor optical amplifier with tensile and compressively strained wells for polarization-independent gain," *IEEE Photon. Technol. Lett.*, vol. 4, pp. 406–408, 1993.

[32] R. M. Jopson and R. E. Tench, "Polarization independent phase conjugation of lightwave signals," *Electron. Lett.*, vol. 29, pp. 2216–2217, 1993.

[33] K. Inoue, "Polarization independent wavelength conversion using fiber four-wave mixing with two orthogonal pump lights of different frequencies," *J. Lightwave Technol.*, vol. 12, pp. 1916–1920, 1994.

[34] L. Y. Lin, J. M. Wiesenfeld, J. S. Perino, and A. H. Gnauck, "Polarization-insensitive wavelength conversion up to 10 Gb/s based on four-wave mixing in

a semiconductor optical amplifier," *IEEE Photon. Technol. Lett.*, vol. 10, pp. 955-957, 1998.

Chapter 8

Wavelength Conversion by FWM in Semiconductor Lasers with a Bragg Mirror

8.1 Introduction

In the previous chapter, we described in details a wavelength conversion device based on FWM in single-pass SOAs [1]–[5]. As discussed there, impressive results in the performance of this device have been recently demonstrated [4], [5] using high-power input waves and long SOAs. An extension of this design strategy consists of placing the nonlinear active medium in an optical cavity. In the following, we describe and demonstrate two different FWM configurations that take advantage of the optical feedback in a semiconductor laser. In one case [6], the laser is biased above threshold and the lasing beam is used as the FWM pump wave, so that a large pump power

is obtained with significantly reduced device complexity (i.e., with no need for an external pump source and for an EDFA at the SOA input). Furthermore [7], the lasing action is beneficial to the wavelength conversion process because of the resulting clamping of the optical gain (and hence of the FWM nonlinearity). In a second configuration [8], we use an external pump wave (strong enough to quench any solitary laser oscillation) and tune the frequency of the converted signal to the laser frequency; consequently, the device is injection locked by the FWM signal itself, leading to a large resonance enhancement of both conversion efficiency and OSNR.

Both approaches would be cumbersome to implement with a Fabry-Perot cavity, because of the complications arising from the laser being injection locked by the external input wave(s). In order to avoid such complications, it is convenient to use a resonator with a narrowband wavelength-selective reflector, such as a Bragg mirror, with the external input wave(s) sufficiently detuned from its reflection band so that for such wave(s) the device simply acts as a SOA. Here, we present experimental results obtained from a semiconductor laser with a fiber Bragg grating (FBG) pigtailed to one facet, and a high-reflection coating on the other facet. This structure has the advantage that there is no spatial overlap between the nonlinear medium and the Bragg mirror, which may introduce a significant phase mismatch in the FWM interaction. It should be mentioned, however, that self-pumped FWM has also been recently demontrated with good results in long, quarter-wave shifted distributed feedback (DFB) lasers [9]. In both cases, the center wavelength of the Bragg mirror reflection bandwidth is not tunable, so that the pump wavelength (in

the self-pumped configuration) and the destination wavelength of the converted signal (in the injection-locked configuration) are fixed. However, an electrically-tunable, on-chip distributed Bragg reflector (DBR) could be used to overcome this problem (DBR lasers are also promising for additional reasons, as will be discussed below).

The chapter is organized as follows. We begin, in the next section, with a description of the FBG coupled laser used in this work, and of the general features of the FWM interaction in this device. In section 8.3 we discuss wavelength conversion by self-pumped FWM, and present the measured BER performance of this converter at 2.5 Gbit/sec. An important feature of this configuration is the fact that, due to gain clamping, both the conversion efficiency and the OSNR of the converted signal exhibit a strong, nearly quadratic, dependence on the pump power; this property is experimentally verified in section 8.3.2, where we also discuss its implications to the design of self-pumped FWM converters. Finally, section 8.4 is devoted to a wavelength converter based on injection-locked FWM; in particular, we present a detailed characterization of its static response, together with preliminary dynamic results at 1 Gbit/sec. With the present laser, this approach cannot be extended to signals with higher bit rate due to the narrow width of the injection-locking resonances; however, we show theoretically how the maximum bit rate can be improved by proper design of the laser cavity. Furthermore, we discuss how the frequency selectivity of this wavelength converter can become an advantage in some applications.

8.2 FWM in a Fiber-Bragg-Grating Coupled Semiconductor Laser

A schematic picture of the device used in these experiments is given in Figs. 8.1 and 8.5 below (for the self-pumped and the injection-locked FWM configurations, respectively). The laser consists of a semiconductor active region with a high-reflection coating on the back facet (providing almost unit reflectivity), and a FBG (with narrow reflection bandwidth centered at about 1554 nm) butt-coupled to the front facet (which is anti-reflection coated). The active region is 500-μm-long, and it is based on a compressively strained MQW structure. We point out that the present device characteristics were optimized for single-mode laser oscillation. Also shown in the figures is an optical circulator, used for efficient coupling of light in and out of the laser (although in the self-pumped FWM experiment a bidirectional coupler was used instead).

The generation and propagation of the FWM signal in this device can be described in the same way as for the case of single-pass SOAs (as in Appendix B), except that here one has to consider waves traveling in both directions along the waveguide axis (and the boundary conditions are different). In this section, we will briefly outline the theoretical description of FWM in a FBG coupled laser, irrespective of the specific configuration considered (i.e., of whether the pump wave is generated inside the laser or is externally injected). This description will then be used in the following sections to discuss how the wavelength conversion performance of this device can be improved by proper design of the laser structure.

Under the experimental conditions of interest here, the total electric field in the laser waveguide (averaged over the transverse dimensions) can be written as

$$\mathcal{E}(z,t) = \sum_{f=p,q,s} \left(E_f^+(z) e^{ik_f z} + E_f^-(z) e^{-ik_f z} \right) e^{-i\omega_f t} + c.c. \tag{8.1}$$

where as before ω_p, $\omega_q = \omega_p - \Omega$, and $\omega_s = \omega_p + \Omega$ are the frequencies of the pump wave, the input signal, and the converted signal respectively (here we are assuming that the pump wave is significantly stronger than the input signal so that the FWM sideband of frequency $\omega_s' = \omega_q - \Omega$ is negligible). Furthermore, in Eq. (8.1) we defined $k_f = \omega_f \bar{n}/c$, where $\bar{n}$ is the modal index of refraction. Notice that we are assuming copolarized input waves (along the TE axis of the compressively strained SOA), so that a "scalar" notation is appropriate in this analysis.

The different field amplitudes $E_f^{\pm}$ defined above satisfy the following coupled-mode wave equations (same as Eqs. (B.3) and (B.4))

$$\pm \frac{dE_{p,q}^{\pm}(z)}{dz} = \left\{ \Gamma \left(\frac{1}{2}\, g(P_{tot}(z)) - i\, \delta k(P_{tot}(z)) \right) - \frac{1}{2}\gamma \right\} E_{p,q}^{\pm}(z), \tag{8.2}$$

$$\pm \frac{dE_s^{\pm}(z)}{dz} = \left\{ \Gamma \left(\frac{1}{2}\, g(P_{tot}(z)) - i\, \delta k(P_{tot}(z)) \right) - \frac{1}{2}\gamma \right\} E_s^{\pm}(z) + \\ + \Gamma \kappa(P_{tot}(z);\Omega) \left(E_p^{\pm}(z) \right)^2 \left(E_q^{\pm}(z) \right)^* \tag{8.3}$$

where Γ is the confinement factor, g is the material gain coefficient, $-\delta k$ is the carrier-induced phase shift per unit length, γ is the waveguide scattering loss coefficient, κ is the FWM coupling coefficient, and P_{tot} is the total optical power along the axis of the active region. Notice that we are neglecting in Eq. (8.3) any contribution to the FWM signal arising from mixing of counterpropagating field components, because these contributions are strongly phase-mismatched. Vice versa, the contributions

from copropagating waves are taken to be perfectly phase matched, and furthermore we neglect the wavelength dependence of g and δk. These assumptions are perfectly justified over a wide range of wavelength shifts of interest (say $|\Delta\lambda| \equiv |\lambda_q - \lambda_s| \sim 2-30$ nm).

Equations (8.2) and (8.3) are to be solved in conjunction with a set of boundary conditions having the general form (for $f : p, q, s$)

$$E_f^+(0) = C\sqrt{R_{BG}(\omega_f)}e^{i\omega_f l_{BG}(\omega_f)/c}E_f^-(0) \; + \; \sqrt{C}E_f^{in},$$

$$E_f^-(L) = \sqrt{R_{HC}}E_f^+(L) \tag{8.4}$$

where $z = 0$ and $z = L$ denote the anti- and the high-reflection coated facets of the laser respectively, C is the fraction of optical power that is coupled from the fiber into the laser (and vice versa), R_{BG} and R_{HC} are the power reflectivities of the FBG mirror and of the high-reflection coating respectively (the former being a narrowband function of frequency peaked at around 1554 nm), l_{BG} is the optical path length from the anti-reflection coated facet into the FBG and back to the same facet, and E_f^{in} is the external field at ω_f launched past the FBG.

The solution of the boundary-value problem above requires knowledge of the dependence of the coefficients appearing in Eqs. (8.2) and (8.3) on the total power $P_{tot}(z)$. Such a dependence is described in Appendix B, but it will be reviewed in the following for completeness, and cast in a slightly different notation, more appropriate to the FBG diode laser.

As for the gain coefficient g, it is convenient to write it as

$$g(P_{tot}) = \frac{g_{th}}{\Gamma} + A\,\Delta N(P_{tot}) \tag{8.5}$$

where

$$g_{th} = \gamma + \frac{1}{L}\log(\frac{1}{C\sqrt{R_{BG}R_{HC}}}) \tag{8.6}$$

is the modal gain coefficient at threshold (equal to the distributed loss coefficient), A is the differential gain, and R_{BG} is evaluated at the lasing frequency at threshold. Furthermore, ΔN is the local deviation of the steady-state carrier density from its threshold value, given by (from solution of the carrier density rate equation in steady-state)

$$\Delta N(P_{tot}) = \frac{(I - I_{th})/(qV_a) - g_{th}P_{tot}/(\Gamma\hbar\omega S_m)}{1/\tau_{sp} + AP_{tot}/(\hbar\omega S_m)} \tag{8.7}$$

where I is the laser bias current, V_a is the volume of the active region, S_m is the modal cross-sectional area, and τ_{sp} is the spontaneous and nonradiative recombination lifetime. A similar functional dependence on P_{tot} can be assumed for δk, which anyway cancels out in the results of the following sections.

Finally, the nonlinear coupling coefficient κ depends on the optical power through the gain coefficient, its derivatives with respect to carrier density and temperature, and the corresponding linewidth enhancement factors. An expression for $\kappa(P_{tot};\Omega)$ can be derived from the microscopic theory of FWM in semiconductor gain media discussed in chapter 3 and Appendix A; furthermore, it has been modeled with varying degrees of approximation [10]–[12]. A simple model that is often used and that is a valid approximation over a wide range of conditions is based on the expression

$$\kappa(P_{tot};\Omega) = \kappa_0(\Omega)g(P_{tot}) \tag{8.8}$$

where the function $\kappa_0(\Omega)$ describes the decrease in the strength of the FWM nonlinearity with increasing detuning frequency.

To conclude this discussion, we point out that, since the pump wave is commonly much stronger than the input and the converted signals, it is a valid assumption to take

$$P_{tot}(z) \approx \left|E_p^+(z)\right|^2 + \left|E_p^-(z)\right|^2. \tag{8.9}$$

Then, $P_{tot}(z)$ can be obtained from a simple numerical integration of the boundary-value problem for the pump wave alone. An important simplification that follows from this assumption is that the carrier density is saturated by the (cw) pump wave alone. And as a result, even in the presence of an intensity-modulated input signal, the coefficients g, δk, and κ of Eqs. (8.2)-(8.3) remain approximately constant in time. The results obtained from this analysis, which is inherently steady-state, can then be taken to be approximately valid even in the presence of such a modulated signal (i.e., under the practical conditions of a wavelength conversion experiment).

8.3 Wavelength Conversion by Folded-Path Self-Pumped FWM

8.3.1 Wavelength Conversion Performance

In this section, we will discuss wavelength conversion by self-pumped FWM in a FBG coupled diode laser. As illustrated schematically in Fig. 8.1, in this configuration the laser is biased above threshold, and the FWM pump wave is provided by the lasing beam, so that this wavelength converter does not require a high-power external pump source. On the other hand, the input signal and, consequently, the converted signal

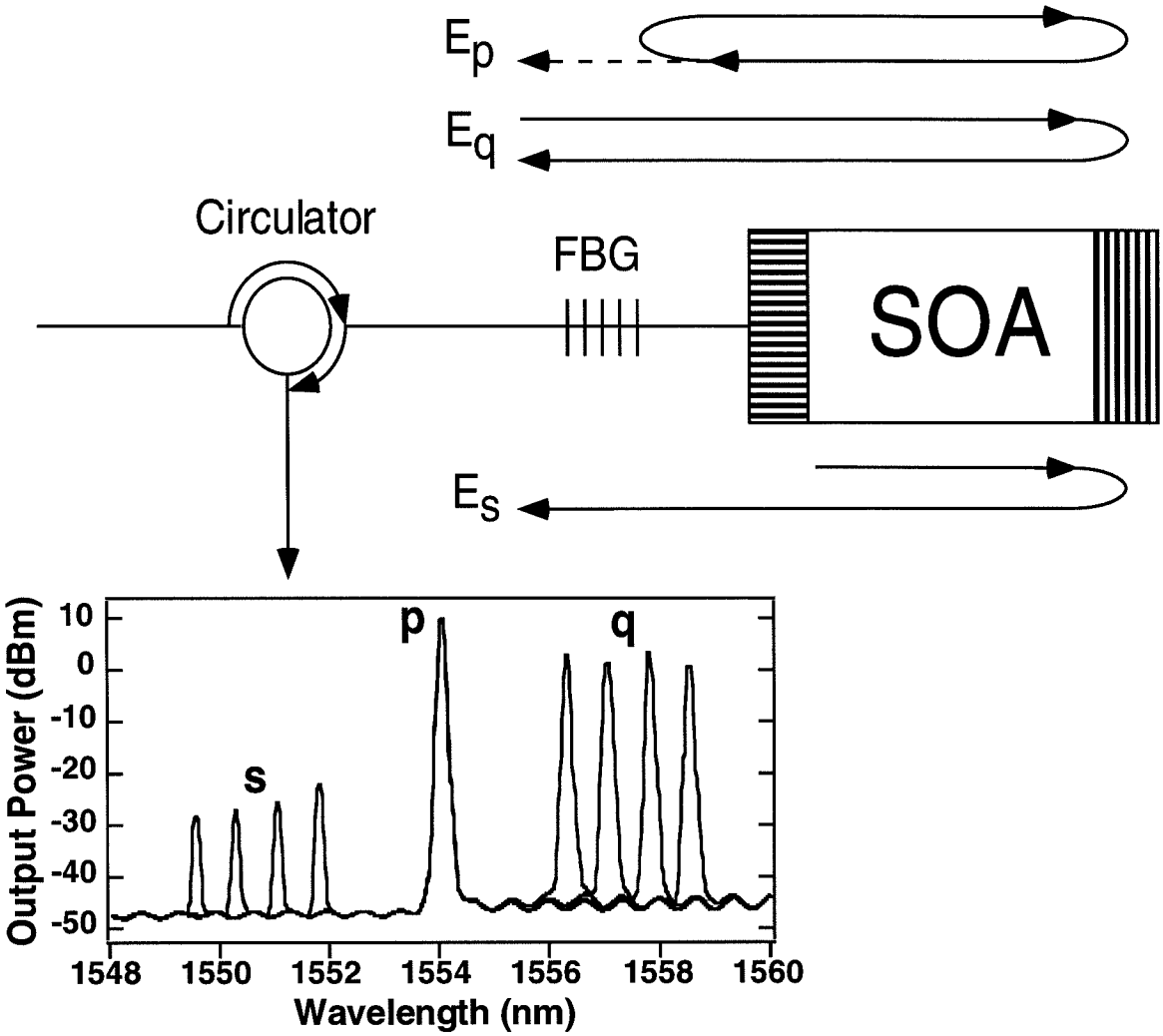

Figure 8.1: Schematic representation of the wavelength conversion device based on self-pumped FWM in a FBG coupled semiconductor laser. The bottom panel shows four superimposed optical spectra measured at the output of the converter, for wavelength downshifts of 4.5, 6, 7.5 and 9 nm (0.1 nm resolution bandwidth).

have frequencies well outside of the reflection band of the FBG, so that for these waves the device simply acts as a gain-clamped SOA. Notice that the reflection off the back mirror (folded-path SOA) effectively doubles the FWM interaction length, leading to an increase in conversion efficiency (however, as will be discussed below, the OSNR of the FWM signal is not correspondingly enhanced). Also shown in Fig. 8.1 (bottom panel) are four superimposed optical spectra measured at the output of the device, corresponding to wavelength (down)shifts of 4.5, 6, 7.5, and 9 nm.

The experimental setup used to measure the BER performance of this device [6] is similar to the one described in the previous chapter, section 7.3. The input signal was provided by a tunable external-cavity semiconductor laser, externally modulated at 2.5 Gbit/sec with a $2^7 - 1$ pseudorandom bit stream (no significant pattern length dependence was observed). Before being coupled into the laser (through a bidirectional coupler in this case), the input signal was amplified in an EDFA, filtered in a 1-nm bandpass filter to reduce the ASE noise from the EDFA, and then passed through a variable attenuator (used to measure the input-signal power dynamic range of the converter). The converted signal collected from the device output (through the other input arm of the bidirectional coupler) was similarly attenuated by a variable amount and then fed to the preamplified receiver. BER measurements were then performed with our HP 70800 Series BER tester.

In Fig. 8.2 we show the measured BER versus received power for the wavelength shifts of Fig. 8.1 (the eye diagram in the inset corresponds to the 4.5 nm shift). No significant degradation is observed except at the largest measured shift (the power

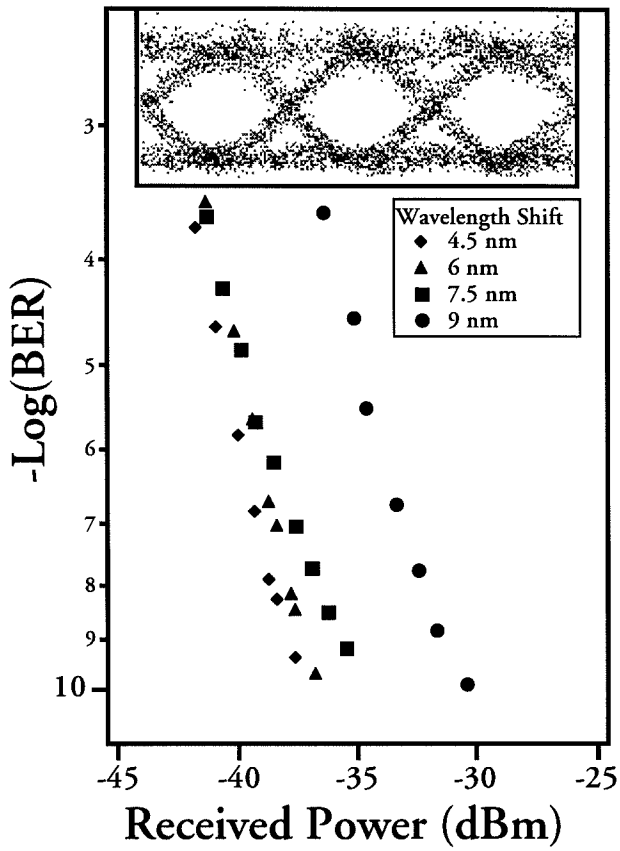

Figure 8.2: BER performance at 2.5 Gbit/sec of the wavelength conversion device based on self-pumped FWM. Top: eye diagram of the error-free converted signal for a 4.5-nm downshift. Bottom: BER versus received power curves, for wavelength downshifts of 4.5, 6, 7.5 and 9 nm.

penalty observed for this shift is in part due to instabilities of the input signal laser at that particular wavelength). Furthermore, we found that error rates lower than 10^{-9} could be obtained over a wide input-signal power range, approximately -10 to +2 dBm (coupled into the FBG) for the 4.5 nm shift. Incidentally, we notice that the degradation in BER performance at large input-signal powers is due not to a reduction in the optical gain as in the case of standard SOAs (since the gain here is

clamped by the lasing action), but rather by a reduction in pump power.

These results clearly indicate that the FWM configuration described in Fig. 8.1 is an attractive approach to wavelength conversion. Good conversion performance is obtained at 2.5 Gbit/sec, with significantly reduced device complexity (relative to the case of FWM wavelength converters based on single-pass SOAs) and low input-signal power requirements. While conversion with much larger wavelength shifts and higher bit rates has been recently demonstrated using specially optimized single-pass SOAs [4], [5] (as discussed in the previous chapter), it should be again emphasized that the present device was not designed specifically for this application. It is therefore worthwhile to investigate theoretically its margins of improvement as a wavelength converter.

To this purpose, we solve the coupled-mode equations of FWM in a FBG coupled laser, Eqs. (8.2)-(8.3) above, for $P_s^{out} = C|E_s^-(0)|^2$, subject to the boundary conditions depicted schematically in Fig. 8.1 (i.e., the boundary conditions of Eq. (8.4) with $E_p^{in} = E_s^{in} = 0$, and $R_{BG}(\omega_q) = R_{BG}(\omega_s) = 0$). The FWM conversion efficency (the ratio of the in-fiber converted signal output power to the input-signal power coupled into the FBG) is found to be given by

$$\eta = \left(\frac{P_p^{out}}{1 - R_{BG}(\omega_p)}\right)^2 \left| \int_0^L dz\ \Gamma\kappa(P_{tot}(z);\Omega) \left[\frac{G(z)}{\sqrt{R_{HC}}G(L)} + \frac{\sqrt{R_{HC}}G(L)}{G(z)}\right]\right|^2 . \quad (8.10)$$

In this expression, the first and second terms in the square brackets refer to the FWM signals generated by the forward and by the backward traveling waves respectively. Furthermore, we defined the overall gain over a length z of the laser active region,

$$G(z) = \exp \int_0^z \mathrm{dz}' \left[\Gamma \mathrm{g}(\mathrm{P_{tot}}(\mathrm{z}')) - \gamma\right] \quad (8.11)$$

with the lasing threshold condition requiring that

$$G(L) = \frac{1}{C\sqrt{R_{BG}(\omega_p)R_{HC}}} \tag{8.12}$$

Incidentally, notice that, due to the large asymmetry of the FBG coupled laser resonator, $P_{tot}(z)$ significantly varies along the cavity axis, so that even under threshold conditions one cannot take $\Gamma g(P_{tot}(z)) = g_{th}$ for all z in the active region.

Finally, the OSNR of the converted signal is given by $\eta P_q^{in}/P_{ASE}^{out}$, where P_{ASE}^{out} is the ASE noise power in the detector bandwidth $\Delta\nu_{res}$, and can be determined using the procedure described in Appendix B (properly modified to account for the high-reflection coating on the device back facet). The result is

$$P_{ASE}^{out} = \frac{h\nu_s \Delta\nu_{res}\Gamma}{\sqrt{R_{BG}}} \left\{ \int_0^L dz\ \beta(P_{tot}(z)) \left[\frac{\sqrt{R_{HC}}G(L)}{G(z)} + \frac{G(z)}{\sqrt{R_{HC}}G(L)} \right] \right\} \tag{8.13}$$

where β is the spontaneous emission rate per unit length of the laser active region (given in Eq. (B.21)), and again the first and second terms in the square brackets refer to the ASE noise generated in the forward and backward directions respectively.

As was discussed in chapter 7, dramatic improvements in the performance of FWM wavelength converters based on single-pass SOAs have been demonstrated [4], [5] by increasing the FWM interaction length. It is therefore interesting to consider how this approach would work in the case of the present device, especially in light of the fact that here the physical length of the semiconductor active region is used twice in the generation of the FWM signal (as well as of the ASE noise power in its spectral vicinity). In Figs. 8.3a and 8.3b, respectively, we plot the FWM conversion efficiency and the OSNR of the converted signal for a FBG coupled laser as a function of the length of the active region. For comparison, the same quantities are also plotted

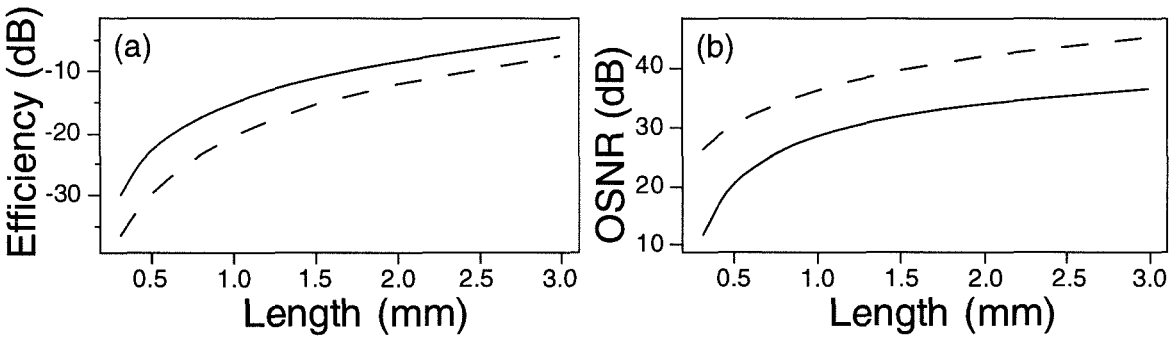

Figure 8.3: Theoretical conversion efficiency (a) and OSNR (b) of the self-pumped FBG coupled laser (continuous lines), and of an otherwise identical, externally pumped, single-pass SOA (dashed lines), versus length of the active medium (6 nm downshift).

(dashed lines) for the case of FWM in a single-pass but otherwise identical SOA (from Fig. 7.2). The approximation of Eq. (8.8) was used for the nonlinear coupling coefficient κ, with the value of $|\kappa_0(\Omega)|$ set to reproduce the measured conversion efficiency for the 6 nm wavelength shift. All other relevant parameters were set to the same values used in Fig. 7.2. Furthermore, we took $R_{BG}(\omega_p) = 25\%$ and $R_{HC} = 100\%$, and we varied the input signal power with length so as to maintain the ratio $P_p^+(0)/P_q^+(0)$ fixed (= 10 dB as in Fig. 7.2).

From Fig. 8.3a it is apparent that the FWM conversion efficiency significantly benefits from the folded-path SOA geometry. Indeed, in terms of conversion efficiency, the self-pumped converter described here roughly performs as a FWM converter based on a single-pass SOA twice as long. However, in the folded-path SOA, the physical length of the active region is used twice also in the generation and amplification of the ASE noise power, which is the main limiting factor to the converter BER

performance. As shown in Fig. 8.3b, in the case at hand this increase in P_{ASE}^{out} more than offsets the corresponding improvement in conversion efficiency. These results are in qualitative agreement with the experimental findings of [1] and [6]. We can then conclude that increasing the length of the FBG coupled laser would certainly improve its wavelength conversion performance, but it would not by itself be able to put it on par with the present state-of-the-art in FWM converters [4], [5]. Instead, more dramatic improvements can be obtained by designing the laser structure for higher power operation, to take advantage of the strong pump power dependence of the conversion efficiency and OSNR of this device, described below.

8.3.2 Gain Clamping and Pump Power Dependence

A peculiar feature of the FWM nonlinearity of SOAs is that it depends on the optical gain coefficient, and as a result it saturates with the total optical power present in the amplifier active region. Indeed, as discussed in the previous chapter, it has been shown [2], [3] that for single-pass SOAs there exists an "optimum" value of the pump power that maximizes the FWM conversion efficiency. At significantly lower values of $P_{tot} \approx P_p$, both the conversion efficiency and the OSNR of the FWM signal increase quadratically with it. As the pump power is increased beyond the "optimum" value, the conversion efficiency actually decreases while the OSNR further increases, but at a slower (sublinear) rate. Practical wavelength converters based on FWM in single-pass SOAs operate in this high-power regime, so that the benefits associated with a large pump power are nearly fully exploited in these devices.

In the self-pumped configuration, on the other hand, the optical gain is clamped at

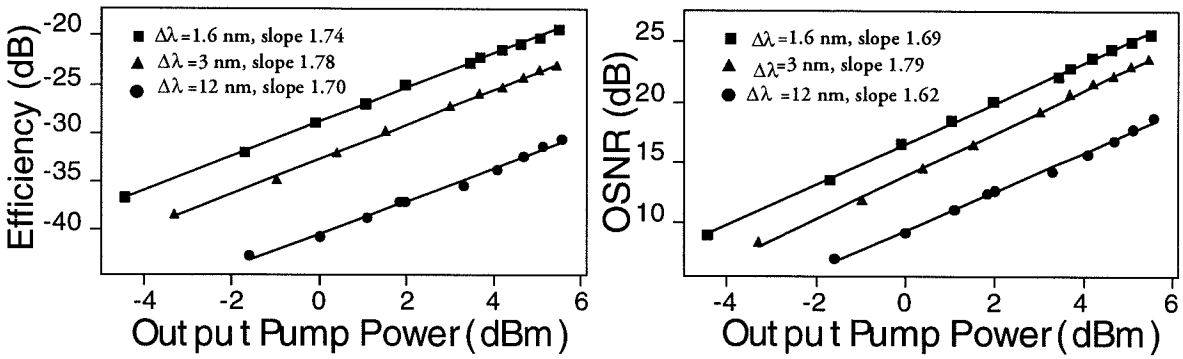

Figure 8.4: Experimental FWM conversion efficiency (a) and OSNR (b) of the self-pumped FBG coupled laser versus output pump power (measured at the output port of the circulator of Fig. 8.1), for several wavelength downshifts. The continuous lines are best-fit straight lines through the data, with slopes listed in the legend.

its threshold value by the lasing action, as indicated by Eq. (8.12). As a result, both the conversion efficiency and the OSNR of the FWM signal are expected to increase monotonically with pump power. This expectation is verified by the data shown in Figs. 8.4a and 8.4b, where we plot η and OSNR respectively versus P_p^{out} for several wavelength downshifts. The experimental setup used is the same as described above (with a cw input signal); P_p^{out} was varied by changing the bias current of the FBG coupled laser (the resulting temperature changes were compensated by constantly adjusting the device temperature controller during the measurement). From these plots, we find that as P_p^{out} is varied over a range of more than 10 dB, both η and OSNR vary as $(P_p^{out})^b$, with the exponent b ranging between 1.6 and 1.8 for the different wavelength shifts (no systematic dependence of b on $\Delta\lambda$ is observed).

In order to discuss these results, it is convenient to refer to Eq. (8.10) for the

conversion efficiency η and to Eq. (8.13) for the output ASE noise power P_{ASE}^{out}. First of all, using these equations it is easy to show that both η and OSNR will vary quadratically with P_p^{out} if $P_{tot}(z)$ is uniform along the laser axis. The reason is that in this case the gain coefficient g itself (not just the overall gain $G(L)$) is clamped (i.e., $\Gamma g(P_{tot}(z)) = g_{th}$ for all values of z), and therefore so are the FWM coupling coefficient κ and the whole integrals appearing in Eqs. (8.10) and (8.13).

In an asymmetric resonator such as the FBG coupled laser, however, the lasing power strongly varies along the axis (decreasing towards the higher reflectivity mirror): depending on the details of $g(P_{tot}(z))$ and $\kappa(P_{tot}(z))$, this may lead to a weak power dependence of the integrals of Eqs. (8.10), (8.13), and therefore explain the observed deviation from a purely quadratic dependence. In particular, a value for the exponent b slighty smaller than two (as in the data of Fig. 8.4) would seem to require a stronger saturation of the FWM coupling coefficient than assumed in Eq. (8.8) (i.e., a larger decrease in κ than g with increasing P_{tot}). While this is a plausible explanation, there is no additional evidence in its favor at this point; alternatively, the measured value of b could be attributed to other causes not directly related to the FWM process (such as, for instance, a slight power dependence of the fiber-laser coupling coefficient C).

In any case, the important thing in the present context is the strong dependence of η and OSNR on the pump power: notice from Fig. 8.4 that neither quantity appears to saturate as P_p^{out} approaches the upper end of its considered range of values. It is therefore apparent that a large improvement in the wavelength conversion

performance of this device can be obtained with a laser structure specifically designed for high-power operation. In fact, the data of Fig. 8.4 suggest that increasing the pump power may be a more effective optimization strategy for the case of self-pumped FWM than it is for FWM in single-pass SOAs. In this sense, semiconductor lasers with an on-chip DBR seem more promising in view of the extremely large output powers that can be obtained from them [13]. Large wavelength shifts at 10 Gbit/sec are therefore realistic even in the self-pumped configuration, which, in conjunction with its inherent simplicity, would make it quite attractive for system applications.

8.4 Wavelength Conversion by Injection-Locked FWM

The second wavelength conversion configuration considered in this chapter is illustrated schematically in Fig. 8.5. In this case, both the input signal and the pump wave are externally launched into the laser active region, with frequencies well outside of the FBG reflection band. On the other hand, the FWM signal frequency $\omega_s = 2\omega_p - \omega_q$ is chosen to nearly coincide with a longitudinal mode of the laser cavity. The laser is biased below the threshold required for oscillation in the presence of the pump wave alone. When the input signal is also turned on, the resulting FWM signal acts as a strong seed for oscillation of the nearby cavity mode. The FBG coupled laser is consequently locked to oscillate at the FWM signal wavelength, and it automatically generates a replica of the input signal at this wavelength. The net result is a sharp resonance enhancement of the FWM conversion efficiency and OSNR. This mechanism is entirely equivalent to the technique of injection locking, which,

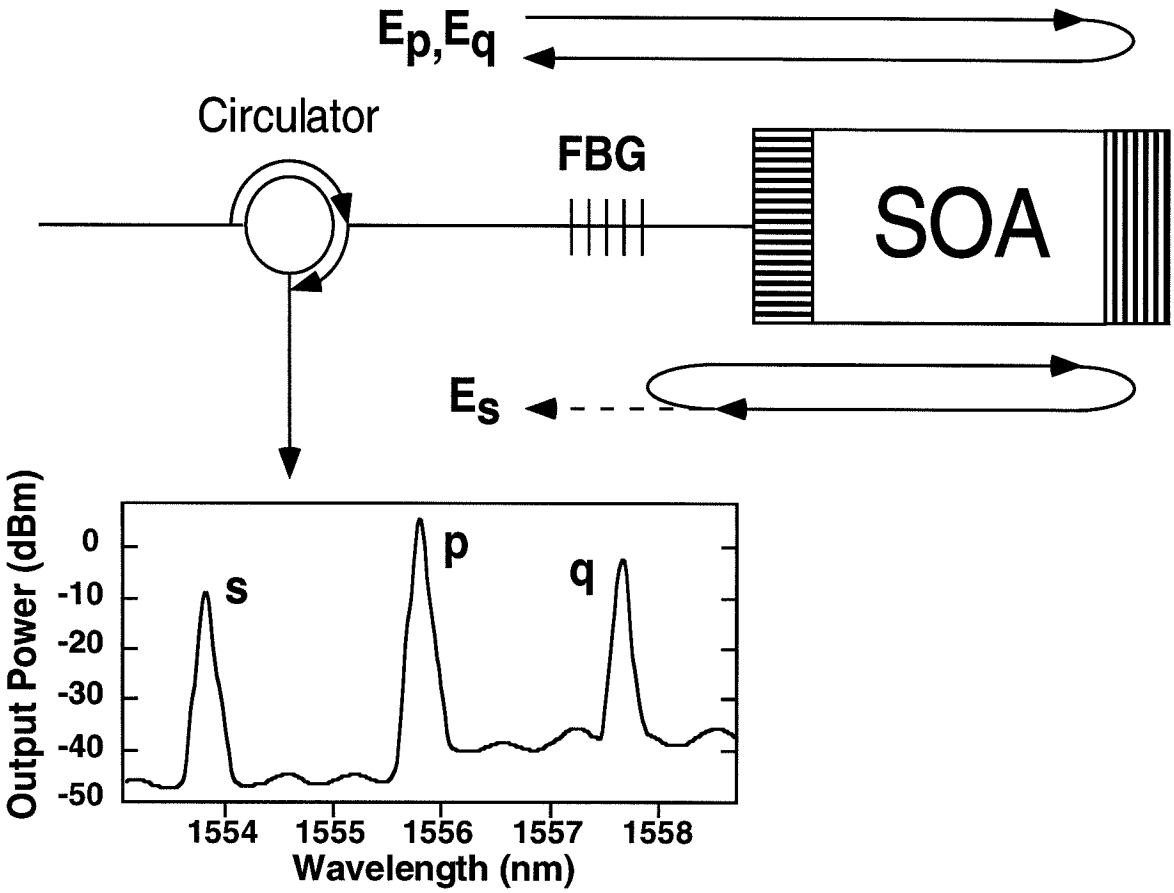

Figure 8.5: Schematic representation of the wavelength conversion device based on injection-locked FWM in a FBG coupled semiconductor laser. The bottom panel shows the optical spectrum measured at the output of the converter under resonance conditions, for a wavelength downshift of 4 nm (0.1 nm resolution bandwidth, less than 4 dBm total in-fiber input power).

in the context of semiconductor lasers, has been considered [14]–[16] as a means to improve their stability and noise properties, and, more recently, for all-optical signal processing applications [17], [18]. However, it is interesting to note that in this case the "master" laser beam is not externally injected, but rather generated inside the active medium by the FWM nonlinear interaction.

The panel at the bottom of Fig. 8.5 shows a typical output spectrum of this wavelength converter under resonance conditions, for a wavelength downshift of 4 nm. The experimental setup is the same as described above, except that two external-cavity lasers are now used to provide the two input waves (with their outputs combined in a bidirectional coupler before being fed into the same EDFA), and a broadband filter is now used for ASE prefiltering at the output of the EDFA. We see from this figure that the FWM signal is strongly enhanced by the optical feedback: for instance, if we refer to the smallest shift displayed in the bottom panel of Fig. 8.1 (a 4.5 nm downshift in the self-pumped configuration), and we keep into account the larger pump power used there, this enhancement can be quantified to be more than two orders of magnitude. In fact, given that the fiber-to-fiber gain experienced by the input signal in the injection-locked converter is approximately equal to $1/R_{BG} \approx 6$ dB, we find that the FWM conversion efficiency in Fig. 8.5 is close to unity.

In Fig. 8.6, we plot the measured FWM conversion efficiency as a function of the frequency of the converted signal (relative to the center frequency of the largest resonance): several resonances, associated with various modes of the FBG coupled laser cavity, are clearly resolved. The spectral width of these resonances is quite small,

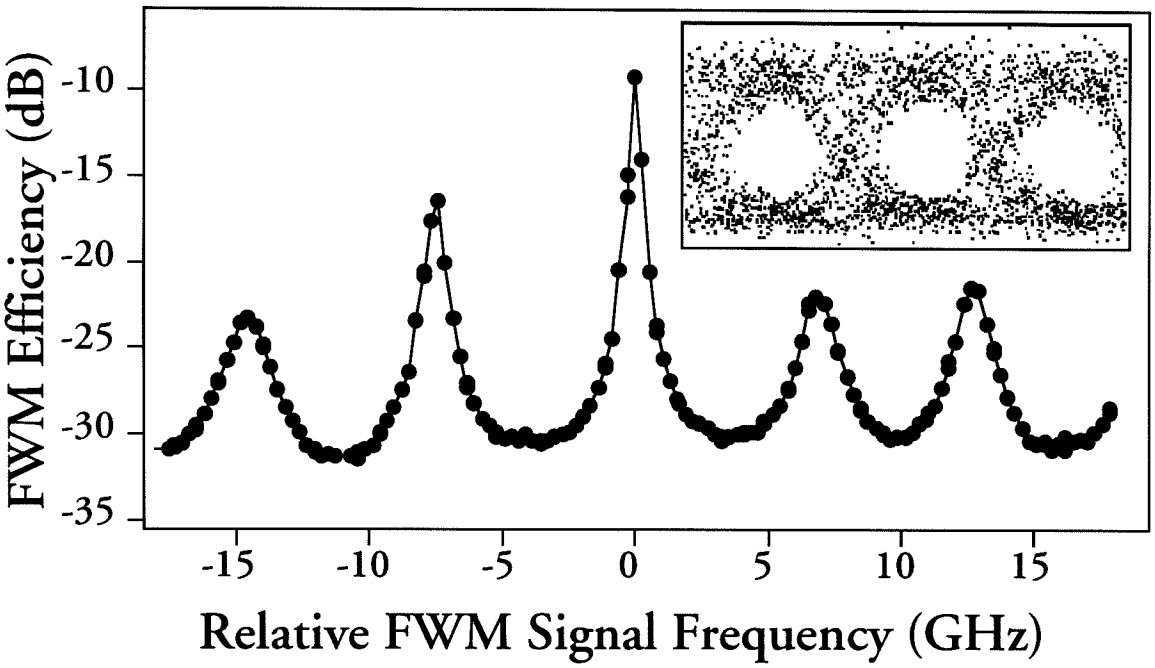

Figure 8.6: Conversion efficiency for injection-locked FWM in the FBG coupled laser versus frequency of the converted signal (4-nm downshift, approximately 5 dBm total in-fiber input power), and (inset) eye diagram at 1 Gbit/sec.

less than 2 GHz for all the peaks in the figure. This poses a serious limitation to the applicability of the present device to wavelength conversion of high-speed signals, because of the spectral distortion that occurs when the bit rate is comparable to, or larger than, the resonance width. In a preliminary study, we obtained conversion with best-case BER of 10^{-9} at 1 Gbit/sec, with eye-diagram as shown in the inset of Fig. 8.6 (the corresponding BER vs. received-power curves exhibit a strong flooring). Also, we found, consistent with the measured width of the injection-locking resonances, that the conversion performance rapidly degraded at higher bit rates.

Based on these results, it is apparent that the width of the resonances must be

significantly improved in order to increase the maximum bit rate at which this wavelength converter can operate. In the following we will discuss how to specifically design the laser structure to this purpose, again using the theoretical framework developed in section 8.2. From the solution of Eqs. (8.2) and (8.3) with the boundary conditions depicted schematically in Fig. 8.5 (i.e., the boundary conditions of Eq. (8.4) with $E_s^{in} = 0$ and $R_{BG}(\omega_q) = R_{BG}(\omega_p) = 0$), the FWM conversion efficiency can be written as

$$\eta = f(\omega_s) \times \eta|_{R_{BG}\to 0} \tag{8.14}$$

where we defined

$$f(\omega_s) = \frac{1 - R_{BG}(\omega_s)}{\left|1 - C\sqrt{R_{HC}R_{BG}(\omega_s)}G(L)e^{i\Delta\Phi(\omega_s)}\right|^2}. \tag{8.15}$$

The quantity $\eta|_{R_{BG}\to 0}$ is the conversion efficiency of the same device used in the injection-locked FWM configuration, with the same power distribution $P_{tot}(z)$, but without the FBG (i.e., operated as an externally pumped, folded-path SOA). Analytically, it is given by the same expression for the FWM efficiency of the self-pumped configuration, Eq. (8.10) (with $R_{BG}(\omega_p) = 0$ in this case); numerically, however, these two quantities may be quite different, because of the different power distributions, and hence overall gain, in the two configurations.

The function $f(\omega_s)$ given in Eq. (8.15) provides a measure of the performance enhancement associated with the optical feedback. In this equation, $G(z)$ is the overall gain of Eq. (8.11); notice that due to the large emission into "lasing mode" (by the FWM interaction) $G(L)$ can significantly differ from its threshold value in

this case, and Eq. (8.12) should be replaced by

$$G(L) = \frac{e^{\Gamma A \Delta \bar{N} L}}{C\sqrt{R_{BG}(\omega_s) R_{HC}}}$$

$$\Delta \bar{N} \equiv \int_0^L \frac{dz}{L}\, \Delta N(P_{tot}(z)) \tag{8.16}$$

with $\Delta \bar{N} < 0$ in this configuration. Furthermore, the quantity $\Delta\Phi$ introduced in Eq. (8.15) is the round-trip phase shift in the laser cavity, given by

$$\Delta\Phi(\omega_s) = \frac{l_{BG}(\omega_s) + 2\bar{n}L}{c}\omega_s - 2\int_0^L dz\; \Gamma \delta k(P_{tot}(z)) =$$

$$= 2m\pi + \frac{l_{BG}(\omega_s) + 2\bar{n}L}{c}(\omega_s - \omega_m) \tag{8.17}$$

where m is an integer, and ω_m is the frequency of the mth longitudinal mode of the solitary laser in the presence of the power distribution $P_{tot}(z)$ (the second equality in Eq. (8.17) assumes that ω_s is sufficiently close to ω_m that $l_{BG}(\omega_s) \approx l_{BG}(\omega_m)$). It is interesting to note that, in the case of standard laser operation, Eq. (8.15) gives the ratio of the output power of the laser to the spontaneous emission power emitted into the lasing mode; near threshold this factor is very large, which explains, in the present case, the strong enhancement in the FWM signal power.

Using Eqs. (8.16) and (8.17) in (8.15), the enhancement function $f(\omega_s)$ can be rewritten as follows

$$f(\omega_s) = \frac{1 - R_{BG}(\omega_m)}{\left(1 - e^{\Gamma A \Delta \bar{N}_m L}\right)^2 + 4e^{\Gamma A \Delta \bar{N}_m L}\sin^2(\pi \frac{\omega_s - \omega_m}{\Delta\omega_m})} \tag{8.18}$$

where again we took $\omega_s \approx \omega_m$, and we defined the cold-cavity free spectral range near ω_m

$$\Delta\omega_m \equiv \frac{c}{l_{BG}(\omega_m) + 2\bar{n}L}. \tag{8.19}$$

Furthermore, notice that ΔN depends on ω_m through $R_{BG}(\omega)$, see Eqs. (8.7) and (8.6), hence the subscript m. Equation (8.18) has the general form of a Fabry-Perot transmission function, with the mth peak centered at the mode frequency ω_m and having FWHM $\delta\omega_L^m$ and maximum value E_{max}^m given by

$$\delta\omega_L^m \approx \frac{\Delta\omega_m}{\pi} \frac{1 - e^{\Gamma A \Delta \bar{N}_m L}}{e^{\Gamma A \Delta \bar{N}_m L/2}},$$

$$E_{max}^m \approx \frac{1 - R_{BG}(\omega_m)}{\left(1 - e^{\Gamma A \Delta \bar{N}_m L}\right)^2}. \tag{8.20}$$

As mentioned before, the spectral width $\delta\omega_L^m$ sets the maximum bit rate at which the wavelength converter described here can operate. The laser structure to be used in this converter should therefore be designed so as to maximize this quantity. Incidentally, we notice that, as long as the approximation of Eq. (8.9) holds, the entire bandwidth of the locking resonances given above is stable against small carrier density fluctuations (whereas, as originally pointed out by Lang [14] in the context of standard injection-locking, if the laser gain is saturated by the injection-locked beam itself, a fraction of this steady-state locking range would actually become unstable for nonzero linewidth enhancement factor).

From inspection of Eq. (8.20), we find that the largest improvement in the performance of this converter can be obtained by maximizing the free spectral range $\Delta\omega_m$, since the width of the locking resonances increases linearly with it, while the conversion efficiency is not affected (at least insofar as the length L of the mixing medium is not reduced). In practice, this can be accomplished by shortening the optical path length in the Bragg mirror, which, in the present device, accounts for the larger part of the measured 7 GHz free spectral range.

The bandwidth $\delta\omega_L^m$ also increases with increasing $\Gamma A\Delta\bar{N}_m L$; the FWM signal enhancement E_{max}^m, however, correspondingly undergoes a larger decrease. Therefore, maximizing $\Gamma A\Delta\bar{N}L$ does not necessarily improve the performance of the converter. Instead, this quantity should be optimized to achieve the largest bandwidth for which the conversion efficiency remains larger than a given threshold (e.g., large enough to support error-free wavelength conversion in a given link); for instance, this can be simply accomplished by properly selecting the input pump power ($|\Delta N|$ increases with the optical power as confirmed by Eq. (8.7)). This is illustrated in Fig. 8.7, where the circles and the continuous lines are, respectively, experimental and theoretical values of $\delta\omega_L^m$ and E_{max}^m/E_{min}^m (the peak-to-valley ratio of the resonance) versus the input power P_p^{in} (the parameter values used in this simulation are similar to those used for Fig. 8.3; furthermore, for simplicity, here we replaced $P_{tot}(z)$ in Eq. (8.7) with its average along the laser axis).

In conclusion, significant improvements over the experimental results presented here can be expected, mainly by maximizing the free spectral range. In the FBG coupled laser, this can be accomplished by writing the grating as close to the lensed fiber tip as possible, and by reducing its length. Also, an on-chip DBR, whether external or distributed, could be used instead, which should allow for an increase of $\Delta\omega_m$ by more than a factor of ten, and therefore make this device suitable for operation at 10 Gbit/sec (in addition a DBR laser has the advantage of tunability of the resonance frequency). Finally, we point out that the wavelength selectivity of this converter could become quite important in certain applications, such as the selective

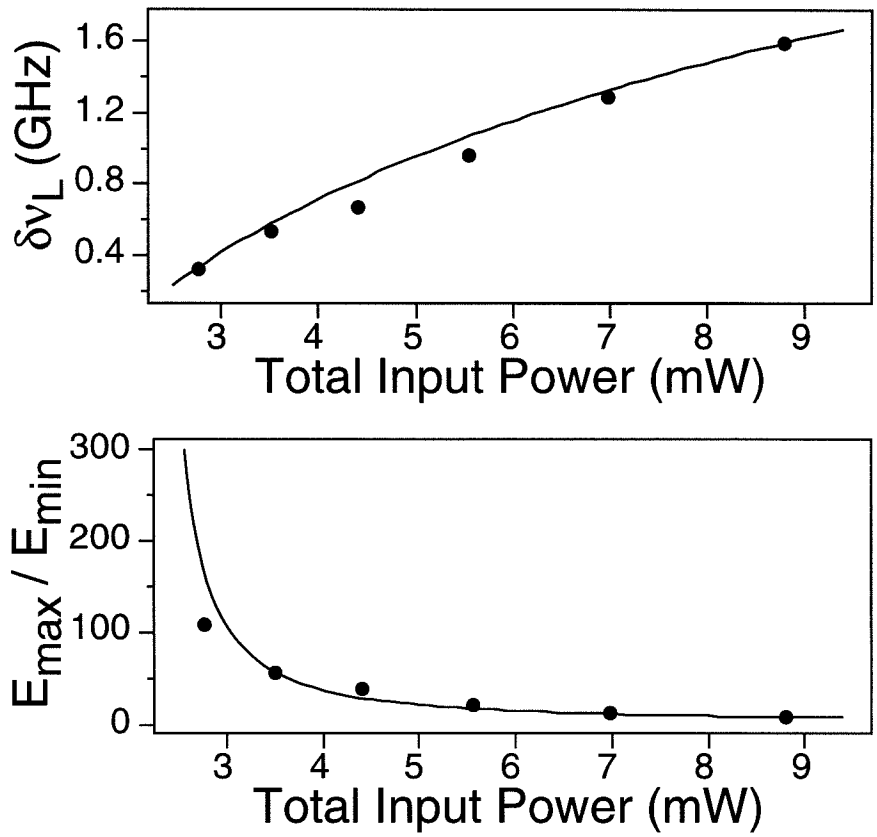

Figure 8.7: Spectral width (upper panel) and peak-to-valley ratio (lower panel) of the FWM injection-locking resonance centered at the frequency of the solitary laser output, versus total in-fiber input power (4 nm downshift). The continuous lines are theoretical fits to the model discussed in the text.

conversion of one out of several WDM channels (e.g., for dynamic channel copying and dropping).

Bibliography

[1] D. F. Geraghty, R. B. Lee, M. Verdiell, M. Ziari, A. Mathur, and K. J. Vahala, "Wavelength conversion for WDM communication systems using four-wave mixing in semiconductor optical amplifiers," *IEEE J. Select. Topics Quantum Electron.*, vol. 3, pp. 1146–1155, 1997.

[2] M. A. Summerfield and R. S. Tucker, "Optimization of pump and signal powers for wavelength converters based on four-wave mixing in semiconductor optical amplifiers," *IEEE Photon. Technol. Lett.*, vol. 8, pp. 1316–1318, 1996.

[3] A. D'Ottavi, F. Girardin, L. Graziani, F. Martelli, P. Spano, A. Mecozzi, S. Scotti, R. Dall'Ara, J. Eckner, and G. Guekos, "Four-wave mixing in semiconductor optical amplifiers: a practical tool for wavelength conversion," *IEEE J. Select. Topics Quantum Electron.*, vol. 3, pp. 522–528, 1997.

[4] G. Hunziker, R. Paiella, A. D'Ottavi, P. Spano, R. Dall'Ara, G. Guekos, and K. J. Vahala, "30 nm Wavelength Conversion at 10 Gb/s by Four-Wave Mixing in a Semiconductor Optical Amplifier," presented at the *Optical Fiber Communication Conference*, San Jose, California, 1998, paper WB7.

[5] A. E. Kelly, D. D. Marcenac, and D. Nesset, "40 Gbit/s wavelength conversion over 24.6 nm using FWM in a semiconductor optical amplifier with an optimised MQW active region," *Electron. Lett.*, vol. 33, pp. 2123–2124, 1997.

[6] G. Hunziker, R. Paiella, M. Ziari, A. Mathur, and K. J. Vahala, "Folded-path self-pumped wavelength converter based on four-wave mixing in a semiconductor optical amplifier," *IEEE Photon. Technol. Lett.*, vol. 9, pp. 1352 – 1354, 1997.

[7] R. Paiella, G. Hunziker, M. Ziari, A. Mathur, and K. J. Vahala, "Wavelength Conversion by Four-Wave Mixing in a Folded-Path, Self-Pumped Semiconductor

Optical Amplifier," presented at the *Optical Fiber Communication Conference*, San Jose, California, 1998, paper WB8.

[8] R. Paiella, G. Hunziker, M. Ziari, A. Mathur, and K. J. Vahala, "Wavelength conversion by cavity-enhanced injection-locked four-wave mixing in a fiber-Bragg-grating coupled diode laser," *IEEE Photon. Technol. Lett.*, vol. 10, pp. 802–804, 1998.

[9] H. Kuwatsuka, H. Shoji, M. Matsuda, and H. Ishikawa, "Nondegenerate four-wave mixing in a long cavity $\lambda/4$-shifted DFB laser using its lasing beam as pump beams," *IEEE J. Quantum Electron.*, vol. 33, pp. 2002–2010, 1997.

[10] G. P. Agrawal, "Population pulsations and nondegenerate four-wave mixing in semiconductor lasers and amplifiers," *J. Opt. Soc. Am. B*, vol. 5, pp. 147–158, 1988.

[11] A. Mecozzi, S. Scotti, A. D'Ottavi, E. Iannone, and P. Spano, "Four-wave mixing in traveling-wave semiconductor amplifiers," *IEEE J. Quantum Electron.*, vol. 31, pp. 689–699, 1995.

[12] I. Koltchanov, S. Kindt, K. Petermann, S. Diez, R. Ludwig, R. Schnabel, and H. G. Weber, "Gain dispersion and saturation effects in four-wave mixing in semiconductor laser amplifiers," *IEEE J. Quantum Electron.*, vol. 32, pp. 712–720, 1996.

[13] F. Delorme, G. Alibert, P. Boulet, S. Grosmaire, S. Slempkes, and A. Ougazzaden, "High reliability of high-power and widely tunable 1.55-μm distributed Bragg reflector lasers for WDM applications," *IEEE J. Select. Topics Quantum Electron.*, vol. 3, pp. 607-614, 1997.

[14] R. Lang, "Injection locking properties of a semiconductor laser," *IEEE J. Quantum Electron.*, vol. 18, pp. 976-983, 1982.

[15] F. Mogensen, H. Olesen, and G. Jacobsen, "Locking conditions and stability properties for a semiconductor laser with external light injection," *IEEE J. Quantum Electron.*, vol. 21, pp. 784-793, 1985.

[16] N. Schunk and K. Petermann, "Noise analysis of injection-locked semiconductor injection lasers," *IEEE J. Quantum Electron.*, vol. 22, pp. 642-650, 1986.

[17] K. Weich, E. Patzak, and J. Hörer, "Fast all-optical switching using two-section injection-locked semiconductor lasers," *Electron. Lett.*, vol. 30, pp. 493-494, 1994.

[18] L. Li and K. Petermann, "Small-signal analysis of optical-frequency conversion in an injection-locked semiconductor laser," *IEEE J. Quantum Electron.*, vol. 30, pp. 43-48, 1994.

Chapter 9

All-Optical WDM Logic Gates

9.1 Introduction

As discussed in the previous two chapters, FWM in semiconductor gain media is an attractive candidate for the implementation of wavelength conversion. Recently, FWM has also been investigated for more involved all-optical signal processing applications in fiber-optic communication networks [1]–[3]. Indeed, as the aggregate bandwidth of these networks increases, it becomes natural to investigate whether some of the simplest network functions may be efficiently performed in the optical layer. For instance, this approach is expected to become more and more advantageous as the bit rate per channel is increased to 40 Gbit/sec and beyond, since it is not clear whether electronic switching devices will be practical at these speeds. In fact, a family of all-optical logic gates, based on ultrafast nonlinear interferometers (with SOAs as the nonlinear elements), has recently been demonstrated for operation up to 100 Gbit/sec [4], [5].

In light of the current trend towards the use of WDM in optical networks, it is interesting to consider new forms of all-optical signal processing, specifically designed to take advantage of multiwavelength transmission. In particular, in this chapter we will investigate byte-wide WDM, i.e., the parallel transmission and processing of entire bytes of information on a single fiber, with each bit assigned to a different WDM channel. This transmission format was first theoretically studied, to our knowledge, in a paper published in 1988 [6], in which a case was made for the use of byte-wide WDM in local-area computer links (in particular to eliminate the need for costly high-speed serializer/deserializer nodes and protocol handling circuitry). Subsequent publications also considered the use of a multiwavelength data bus for improved error-correction algorithms [7], as well as to eliminate the need for clock recovery [8]. These advantages are in part offset by the penalties associated with the group-velocity-dispersion induced bit skew across the multiwavelength byte. In particular, in Ref. [6], the authors showed that, because of bit skew, byte-wide WDM transmission cannot improve the maximum data rate of a conventional serial link. It should be mentioned, however, that this conclusion is no longer necessarily true if dispersion management techniques (not well established in 1988) are employed.

In any case, all-optical signal processing in a byte-wide WDM system requires a new class of logic gates, specifically designed to operate on multiwavelength input bits. The FWM interaction is an ideal candidate for the implementation of such logic elements, since it automatically compares two input bits at different wavelengths (i.e., the FWM pump and probe waves) and generates their AND product (the converted

signal) at a new wavelength, logically related to those of the input signals. Furthermore, the use of SOAs as the nonlinear mixing elements allows for ultrafast switching times, as well as for the monolithic integration of the basic logic gates. These can then be arranged in parallel and/or cascaded combinations to realize more sophisticated processing functions (in this respect, it is important to point out that cascaded wavelength conversion by FWM in SOAs is possible, as was recently demonstrated [9]).

In this chapter, we propose and demonstrate all-optical logic gates based on FWM in SOAs [2], for signal processing applications in such byte-wide WDM systems. Notice that the FWM interaction alone cannot be used to perform logical inversion (i.e., the NOT operation) in any simple way. One could resort to other nonlinear processes in a SOA to invert the power level of a WDM channel, such as cross-gain or cross-phase modulation. However, these processes are slower than FWM and therefore, in principle, they would reduce the maximum clock rate; furthermore, they would require an extra SOA for every inversion. In this work, we use the polarization state (instead of the power level) of each wavelength channel to define its logical state, which leads to an extremely simple and instantaneously fast implementation of the NOT operation. Namely, we select two orthogonal polarization states (e.g., TE and TM), and interpret one as the logical "1" and the other as the logical "0." The NOT gate is then immediately provided by a half-wave polarization element.

Because of the polarization selection rules discussed in section 3.3, FWM will then provide a test for a condition of coincidence of two waves in the same logical state.

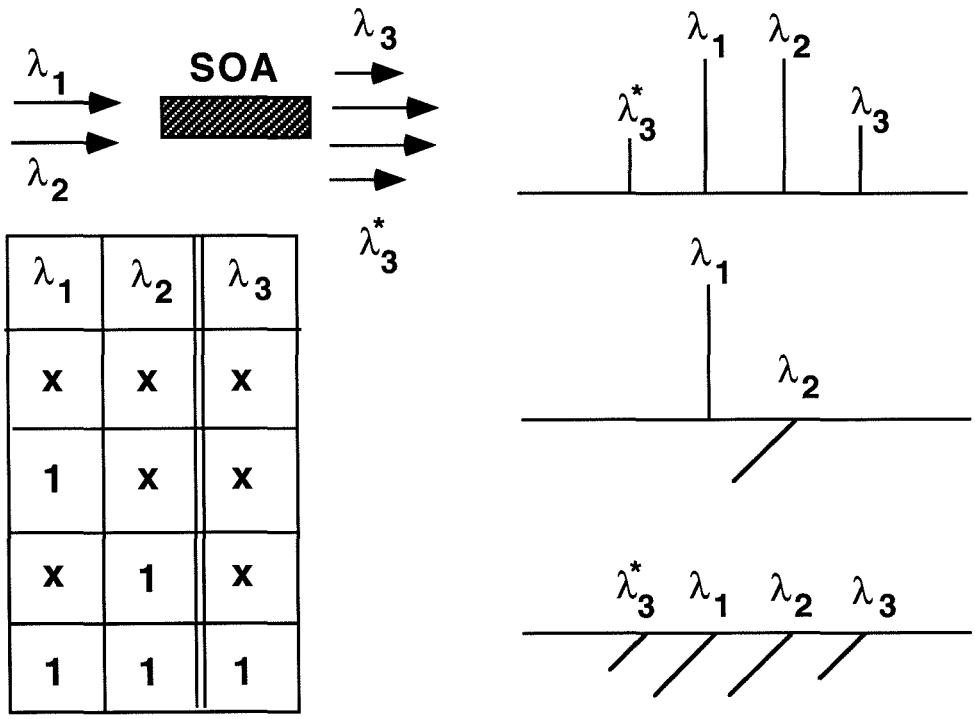

Figure 9.1: Schematic representation of the conditional test function performed by FWM in a SOA on polarized data. The corresponding truth table is also shown, with the symbol "1" ("X") signifying that power is (is not) present in the given wavelength.

This is illustrated in Fig. 9.1, together with the corresponding truth table, where the symbol "1" ("X") signifies that power is (is not) present in the given wavelength. Incidentally, notice that here we are neglecting the FWM contribution described in section 3.5 (involving a TE pump wave and a TM probe wave, or vice versa), since, as was discussed there, in most cases of practical interest this contribution is negligible. We emphasize that the conditional test function provided by FWM occurs on femtosecond time scales and is therefore essentially instantaneous for all data rates

of interest. As will be shown in the next section, a set of FWM elements behaving as shown in Fig. 9.1 (e.g., SOAs) and polarization rotators can be used to implement any desired logic gate. A preliminary experimental demonstration of an exclusive OR (EXOR) gate is given in section 9.3.

9.2 Operation of the Logic Gates

9.2.1 Basic Architecture

Conceptually, the construction of each logic gate can be divided into three main steps, as illustrated schematically in Fig. 9.2 for the specific case of the EXOR gate. In this discussion we will assign the TM polarization state to the logical mark ("1"), and the TE polarization state to the logical space ("0"), and use the notation λ_C^P, where $P = 1, 0$ (TM, TE) denotes the polarization state of wavelength channel number C (= 1, 2 for the two input signals, and 3 for the gate output).

The first step consists of resolving the optical input to the gate according to both wavelength and polarization. In practice, this is accomplished with a series of wavelength- and polarization-selective beamsplitters (not shown in the figure), possibly integrated in a single waveguide. In the second step, some of the resulting wavelength and polarization products are inverted (i.e., their polarization is rotated by 90° with a half-wave polarization element, indicated by a solid circle in Fig. 9.2), in a way that depends upon the desired truth table. Finally, these waves are coupled in the appropriate number of SOAs (two for any two-input/one-output logic gate), where the FWM conditional test function (third step) occurs. The output of the logic

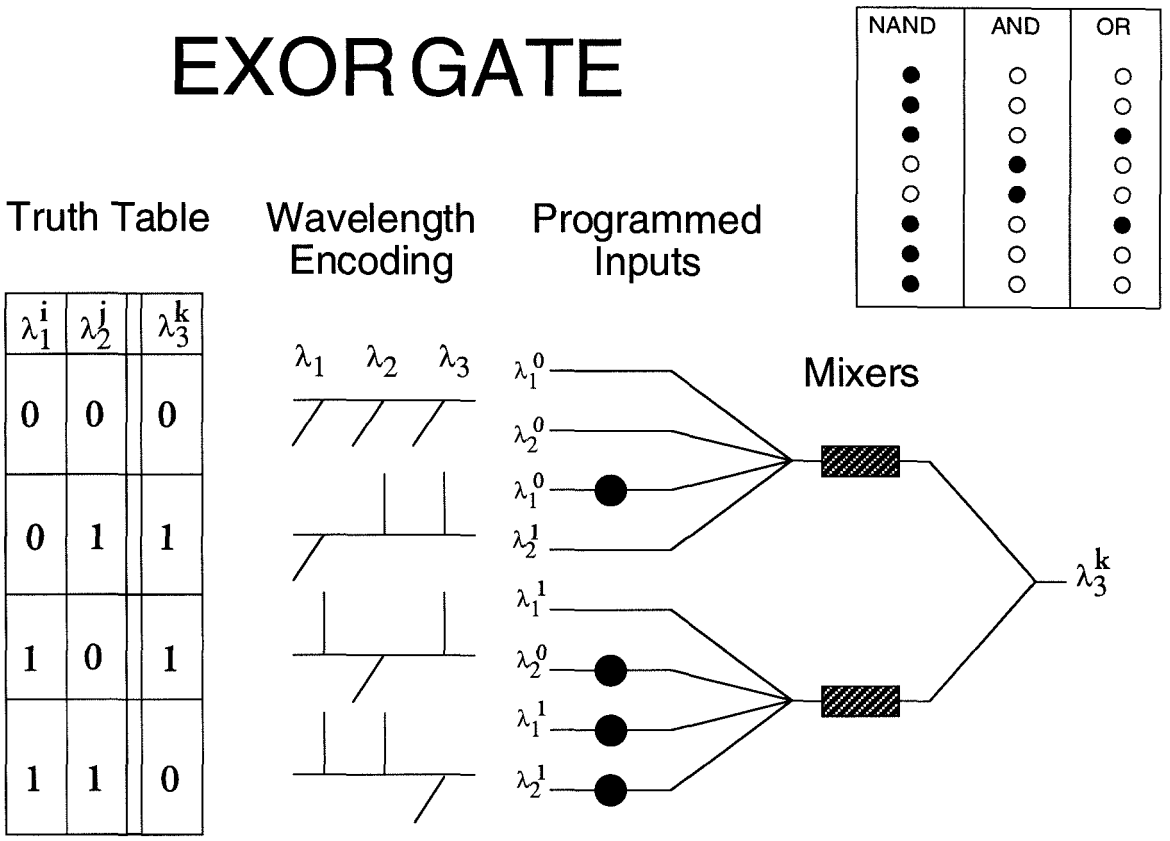

Figure 9.2: Conceptual diagram of the WDM EXOR gate. The arrangement of the polarization rotators (denoted by the solid circles) for other common logic gates is given in the inset.

gate is then given by the combined output of these SOAs, with the input wavelengths filtered out.

For clarity, we will next describe this procedure in some details for the specific case of the EXOR gate. As shown in Fig. 9.2, the wavelength and polarization products of the first step are paired to form the four possible binary combinations. The bottom pair in the figure, $[\lambda_1^1, \lambda_2^1]$, correspond to logical "1" on each wavelength

channel (i.e., both are TM polarized). The EXOR truth table requires that the gate output be a logical "0" (a TE polarized wave) in this case. If each input is inverted (i.e., half-wave elements are inserted on the bottom two guides, as denoted by the solid circles), then FWM between these two waves will produce a new wave with the desired (TE) polarization.

Proceeding up to the next two inputs, a logical "1" (TM) on the first input wavelength and a logical "0" (TE) on the second input wavelength require a logical "1" (TM) output according to the EXOR truth table. This requires that a half-wave element be introduced on the second input as indicated, so that when the $[\lambda_1^1, \lambda_2^0]$ input ([1, 0], or [TM, TE]) occurs, FWM will create a third wave polarized TM or logical "1." Proceeding up the remaining inputs, the truth table locations are filled in as shown. There is a unique arrangement of half-wave elements for each truth table (the arrangements corresponding to other common two-input/one-output logic gates are shown in the inset of Fig. 9.2). The placement of these half-wave elements therefore amounts to programming the truth table into the gate.

Notice that two SOAs are used in the EXOR gate of Fig. 9.2. In fact, it is always necessary, in the implementation of any two-input/one-output logic gate, to separate the four binary pairings into two subgroups as shown in this figure, each coupled to a different SOA. Otherwise, spurious outcomes are created in the FWM process for certain input combinations. For instance, it is easy to see from Fig. 9.2 that if only one SOA were used, the input $[\lambda_1^0, \lambda_2^1]$ ([0, 1], or [TE, TM]) would result in a FWM signal with nonzero TE and TM components (instead of being TM polarized

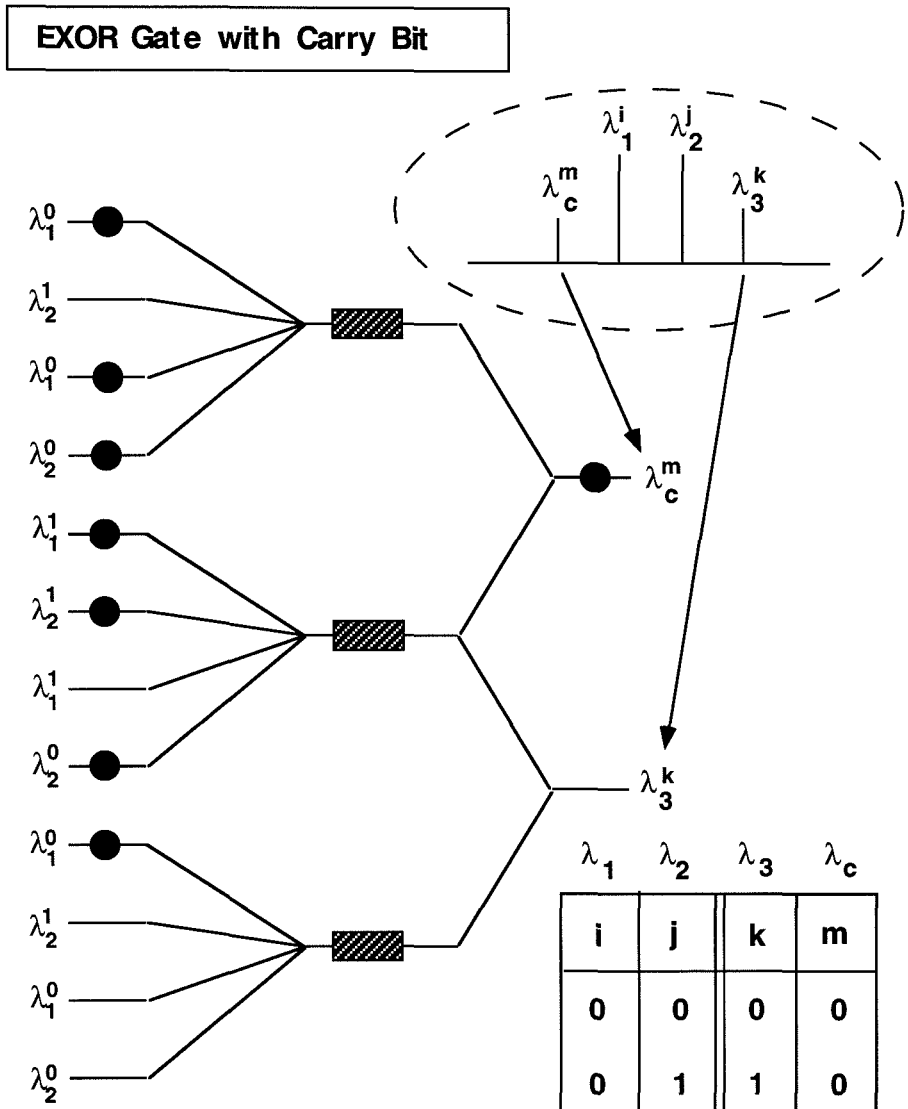

λ_1	λ_2	λ_3	λ_c
i	j	k	m
0	0	0	0
0	1	1	0
1	0	1	0
1	1	0	1

Figure 9.3: Conceptual diagram of the WDM EXOR gate with an additional output for the carry bit.

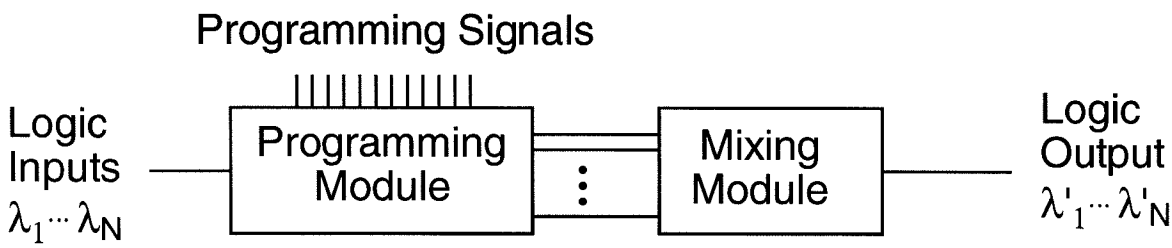

Figure 9.4: Architecture of a generic WDM logic gate. As shown in this figure, the functions related to programming (polarization control) and those related to conditional testing (FWM) can be separated into two distinct modules, which may be advantageous for increased ease of fabrication. Furthermore, the former module may be made dynamically reconfigurable.

as required by the truth table).

More involved multi-input and/or multi-output logic gates can also be constructed with the procedure just described (in general requiring more than two SOAs). As an example, in Fig. 9.3 we give the schematics of an EXOR gate with an additional output for the carry bit, which could be used as a building block for a binary adder circuit.

9.2.2 Practical Implementation

In order to be able to use these logic gates to realize more sophisticated processing functions, it is essential that they may be monolithically integrated. Indeed, present-day photonic-integrated-circuit technology can be used to make compact optical waveguide chips, including all the passive elements required to carry out the first

two steps in gate construction. Furthermore, notice that the architecture of the logic gates allows for a convenient separation of such waveguide chip (the programming module) from the FWM conditional test elements (e.g., the SOAs). This feature is quite attractive because it makes it possible to use two different fabrication technologies. For instance, a dynamically programmable set of gates could use electrical (or optical) control signals to reconfigure their function by reprogramming the configuration of invertors (this is illustrated in Fig. 9.4). This might require the use of a thin film fabrication technology that is incompatible with the FWM element technology (e.g., InGaAsP active waveguides), thus requiring the kind of separation just described.

The EXOR gate described in the previous subsection can be implemented as shown in Fig. 9.5. The dashed box denotes the waveguide chip, which can be realized using planar silica-on-silicon waveguide technology (for a review of this technology see Ref. [10]). The mask layout of the chip, by PIRI corporation, is also shown at the bottom of the figure. In this photonic circuit, the input beam is first split in a bidirectional coupler, each arm of which is followed by a temperature-tunable Mach-Zender interferometer where the two wavelength channels are separated. These are then passed in the appropriate set of polarization elements, and finally recombined in either output port of the chip. It is easy to see that each port will then contain the required input to each SOA, consistently with Fig. 9.2.

For optimum FWM performance, an EDFA followed by a band-pass filter (BPF) for ASE prefiltering is placed before each SOA (the advantages of this configuration

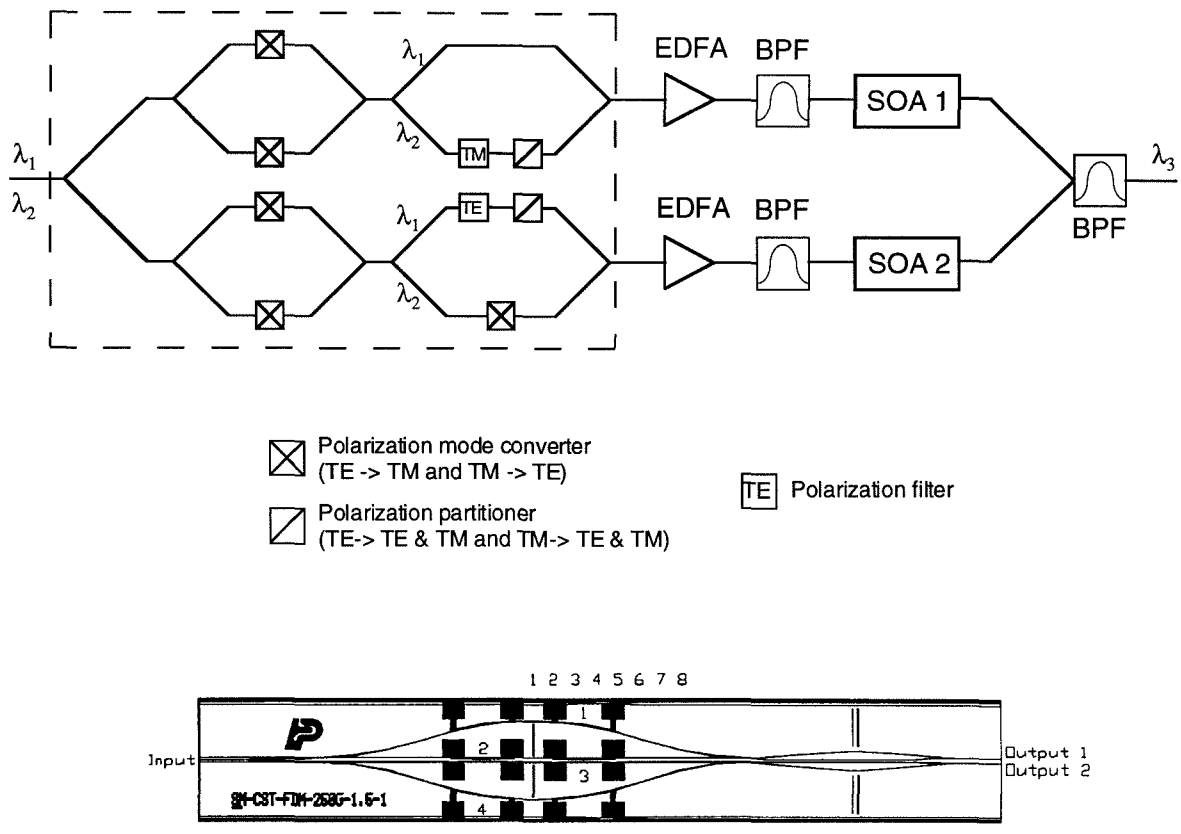

Figure 9.5: Top: practical implementation of the WDM EXOR gate. Bottom: mask layout of the photonic integrated chip used for the programming module (the region enclosed in the dashed box in the diagram above). The black squares here denote the electrical heating pads used to adjust the wavelength position of the demultiplexers. The polarization elements are inserted into grooves denoted by the vertical lines.

are described in details in section 7.2). Notice that in order to preserve the polarization states selected by the programming module, polarization maintaining (PM) fibers should be used throughout the gate. Equivalently, one could do with non-PM fibers between the waveguide chip and the SOAs, and use a polarization controller (PC) to properly realign the polarization states right at the input of each SOA. The only requirement in this case is that the wavelength separation between the two input signals is not so large that the fiber birefringence significantly changes the overlap between their polarization unit vectors (e.g., if they are orthogonal at the output of the chip, they should remain orthogonal entering the SOAs). In practice, a few hundreds of GigaHertz is entirely appropriate in this respect.

Finally, we should spend a few words regarding the signal source to be used to generate polarization encoded light signals. This can be realized using a dual-output $LiNbO_3$ Mach-Zender modulator, with two PM-fiber output ports, one providing the modulating signal (data) and the other its complement (data-bar). Both output fibers are then spliced to the input ports of a PM-fiber polarization combiner; in particular, in one arm the PM fibers are spliced with their slow axes aligned to each other, in the other arm they are spliced with their slow axes making a 90° angle. Then (provided that light is initially launched into the Mach-Zender modulator linearly polarized along either polarization eigenaxis) the output of the polarization combiner will contain data along one axis and data-bar along the other, as required by our polarization encoding scheme. Notice that it is of critical importance that the optical path length between the modulator and the combiner be the same in the two arms,

to avoid any timing offset between the two polarization components.

9.3 Experimental Demonstration

In a preliminary experiment [2], we have tested the operation of the EXOR gate by implementing it in the simple way shown in Fig. 9.6. Notice that we did not use PM waveguides in this experiment; as a result, we could not obtain the required polarization components at the input of each SOA by simply using TM (λ_1^1 and λ_2^1) and TE (λ_1^0 and λ_2^0) waves followed by the appropriate polarization rotators (as in Fig. 9.5). Instead, we used the PCs shown in Fig. 9.6 (each of which is labeled by the polarization state that it is set to produce at the SOA input).

Furthermore, due to limited availability of components, only one of the input signals (X_1, of wavelength λ_1) was modulated with digital information. This signal was provided by an externally modulated DFB laser. The modulator was the dual-output Mach-Zehnder interferometer described above, whose two output ports provide the modulating signal and its complement (i.e., the waves λ_1^1 and λ_1^0 respectively). This was driven by our Hewlett-Packard BER tester with a preset bit pattern (at 2.5 Gbit/sec). On the other hand, the other input signal (X_2, of wavelength λ_2, provided by an external cavity laser diode (ECLD)) was not modulated, and set first to a logical "1" and then to a logical "0." In the former case, the EXOR truth table requires that the output signal Y be the complement of X_1; in the latter case that $Y = X_1$.

The results of this experiment are also shown in Fig. 9.6. The upper trace is the

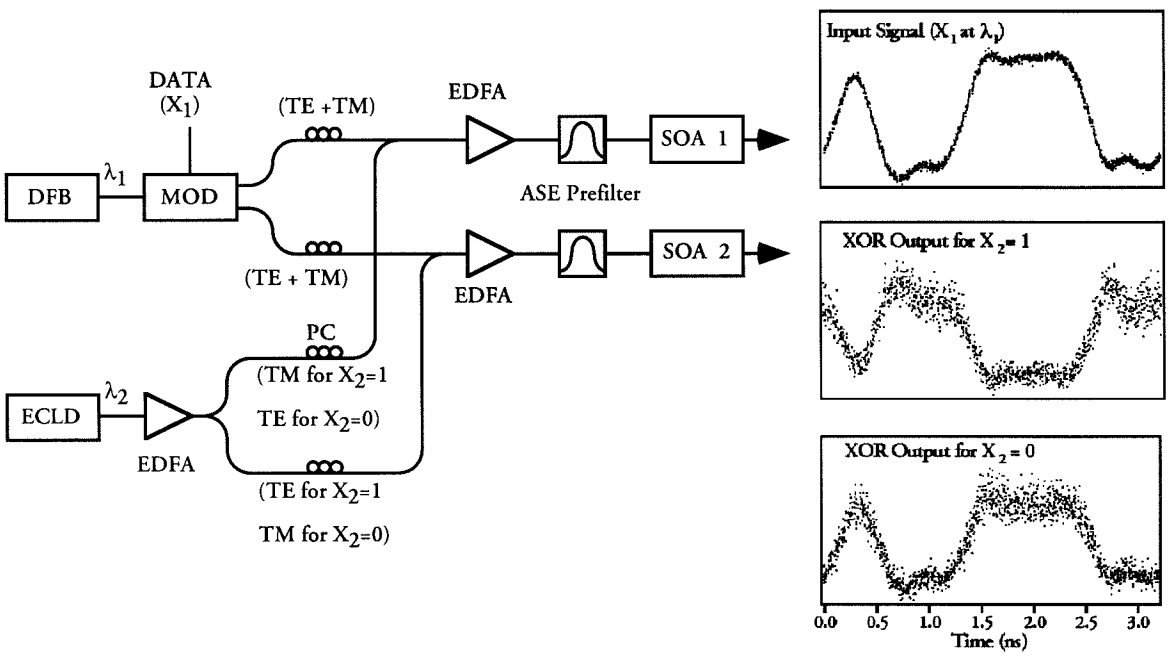

Figure 9.6: Experimental setup used to demonstrate the WDM EXOR gate, and the corresponding measurement results. The upper trace is the input bit pattern X_1. The middle and lower traces represent the output signal of the gate given that the other input X_2 is, respectively, a logical one and a logical zero. The implementation of the EXOR truth table is clearly seen.

preset bit pattern (10011100) encoded on the input signal X_1 (i.e., the optical intensity in wave λ_1^1), measured with the Hewlett-Packard microwave transition analyzer. The middle trace corresponds to the case $X_2 = 1$ and shows the FWM signal generated in SOA 1, which in this case is the TM component of the overall output wave of the EXOR gate. As such, this trace gives the output signal Y (given that TM is interpreted as a logical "1"). Consistent with the truth table, we indeed find it to be the complement of X_1. Similarly, the bottom trace gives Y for $X_2 = 0$ (i.e., the FWM signal from SOA 2 in this case), which can be seen to be equal to X_1, again as required by the truth table. The SOAs used in the experiment (two alternating-strain MQW devices [11] similar to the one described in chapter 4) have a small-signal gain of only approximately 10 dB, which results in fairly low FWM conversion efficiency and OSNR; this explains the additional noise on the two output traces.

9.4 Conclusions and Outlook

It is apparent that this experiment is only a preliminary demonstration, and many challenges need to be met to make these logic gates attractive for practical applications. In particular, the relative timing of the different field components is an important issue, because of the group-velocity-dispersion induced bit skew across the wavelength bus, as well as the polarization walk-off between data and data-bar at a same wavelength (due to the different group velocities of the two polarization eigenaxes of PM fibers). The former problem may not be too severe for small wavelength detunings between the channels in the bus, and in general it may be dealt with us-

ing standard dispersion compensation techniques. As for the polarization walk-off, it may be minimized by implementing each PM fiber span with two segments of equal length, spliced together with their slow axes at 90° (so that each polarization component travels equal lengths of fiber aligned with the slow and with the fast axes).

Furthermore, the implementation described in section 9.2 may still be too bulky for many applications, when several gates are needed. However, we point out that optical amplifiers [12] and filters [13] can also, in principle, be integrated in a same photonic circuit. Therefore, it is realistic to expect that in a few years a much higher level of miniaturization of these gates will be commercially feasible.

Finally, we consider the question of what kind of applications one may envision for these logic gates. As was mentioned in the introduction, the basic idea is to take advantage of the multiple wavelength channels of WDM systems for byte-wide transmission on a single fiber. Incidentally, because of the bit-skew problem, this may in general be more appropriate to local area networks. A specific application that seems very well suited to this kind of transmission format is the implementation of error correction algorithms in the optical layer. For instance, one may assign a number of wavelength channels in the overall byte to parity bits, and then use the WDM logic gates to perform the corresponding error correction (e.g., Hamming) code. Another application is to extend the useful range of high-speed computer interconnections without resorting to serializer-deserializer nodes. This implies the implementation of all-optical digital circuits, whose complexity will be ultimately limited by the level of performance and integration of the logic gates.

Bibliography

[1] D. Nesset, M. Tatham, and D. Cotter, "All-optical AND gate operating on 10 Gbit/s signals at the same wavelength using four-wave mixing in a single semiconductor laser amplifier," *Electron. Lett.*, vol. 31, pp. 896–898, 1995.

[2] K. J. Vahala, R. Paiella, and G. Hunziker, "Ultrafast WDM logic," *IEEE J. Select. Topics Quantum Electron.*, vol. 3, pp. 698–701, 1997.

[3] S. Diez, C. Schmidt, R. Ludwig, H. G. Weber, K. Obermann, S. Kindt, I. Koltchanov, and K. Petermann, "Four-wave mixing in semiconductor optical amplifiers for frequency conversion and fast optical switching," *IEEE J. Select. Topics Quantum Electron.*, vol. 3, pp. 1131–1145, 1997.

[4] N. S. Patel, K. L. Hall, and K. A. Rauschenbach, "40 Gbit/s cascadable all-optical logic with an ultrafast nonlinear interferometer," *Optics Lett.*, vol. 21, pp. 1466–1468, 1996.

[5] K. L. Hall and K. A. Rauschenbach, "100 Gb/s all-optical logic," presented at the *Optical Fiber Communication Conference*, San Jose, California, 1998, post-deadline paper PD5.

[6] M. L. Loeb and G. R. Stilwell, Jr., "High-speed data transmission on an optical fiber using a byte-wide WDM system," *J. Lightwave Technol.*, vol. 6, pp. 1306-1311, 1988.

[7] S.-K. Shao and M.-S. Kao, "WDM coding for high-capacity lightwave systems," *J. Lightwave Technol.*, vol. 12, pp. 137-148, 1994.

[8] K. Kazi, "Elimination of clock recovery and framing by transporting clock, data and synchronization pulse for OC-192 using WDM," *J. Lightwave Technol.*, vol. 13, pp. 2136-2141, 1995.

[9] R. B. Lee, D. F. Geraghty, K. J. Vahala, M. Verdiell, M. Ziari, and A. Mathur, "Cascaded wavelength conversion by four-wave mixing in a strained semiconductor optical amplifier at 10 Gb/s," *IEEE Photon. Technol. Lett.*, vol. 9, pp. 752–754, 1997.

[10] M. Kawachi, "Recent progress in silica-based planar lightwave circuits on silicon," *IEE Proceedings in Optoelectronics*, vol. 143, pp. 257–262, 1996.

[11] M. A. Newkirk, B. I. Miller, U. Koren, M. G. Young, M. Chien, R. M. Jopson, and C. A. Burrus, "1.5 μm multiquantum-well semiconductor optical amplifier with tensile and compressively strained wells for polarization-independent gain," *IEEE Photon. Technol. Lett.*, vol.4, pp. 406–408, 1993.

[12] Y. C. Yan, A. J. Faber, H. de Waal, P. G. Kik, and A. Polman, "Erbium-doped phosphate-glass waveguide on silicon with 4.1 dBG/cm gain at 1.535 μm," *Appl. Phys. Lett.*, vol. 71, pp. 2922–2924, 1997.

[13] Y. Hibino, T. Kitagawa, K. O. Hill, F. Bilodeau, B. Malo, J. Albert, and D. C. Johnson, "Wavelength-division multiplexer with photoinduced Bragg gratings fabricated in a planar-lightwave-circuit-type A symmetrical Mach-Zender interferometer on Si," *IEEE Photon. Technol. Lett.*, vol. 8, pp. 84–86, 1996.

Appendix A

Microscopic Expressions for the FWM Susceptibility Tensor Components

In chapter 3 we presented a full microscopic theory of FWM in semiconductor gain media, including polarization effects. In particular, the FWM susceptibility tensor χ_{ijkl} was found to have the general form given in Eq. (3.8). In this Appendix we give explicit expressions [1] for all the quantities appearing in that equation. The scalar susceptibilities associated with carrier density modulation, carrier heating and spectral hole burning respectively are as follows:

$$\chi_{ijkl}|_{CDM} = \frac{i}{\hbar^3}\frac{\tau_s}{1-i\Omega\tau_s}\times$$

$$\frac{1}{V}\left(\sum_{|\vec{k}|}\frac{1}{1-i\Omega\tau_1}\left|M\right|^2\left\langle\sum_{v,c}(\vec{\mu}_{cv})_j(\vec{\mu}_{vc})_i\right\rangle\frac{\partial\Delta f}{\partial N}\hat{\chi}(\omega_s)\right)\times$$

$$\frac{1}{V}\left(\sum_{|\vec{k}|}\left|M\right|^2\left\langle\sum_{v,c}(\vec{\mu}_{cv})_k(\vec{\mu}_{vc})_l\right\rangle\Delta f\left(\hat{\chi}(\omega_p)-\hat{\chi}^*(\omega_q)\right)\right), \tag{A.1}$$

$$\chi_{ijkl}|_{CH}=\frac{i}{\hbar^3}\frac{\tau_h}{1-i\Omega\tau_h}\times$$

$$\frac{1}{V}\left(\sum_{|\vec{k}|}\frac{1}{1-i\Omega\tau_1}\left|M\right|^2\left\langle\sum_{v,c}(\vec{\mu}_{cv})_j(\vec{\mu}_{vc})_i\right\rangle(\Delta_T f)\ \hat{\chi}(\omega_s)\right)\times$$

$$\frac{1}{V}\left(\sum_{|\vec{k}|}\left|M\right|^2\left\langle\sum_{v,c}(\vec{\mu}_{cv})_k(\vec{\mu}_{vc})_l\right\rangle\Delta f\left(\hat{\chi}(\omega_p)-\hat{\chi}^*(\omega_q)\right)\right), \tag{A.2}$$

$$\chi_{ijkl}|_{SHB(1)}=\frac{i}{\hbar^3}\frac{1}{V}\sum_{|\vec{k}|}\frac{\tau_1}{1-i\Omega\tau_1}\left|M\right|^4\times$$

$$\left\langle\sum_{v,c,v'}(\vec{\mu}_{cv})_j(\vec{\mu}_{vc})_i(\vec{\mu}_{cv'})_k(\vec{\mu}_{v'c})_l+\sum_{v,c,c'}(\vec{\mu}_{vc})_i(\vec{\mu}_{cv})_j(\vec{\mu}_{vc'})_l(\vec{\mu}_{c'v})_k\right\rangle\times$$

$$\Delta f\hat{\chi}(\omega_s)\left(\hat{\chi}(\omega_p)-\hat{\chi}^*(\omega_q)\right), \tag{A.3}$$

and

$$\chi_{ijkl}|_{SHB(2)}=\frac{i}{\hbar^3}\frac{1}{V}\sum_{|\vec{k}|}\frac{\tau_2}{1-i\Omega\tau_2}\left|M\right|^4\times$$

$$\left\langle\sum_{v,c,v'}(\vec{\mu}_{\bar{c}v})_j(\vec{\mu}_{vc})_i(\vec{\mu}_{cv'})_k(\vec{\mu}_{v'\bar{c}})_l+\sum_{v,c,c'}(\vec{\mu}_{vc})_i(\vec{\mu}_{c\bar{v}})_j(\vec{\mu}_{\bar{v}c'})_l(\vec{\mu}_{c'v})_k\right\rangle\times$$

$$\Delta f\hat{\chi}(\omega_s)\left(\hat{\chi}(\omega_p)-\hat{\chi}^*(\omega_q)\right), \tag{A.4}$$

where we introduced the matrix element $M=\langle S,\uparrow\ |ex|X,\uparrow\ \rangle$, the Fermi inversion factor $\Delta f=f_v-f_c$, the complex lineshape function

$$\hat{\chi}(\omega) = \frac{1}{\omega - \omega_{cv} + i\tau_{cv}^{-1}} \tag{A.5}$$

and the quantity

$$\Delta_T f = \frac{\epsilon_v - \mu_v}{h_v}\frac{\partial f_v}{\partial T_v} - \frac{\epsilon_c - \mu_c}{h_c}\frac{\partial f_c}{\partial T_c}. \tag{A.6}$$

All other symbols appearing in Eqs. (A.1)-(A.6) are defined in section 3.2. The Fermi distribution functions above are to be evaluated under conditions of quasi-equilibrium (as determined by the electrical pumping). Also, in Eq. (A.4) the index $\bar{c}$ is defined so that, given c, $\bar{c} \neq c$ (for instance, if c denotes spin-up, $\bar{c}$ denotes spin-down), and similarly for $\bar{v}$. Furthermore, in writing these expressions we assumed isotropic in-plane dispersion relations, so that the only quantities depending on the direction of the 2D wavevector $\vec{k}$ are the dipole moments $\vec{\mu}_{vc}$, and $< .. >$ denotes averaging over all directions of $\vec{k}$.

Next, we consider the summations over the indexes c, v, which, once substituted in Eqs. (A.1)-(A.4), entirely determine the polarization properties of the FWM susceptibility. We consider the general case of a QW with arbitrary (or zero) strain, for which the doubly-degenerate conduction- and valence-band states can be written as [2]

$$|C1(2)\rangle = |f_k^e\rangle \otimes |S, \uparrow (\downarrow)\rangle$$

$$|V1(2)\rangle = |f_k^{hh}\rangle \otimes \left(v^*|\frac{3}{2},\frac{3}{2}\rangle \mp v|\frac{3}{2},-\frac{3}{2}\rangle\right) + |f_k^{lh}\rangle \otimes \left(w^*|\frac{3}{2},-\frac{1}{2}\rangle \mp w|\frac{3}{2},\frac{1}{2}\rangle\right)$$

$$v = \frac{1}{\sqrt{2}}e^{i(\frac{3\pi}{4}-\frac{3\xi}{2})} \qquad w = \frac{1}{\sqrt{2}}e^{i(-\frac{\pi}{4}+\frac{\xi}{2})} \qquad \xi = arctan\left(\frac{k_y}{k_x}\right), \tag{A.7}$$

where $|f_k^e\rangle$, $|f_k^{lh}\rangle$, $|f_k^{hh}\rangle$ are the envelope-function state vectors for electrons, light holes and heavy holes.

With these expressions used to compute the dipole moment matrix elements, we find

$$\left\langle \sum_{v,c} \vec{\mu}_{cv}\vec{\mu}_{vc} \right\rangle = \left(|\langle f_k^e|f_k^{hh}\rangle|^2 + \frac{1}{3}|\langle f_k^e|f_k^{lh}\rangle|^2 \right) \hat{x}\hat{x} + \frac{4}{3}|\langle f_k^e|f_k^{lh}\rangle|^2 \hat{z}\hat{z}. \tag{A.8}$$

$$\begin{aligned} \left\langle \sum_{v,c,v'} \vec{\mu}_{vc}\vec{\mu}_{cv}\vec{\mu}_{cv'}\vec{\mu}_{v'c} \right\rangle &= \left\langle \sum_{v,c,c'} \vec{\mu}_{vc}\vec{\mu}_{cv}\vec{\mu}_{c'v}\vec{\mu}_{vc'} \right\rangle = \\ = \left(\frac{1}{2}|\langle f_k^e|f_k^{hh}\rangle|^4 + \frac{2}{3}|\langle f_k^e|f_k^{hh}\rangle|^2|\langle f_k^e|f_k^{lh}\rangle|^2 + \frac{1}{18}|\langle f_k^e|f_k^{lh}\rangle|^4 \right) \hat{x}\hat{x}\hat{x}\hat{x} + \\ + \left(\frac{2}{3}|\langle f_k^e|f_k^{hh}\rangle|^2|\langle f_k^e|f_k^{lh}\rangle|^2 + \frac{2}{9}|\langle f_k^e|f_k^{lh}\rangle|^4 \right) (\hat{x}\hat{x}\hat{z}\hat{z} + \hat{z}\hat{z}\hat{x}\hat{x}) + \frac{8}{9}|\langle f_k^e|f_k^{lh}\rangle|^4 \hat{z}\hat{z}\hat{z}\hat{z}, \end{aligned} \tag{A.9}$$

$$\begin{aligned} \left\langle \sum_{v,c,v'} \vec{\mu}_{vc}\vec{\mu}_{\bar{c}v}\vec{\mu}_{cv'}\vec{\mu}_{v'\bar{c}} \right\rangle &= \left\langle \sum_{v,c,c'} \vec{\mu}_{vc}\vec{\mu}_{c\bar{v}}\vec{\mu}_{c'v}\vec{\mu}_{\bar{v}c'} \right\rangle = \\ = \left(\frac{2}{3}|\langle f_k^e|f_k^{hh}\rangle|^2|\langle f_k^e|f_k^{lh}\rangle|^2 + \frac{2}{9}|\langle f_k^e|f_k^{lh}\rangle|^4 \right) (\hat{x}\hat{z}\hat{x}\hat{z} + \hat{z}\hat{x}\hat{z}\hat{x}) + \\ - \left(\frac{2}{3}\left(\langle f_k^{hh}|f_k^e\rangle\langle f_k^e|f_k^{lh}\rangle\right)^2 + \frac{2}{9}|\langle f_k^e|f_k^{lh}\rangle|^4 \right) \hat{x}\hat{z}\hat{z}\hat{x} + \\ - \left(\frac{2}{3}\left(\langle f_k^{lh}|f_k^e\rangle\langle f_k^e|f_k^{hh}\rangle\right)^2 + \frac{2}{9}|\langle f_k^e|f_k^{lh}\rangle|^4 \right) \hat{z}\hat{x}\hat{x}\hat{z} \end{aligned} \tag{A.10}$$

where we use $\hat{x}$ and $\hat{z}$ to denote the TE and TM directions respectively. From these equations, the FWM polarization selection rules discussed in section 3.3 are immediately derived. In passing, we note that the limiting forms of Eqs. (A.8)-(A.10) appropriate to highly tensile-strained (compressively strained) quantum wells are obtained by taking $|f_k^{hh}\rangle \to 0$ ($|f_k^{lh}\rangle \to 0$).

A more compact expression for χ_{ijkl} can be obtained from Eqs. (A.1)-(A.4), if the dependence of the dipole moment matrix elements on $|\vec{k}|$ can be neglected, which is in particular a valid approximation when valence-band mixing is negligible [2] (i.e., near $\vec{k} = 0$ and/or in highly strained QW structures). Then, the dipole products can be taken out of the sums over $|\vec{k}|$, which results in the general form for χ_{ijkl} given in Eq. (3.8). The scalar susceptibilities χ_{CDM}, χ_{CH}, $\chi_{SHB(1)}$, and $\chi_{SHB(2)}$ introduced there can then be immediately obtained from Eq. (A.1), (A.2), (A.3), and (A.4) respectively (by comparison with Eq. (3.8)). We emphasize that the expressions obtained with this procedure are consistent with a previous "scalar" theory of FWM in SOAs [3] (in which polarization effects were not included).

Finally, we give the full expressions for the scalar susceptibilities $\chi_{CDM}^{C\leftarrow C}$ and $\chi_{CDM}^{C\leftarrow T}$ introduced in chapter 4 (see Eq. (4.6)), appropriate to an alternating-strain MQW SOA with interwell coupling:

$$\chi_{CDM}^{C\leftarrow C} = \frac{i}{\hbar^3} \frac{\tau_e^C \left(1 - i\Omega\tau_e^T\right)}{\left(1 - i\Omega\tau_e^C\right)\left(1 - i\Omega\tau_e^T\right) - \tau_e^C\tau_e^T / \left(\tau_t^{C\leftarrow T}\tau_t^{T\leftarrow C}\right)} \times \frac{1}{V^C}\left(\sum_{|\vec{k}|} \frac{1}{1 - i\Omega\tau_1} \left|M^C\right|^2 \frac{\partial \Delta f^C}{\partial N} \hat{\chi}^C(\omega_s)\right) \times \frac{1}{V^C}\left(\sum_{|\vec{k}|} \left|M^C\right|^2 \Delta f^C \left(\hat{\chi}^C(\omega_p) - \left(\hat{\chi}^C(\omega_q)\right)^*\right)\right), \tag{A.11}$$

$$\chi_{CDM}^{C\leftarrow T} = \frac{i}{\hbar^3} \frac{\tau_e^C\tau_e^T / \tau_t^{C\leftarrow T}}{\left(1 - i\Omega\tau_e^C\right)\left(1 - i\Omega\tau_e^T\right) - \tau_e^C\tau_e^T / \left(\tau_t^{C\leftarrow T}\tau_t^{T\leftarrow C}\right)} \times \frac{1}{V^C}\left(\sum_{|\vec{k}|} \frac{1}{1 - i\Omega\tau_1} \left|M^C\right|^2 \frac{\partial \Delta f^C}{\partial N} \hat{\chi}^C(\omega_s)\right) \times$$

$$\frac{1}{V^T}\left(\sum_{|\vec{k}|}\left|M^T\right|^2\Delta f^T\left(\hat{\chi}^T(\omega_p)-\left(\hat{\chi}^T(\omega_q)\right)^*\right)\right). \tag{A.12}$$

Notice how, in the limit of no interwell coupling (i.e., for $\tau_e^{T(C)} \rightarrow \tau_s$ and $1/\tau_t^{T\leftarrow C}$, $1/\tau_t^{C\leftarrow T} \rightarrow 0$), $\chi_{CDM}^{C\leftarrow C}$ reduces to the expression for χ_{CDM} in Eq. (A.1), whereas $\chi_{CDM}^{C\leftarrow T}$ vanishes. These equations, with lifetimes taken to be the same for both types of wells (and with the summations over $|\vec{k}|$ treated as unimportant premultiplicative factors), are used in the fit of the experimental results of chapter 4.

Bibliography

[1] R. Paiella, G. Hunziker, U. Koren, and K. J. Vahala, "Polarization-dependent optical nonlinearities of multiquantum-well laser amplifiers studied by four-wave mixing," *IEEE J. Select. Topics Quantum Electron.*, vol. 3, pp. 529–540, 1997.

[2] W. W. Chow, S. W. Koch, and M. Sargent III, *Semiconductor-Laser Physics.* Berlin, Germany: Springer-Verlag, 1994.

[3] A. Uskov, J. Mϕrk, and J. Mark, "Wave mixing in semiconductor laser amplifiers due to carrier heating and spectral hole burning," *IEEE J. Quantum Electron.*, vol. 30, pp. 1769–1781, 1994.

Appendix B

FWM Conversion Efficiency and Optical Signal-to-Noise Ratio

B.1 The FWM Coupled-Mode Wave Equations

The FWM conversion efficiency and the optical signal-to-noise ratio (OSNR) of the FWM signal are strongly affected by the propagation properties of the SOA waveguide. Understanding these effects is important in spectroscopic applications, for an accurate interpretation of the experimental results. Furthermore, these same effects are crucial in determining the performance of wavelength conversion devices based on FWM. In this Appendix, we will review the basic theory [1]–[3] of the generation and propagation of the FWM signal in a SOA.

We begin by writing the electric field in the SOA (averaged over the transverse dimensions) as follows:

$$\mathcal{E}_i(z,t) = \sum_{f=p,q,s} E_i^{(f)}\, e^{-i\omega_f\left(t-\frac{\bar{n}_i^{(f)}}{c}z\right)} + c.c. \tag{B.1}$$

where as usual ω_p, $\omega_q = \omega_p - \Omega$ and $\omega_s = \omega_p + \Omega$ denote the frequencies of the pump wave, the input signal, and the FWM signal respectively, and we neglect the FWM signal of frequency $\omega_s' = \omega_q - \Omega$ as appropriate if the pump wave is much stronger than the input signal. The subscript i is used to distinguish between two orthogonal polarizations (i.e., TE and TM) for a wave traveling in the SOA waveguide (along the z direction). Finally, $\bar{n}_i^{(f)}$ is the modal index of refraction for the i^{th} polarization component at frequency ω_f.

In terms of the field amplitudes defined above, the FWM conversion efficiency η is given by

$$\eta = C^2 \frac{\left|\vec{E}^{(s)}(L)\right|^2}{\left|\vec{E}^{(q)}(0)\right|^2} \tag{B.2}$$

where $z = 0, L$ denote the input and output facets of the SOA respectively, and C is the light coupling efficiency into and out of the SOA.

A complete expression for this quantity is obtained by solving the coupled-mode wave equations of FWM, which can be written as

$$\frac{dE_i^{(f)}(z)}{dz} = T_i^{(f)}(z) E_i^{(f)}(z) \qquad f : p, q \tag{B.3}$$

$$\frac{dE_i^{(s)}(z)}{dz} = T_i^{(s)}(z)\; E_i^{(s)}(z) +$$

$$+ \sum_{j,k,l} \Gamma \kappa_{ijkl}(P_{tot}(z);\Omega) e^{i\Delta k_{ijkl} z} E_j^{(p)}(z) E_k^{(p)}(z) \left(E_l^{(q)}(z)\right)^* \tag{B.4}$$

where we defined the propagation factor

$$T_i^{(f)}(z) = \Gamma\left(\frac{1}{2}g_i^{(f)}(P_{tot}(z)) - i\delta k_i^{(f)}(P_{tot}(z))\right) - \frac{1}{2}\gamma \qquad f : p, q, s, \tag{B.5}$$

the nonlinear coupling tensor

$$\kappa_{ijkl}(P_{tot}(z);\Omega) = \frac{i}{2}\frac{\omega_s \mu_0 c}{\bar{n}_i^{(s)}}\chi_{ijkl}(P_{tot}(z);\Omega), \tag{B.6}$$

and the phase mismatch per unit length

$$\Delta k_{ijkl} = \frac{(\bar{n}_j^{(p)} + \bar{n}_k^{(p)})\omega_p - \bar{n}_l^{(q)}\omega_q - \bar{n}_i^{(s)}\omega_s}{c}. \tag{B.7}$$

In these equations, Γ is the confinement factor, $g_i^{(f)}$ and $-\delta k_i^{(f)}$ are the material gain coefficient and the carrier-induced phase shift per unit length for the i^{th} component of the field at frequency ω_f, $P_{tot}(z)$ is the total optical power along the axis of the waveguide, γ is the scattering loss coefficient, and χ_{ijkl} is the FWM susceptibility tensor.

In order to solve these equations, we need to model the dependence of the gain coefficient, the carrier-induced phase shift, and the FWM nonlinearity on the power $P_{tot}(z)$. As for the former two quantities, a commonly used approximation, based on the assumption of a linear relation between the first-order susceptibility and the carrier density, is the following:

$$\frac{1}{2}g_i^{(f)}(P_{tot}(z)) - i\delta k_i^{(f)}(P_{tot}(z)) = \frac{1}{1 + P_{tot}(z)/P_{sat}}\frac{g_{0i}^{(f)}}{2}\left(1 - i\alpha_i^{(f)}\right) \tag{B.8}$$

where we introduced the unsaturated material gain coefficient g_0, the linewidth enhancement factor α, and the saturation power P_{sat}. The FWM susceptibility, and hence the nonlinear coupling tensor κ_{ijkl}, depend on P_{tot} in a complicated manner, which can be derived rigorously from the microscopic expressions given in Appendix A, and which has been modeled with various degrees of approximation [1]–[3]. The simplest such approximation, which is nevertheless appropriate to a wide range of conditions, is the following:

$$\chi_{ijkl}(P_{tot}(z);\Omega) = \frac{1}{1+P_{tot}(z)/P_{sat}}\chi_{ijkl}(\Omega) \tag{B.9}$$

From the solution of Eqs. (B.3) and (B.4) (and use of the FWM polarization selection rules described in section 3.3), we obtain

$$E_i^{(s)}(L) = \left(E^{(p)}(0)\right)^2 \left(E^{(q)}(0)\right)^* \left[\left(p_i \sum_{k=1}^{2} M_{iikk}\, p_k\, q_k^*\right) + \right.$$
$$\left. + M_{ilil}\Big|_{l\neq i} p_l p_i q_l^* + M_{illi}\Big|_{l\neq i} p_l^2 q_i^*\right] \tag{B.10}$$

where $\hat{p}$ and $\hat{q}$ are the polarization unit vectors of the pump wave and the input signal at $z = 0$, and we defined the "transfer tensor"

$$M_{ijkl}(\Omega) \equiv \chi_{ijkl}(\Omega) R_{ijkl} =$$
$$\Gamma \exp\left(\int_0^L dz T_i^{(s)}(z)\right) e^{i\frac{\bar{n}_i^{(s)}\omega_s L}{c}} \int_0^L dz\ \kappa_{ijkl}(P_{tot}(z);\Omega)\times$$
$$e^{i\Delta k_{ijkl} z} \exp\left[\int_0^z dz' \left(T_j^{(p)}(z') + T_k^{(p)}(z') + (T_l^{(q)}(z'))^* - T_i^{(s)}(z')\right)\right]. \tag{B.11}$$

Notice that this expression can be somewhat simplified by noting that in practice the frequency dependence of the gain and the index over the wavelength shifts of interest is usually negligible.

The equations above (together with the microscopic expressions for χ_{ijkl} of Appendix A) give a complete solution for the FWM signal in a SOA. In order to use these results for any numerical simulation (such as the length-dependence study of section 7.2), we finally need to solve for the total optical power $P_{tot}(z)$. In a typical FWM experiment, the pump wave is quite stronger than the input signal (and both are much more intense than the converted signal). As a result, it is a fair approximation to take $P_{tot}(z) \approx P_p(z) \equiv |E_p(z)|^2$. Then, the following expression for $P_{tot}(z)$ is immediately derived by straightforward integration of Eq. (B.3) alone (with $f = p$):

$$P_{tot}(z) \approx P_p(0) \sum_{i=1}^{2} |p_i|^2 \exp\left(2 \int_0^z dz' Re[T_i^{(p)}(z')]\right) \tag{B.12}$$

Incidentally, this neglect of the input signal contribution to the total power is actually a necessary assumption in the case in which the input signal carries digital information. Otherwise, this same modulation would be transferred to the carrier density (and hence to the gain and the index), and the present analysis, which is inherently steady-state, would no longer be appropriate.

To conclude this section, we give below the limiting form of M_{ijkl} appropriate to the case in which the pump wave and input signal are copolarized (along the TE or TM axis in MQW SOAs), i.e., the case of practical interest in wavelength conversion applications:

$$M_{iiii}(\Omega) = \Gamma \exp\left[i \int_0^L dz \left(\frac{\bar{n}_i \omega_s z}{c} - \Gamma \delta k_i(P_{tot}(z))\right)\right] \times$$
$$\sqrt{G_i(L)} \int_0^L dz\ \kappa_{iiii}(P_{tot}(z); \Omega) G_i(z) \tag{B.13}$$

where we neglected any gain and index dispersion, and we defined the overall gain over a length z into the SOA

$$G_i(z) = \exp\left[\int_0^z dz' \left(\Gamma g_i(P_{tot}(z')) - \gamma\right)\right]. \tag{B.14}$$

B.2 Amplified Spontaneous Emission Noise in Semiconductor Optical Amplifiers

The BER performance of any wavelength conversion device is mainly determined by the OSNR of the converted signal, which, in this context, is defined as

$$OSNR \equiv \frac{C\left|\vec{E}^{(s)}(L)\right|^2}{P_{ASE}^{out}}. \tag{B.15}$$

(Strictly speaking, this is actually a signal-to-background ratio, but we keep the notation OSNR following common usage). The quantity P_{ASE}^{out} is defined as the (in-fiber) output amplified spontaneous emission (ASE) noise power, with frequency in the range $\Delta\nu_{det}$ (the resolution bandwidth of the spectrum analyzer used in the measurement, typically 12.5 GHz) around the FWM signal frequency. As such, it is given by

$$P_{ASE}^{out} = Ch\nu_s \Delta\nu_{det} \sum_{i=1}^{2} n_i(L) \tag{B.16}$$

where $n_i(L)\Delta\nu_{det}$ is the number of ASE photons with frequency within $\Delta\nu_{det}$ about ν_s, and state of polarization i, at the output facet of the SOA.

It is easy to argue that the variable $n_i(z)$ satisfies the boundary-value problem

$$\frac{dn_i(z)}{dz} = \Big\{\Gamma g_i(P_{tot}(z)) - \gamma\Big\} n_i(z) + \Gamma\beta_i(P_{tot}(z))$$

$$n_i(0) = n_i^{in} \tag{B.17}$$

where β is the spontaneous emission rate per unit length, n^{in} is the number of ASE photons coupled into the SOA (e.g., from the EDFA used to amplify the input waves), and we are neglecting the gain dispersion. The solution of Eqs. (B.16)-(B.17) can be written as

$$P_{ASE}^{out} = Ch\nu_s \Delta\nu_{res} \sum_{i=1}^{2} \Gamma G_i(L) \left(\int_0^L dz \frac{\beta(P_{tot}(z))}{G_i(z)} + n_i^{in} \right). \tag{B.18}$$

It should be noted that in a typical FWM wavelength conversion experiment a band-pass filter for ASE prefiltering is used at the input of the SOA (as discussed in section 7.2). In this case, the contribution to Eq. (B.18) proportional to n_i^{in} can be neglected.

Finally, in order to express P_{ASE}^{out} in terms of directly measurable parameters, we need to characterize the dependence of β_i on the total optical power within the SOA. First of all, recall that the following expressions are good approximations for semiconductor gain media, in the limit of negligible transition broadening (see, for instance, section 3-3 of Ref. [4]):

$$g_i(P_{tot}(z)) = g_i^M \left[f_e(P_{tot}(z)) + f_h(P_{tot}(z)) - 1\right]$$

$$\beta_i(P_{tot}(z)) = g_i^M f_e(P_{tot}(z)) f_h(P_{tot}(z)) \tag{B.19}$$

where f_e and f_h are the occupation probabilities for the conduction-band electrons and the valence-band holes, respectively, evaluated at the transition frequency ω_0, and g^M is a constant depending on a number of material and structural parameters. In a MQW active layer it can be written as [5]

$$g_i^M = \frac{\omega_0 m^* |(\vec{\mu}_{cv})_i|^2}{\epsilon \hbar^2 L_w} \tag{B.20}$$

where m^* is the reduced mass, $(\vec{\mu}_{cv})_i$ is the i^{th} component of the dipole moment matrix element, ϵ is the material dielectric constant, and L_w is the width of each QW.

Given the relation between the two Fermi functions, one can solve Eq. (B.19) for β_i as a function of g_i. This is particularly simple for the case of compressively-strained QW devices, because in this case the two Fermi functions are approximately equal, which leads to

$$\beta_i(P_{tot}(z)) = \frac{g_i^M}{4}\left[1 + \frac{g_i(P_{tot}(z))}{g_i^M}\right]^2. \tag{B.21}$$

In the more general case, we can take $f_e \propto f_h$ and Eq. (B.21) remains valid up to a multiplicative factor. In any case, once this expression is plugged in Eq. (B.18), the ASE output power is immediately evaluated.

Bibliography

[1] G. P. Agrawal, "Population pulsations and nondegenerate four-wave mixing in semiconductor lasers and amplifiers," *J. Opt. Soc. Am. B*, vol. 5, pp. 147–158, 1988.

[2] A. Mecozzi, S. Scotti, A. D'Ottavi, E. Iannone, and P. Spano, "Four-wave mixing in traveling-wave semiconductor amplifiers," *IEEE J. Quantum Electron.*, vol. 31, pp. 689–699, 1995.

[3] I. Koltchanov, S. Kindt, K. Petermann, S. Diez, R. Ludwig, R. Schnabel, and H. G. Weber, "Gain dispersion and saturation effects in four-wave mixing in semiconductor laser amplifiers," *IEEE J. Quantum Electron.*, vol. 32, pp. 712–720, 1996.

[4] W. W. Chow, S. W. Koch, and M. Sargent III, *Semiconductor-Laser Physics.* Berlin, Germany: Springer-Verlag, 1994.

[5] K. J. Vahala and C. E. Zah, "Effect of doping on the optical gain and the spontaneous noise enhancement factor in quantum well amplifiers and lasers studied by simple analytical expressions," *Appl. Phys. Lett.*, vol. 52, pp. 1945–1947, 1988.